Karlsruher Institut für Technologie

Electromagnetic Scattering by Objects Moving at Relativistic Speeds

Zur Erlangung des akademischen Grades eines

DOKTORS DER NATURWISSENSCHAFTEN (Dr. rer. nat.)

von der KIT-Fakultät für Physik des
Karlsruher Instituts für Technologie (KIT)
angenommene

DISSERTATION

von

MPhys Mitchell Rhodes Whittam

am Institut für Theoretische Festkörperphysik

Tag der mündlichen Prüfung:	31. Januar 2025
Referent:	Prof. Dr. Carsten Rockstuhl
Korreferent:	Prof. Dr. Thomas Pertsch

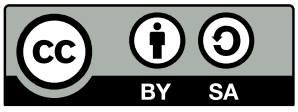

Selbstständigkeitserklärung

Eidesstattliche Versicherung gemäß §13 Absatz 2 Ziffer 3 der Promotionsordnung des Karlsruher Instituts für Technologie (KIT) für die KIT-Fakultät für Physik:

1. Bei der eingereichten Dissertation zu dem Thema

   "Electromagnetic Scattering by Objects Moving at Relativistic Speeds"

   handelt es sich um meine eigenständig erbrachte Leistung.

2. Ich habe nur die angegebenen Quellen und Hilfsmittel benutzt und mich keiner unzulässigen Hilfe Dritter bedient. Insbesondere habe ich wörtlich oder sinngemäß aus anderen Werken übernommene Inhalte als solche kenntlich gemacht.

3. Die Arbeit oder Teile davon habe ich bislang nicht an einer Hochschule des In- oder Auslands als Bestandteil einer Prüfungs- oder Qualifikationsleistung vorgelegt.

4. Die Richtigkeit der vorstehenden Erklärungen bestätige ich.

5. Die Bedeutung der eidesstattlichen Versicherung und die strafrechtlichen Folgen einer unrichtigen oder unvollständigen eidesstattlichen Versicherung sind mir bekannt.

Ich versichere an Eides statt, dass ich nach bestem Wissen die reine Wahrheit erklärt und nichts verschwiegen habe.

Ort und Datum Unterschrift

Acknowledgements

My time as a PhD student has been my greatest test of mental fortitude. Of course, physics is a demanding discipline that requires much hard work and dedication. However, the greatest challenge was continuing the PhD despite life's unexpected hurdles. Put bluntly, life doesn't stop just so you can do a PhD. For this reason, I am very proud to have reached the finish line, and it certainly wouldn't have been possible without the help of many influential people along the way.

Firstly, I would like to warmly thank my supervisor Carsten Rockstuhl. Most of all, I am grateful for his approachability. He always made me feel comfortable to express my opinion, even if I didn't agree with something. This is a quality every supervisor should have, so I feel very lucky. I also wish to thank him for his patience. The start of my PhD was a bumpy ride, but I greatly appreciate his belief that I could reach my potential. I would also like to thank Thomas Pertsch for taking the time to be my second examiner and for his engagement in my many TAC meetings.

Next, my appreciation goes to the wonderful people in TFP, both past and present. It has been the ultimate privilege to work with such intelligent and insightful people. I wish only the best for you all. For those still on their PhD journey, please have the same belief in yourselves as I do in you. A special thanks goes to Aristeidis Lamprianidis and Yannick Augenstein. It's no understatement that their collaboration on my first project saved my PhD. I learned a great deal from them both, allowing me to become a confident researcher.

Looking back on my formative years, I have realised the importance of quality teaching. I am very fortunate to have had many encouraging and enthusiastic teachers who shaped my life. Starting with my teachers at Bowland High School, I would like to thank my Maths teacher, Mr Whittaker. For three years, I was performing very poorly in exams. Instead of moving me to a lower group, he believed in me and helped me realise my potential, for which I am forever grateful. Furthermore, I wish to thank my Biology teacher Mr Breen for sharing his infectious enthusiasm for science. I have much admiration for his commitment to education, and he is the embodiment of how a teacher should be. Finally, thank you to my German teacher Mr Morrissey for nurturing my passion for foreign languages. I greatly appreciate his constant willingness to correct my work and challenge me further. His contribution to my education played a significant role in my decision to come to Germany.

Going back even further, I wish to thank my Year 4 teacher at Waddington and West Bradford Primary School, Mr Dugdale. When asked if I could miss school to go to South Africa, he said yes, because "*travelling is the best education a child can have*". Those words always stayed with me, and also inspired my move to Germany.

On a personal note, I would like to thank my long-time friend Safdar for always making me laugh. I look forward to the many games of golf to come, even though you spend more time in the sand than David Hasselhoff. Last but not least, I wish to express my deepest gratitude to my mum Victoria, dad Jeffrey and brother James. It has been a true blessing to grow up with such a loving and supportive family. I hope I have done you all proud.

Abstract

The electromagnetic scattering of light has become cemented as a core research topic the world over. In the context of Mie theory, for example, the focus has predominantly been on scattering by stationary objects. With a look to the future, increasingly more research on the effects of relativistic motion has been emerging. The main reasons for considering relativistic effects are twofold. Firstly, of great interest is simply the fundamental question *"how does relativistic motion affect the electromagnetic scattering by different objects?"*. A second question is *"how can the scattering response of an object be exploited to design spacecraft that reach distant locations as quickly as possible?"*. This thesis draws on both sources of motivation, offering abstract insights as well as potential areas of application.

Beginning with a more abstract scenario, this thesis begins with exploring the energy backscattered by a relativistically moving sphere as seen by an external observer. The necessary calculations rely on a combination of Mie theory and special relativity, and demonstrate the power of the frame-hopping method (FHM). The FHM allows one to apply methods from scattering theory and special relativity in a logical order. Specifically, it is shown why one must apply Mie theory in the scatterer's inertial reference frame and not the frame of the observer. In addition to a general visualisation of the backscattered signal, numerical optimisation methods are implemented to minimise it. Such a minimisation resembles a relativistic version of the first Kerker condition.

The case of a single sphere transitions naturally to scattering by relativistically moving arrays of spheres. The spherical arrays correspond to light sails. Using lasers, it is planned to accelerate microsatellites equipped with light sails to 20% of the speed of light to explore neighbouring solar systems. In this thesis, the effects of relativistic motion on lattice interactions within the light sails are investigated. Moreover, the time taken to reach the abovementioned target speed is minimised for various sail configurations. It is also emphasised why one should ensure a high reflectance and low absorptance of the incident light. A high reflectance is required for maximum momentum transfer, while a low absorptance minimises thermal damage. An optimal light sail comprising core-shell spheres made from silicon and silicon dioxide is found that possesses these qualities.

The investigation of interstellar chiral molecules has also gathered much attention in recent years. To build on previous work, this thesis discusses the effects of relativistic motion on the transmission circular dichroism (TCD) of three chiral biomolecules: B-DNA, chlorophyll *a* and chlorophyll *b*. The TCD is a function of the wavelength of the incident field and quantifies the difference between the transmittances of right- and left-circularly polarised light. It is described how the TCD needs to be redefined since the molecules are of finite size. Specifically, a correction term is required to account for higher-order multipolar contributions of the incoming light. Importantly, it is found that the TCD scales to shorter wavelengths with increasing speeds.

Contents

List of Figures

List of Tables

Publications

I was involved in the research in the following peer-reviewed articles, which form the basis of this thesis.

Peer-reviewed articles

[P1] M. R. Whittam, A. G. Lamprianidis, Y. Augenstein, and C. Rockstuhl, "Identifying regions of minimal backscattering by a relativistically moving sphere", Physical Review A **108**, 043510 (2023).

[P2] M. R. Whittam, L. Rebholz, B. Zerulla, and C. Rockstuhl, "Analyzing the acceleration time and reflectance of light sails made from homogeneous and core-shell spheres", Optical Materials Express **15**, 345–361 (2025).

[P3] M. R. Whittam, B. Zerulla, M. Krstić, M. Vavilin, C. Holzer, M. Nyman, L. Rebholz, I. Fernandez-Corbaton, and C. Rockstuhl, "Circular dichroism of relativistically–moving chiral molecules", Scientific Reports **14**, 16812 (2024).

I also made the following conference contributions.

Conference contributions

[C1] M. R. Whittam, A. G. Lamprianidis, Y. Augenstein, and C. Rockstuhl, "Identifying regions of minimal back-scattering by a relativistically-moving sphere", in *Metamaterials 2023, Seventeenth International Congress on Artificial Materials for Novel Wave Phenomena*, Chania, Greece (2023).

1 | Introduction and Thesis Structure

Introduction

Electromagnetic scattering is a phenomenon that has captured the interest of curious minds for many centuries. On both a small and a large scale, studying the scattering of light has significantly advanced humankind's understanding of the universe. From natural wonders such as a blue sky and rainbows to medical applications including cardiovascular imaging [1–5], determining the severity of burns [6–9] and cancer detection [10–13], the versatility of light scattering knows no bounds.

A widely used method to theoretically describe electromagnetic scattering is Mie theory, a formalism devised in 1908 by Gustav Mie [14]. Nowadays expressed using the transition or T-matrix, which links incident to scattered electromagnetic fields [15], Mie theory enables one to determine the scattering response by a sphere. Most commonly, Mie theory has been applied in a non-relativistic regime [16–29]. With a look to the future, the addition of motion to spherical scatterers has prompted an extension to work done on stationary spheres, gaining a lot of popularity in the scientific community [30–33].

An extension to Mie theory comes in the form of scattering by arbitrary objects, including molecules, periodic lattices and stratified media [29, 34–44]. In a relativistic setting, a significant source of motivation for studying more complex, relativistic systems is the Breakthrough Starshot Initiative (BSI) announced in 2016. The aim of the BSI is to use an Earth-based laser array to accelerate microgramme satellites equipped with a light sail to 20% of the speed of light to explore neighbouring solar systems [45, 46]. It would take such a system just over 20 years to carry out a flyby mission past Alpha Centauri [47]. As a comparison, the Voyager 1 probe launched in 1977 is the most distant human-made object ever launched into space. However, Voyager 1 only moves at approximately $17,000$ m/s with respect to the Sun (0.006% of the speed of light) [48]. To put this in perspective, Alpha Centauri is located approximately 4.37 light years from Earth [49], meaning it would take Voyager 1 about $77,980$ years longer than the abovementioned microgramme satellites to undertake the journey planned in the BSI.

To ensure a light sail fit for its anticipated purpose, many engineering challenges must be overcome, including the thermal management and stability of the light sail [50–56]. As a result, a sensible choice of materials from which to construct the light sail is of utmost importance. Crucially, the light sail should have a high reflectivity and a low absorptance. The former is imperative to ensure maximum momentum transfer to the light sail, while the latter is necessary to minimise unwanted thermal deformation in the light sail. Potential material candidates include metals such as aluminium (Al) due to its high reflectivity [57, 58], as well as dielectrics such as silicon dioxide (SiO_2) due to its low absorptance of near-infrared light [59]. This is important since a near-infrared incident light source has been proposed for the BSI [53, 60, 61]. Further possibilities include combining various materials in the form of layered slabs [62–64], or exploiting the high reflectance that emerges from structures such as Bragg reflectors [65–70].

Also of great interest is the fundamental topic of scattering by interstellar molecules, as evident in recent work done to detect chiral molecules in space [71, 72]. Chirality, a term defined by Lord Kelvin describing an object that cannot be superimposed on its mirror image, is a property exhibited by most molecules vital to life. Examples of such molecules include amino acids, sugars and DNA [73–79]. After the recent discovery of the first known interstellar chiral molecule propylene oxide (CH_3CHCH_2O) in 2016 [71], the further investigation of such molecules has gained great significance.

As a contribution to this endeavour, this thesis will consider the impact of relativistic effects on the circular dichroism, or CD, of various biomolecules. The CD is usually defined as the difference in the absorption of left- and right-circularly polarised light [80–87]. Such a CD will be referred to in this thesis as ACD. For practical purposes, the transmission CD (TCD) will also be explored, defined as the difference in the transmission of left- and right-circularly polarised light. Knowing the CD of an object is crucial in the fields of biology and chemistry. For example, CD spectra can be used to gain more information about secondary structures in amino acids and proteins [88–91].

Thesis structure

After this chapter, the thesis is structured as follows:

Chapter 2 offers an overview of the theoretical tools of electrodynamics that provide the building blocks for future chapters. Departing from Maxwell's equations, vector spherical harmonics (VSHs) will be defined. The VSHs serve as elementary solutions to the vector Helmholtz equation and are used to express an electromagnetic field in terms of spherical waves. Specifically, an electromagnetic field can be expressed as a series of VSHs, along with expansion coefficients that are different for an incident and scattered field.

Once the fields are defined, it will be shown how scattered and incident fields relating to an arbitrary object are linked by the transition, or T-matrix. For spheres, the T-matrix contains quantities known as Mie coefficients, which depend on the sphere's geometry and the material from which it is made. Afterwards, two transformations are discussed: the conversion of a T-matrix from the parity to the helicity basis and how a T-matrix behaves under rotations. Following this, Mie angles are defined, which allow one to observe the scattered field patterns corresponding to every possible set of Mie coefficients describing a sphere.

After discussing a single scatterer, field scattering by periodic and layered structures is considered. Moreover, the renormalised T-matrix of an infinitely-extended lattice is defined. The renormalised T-matrix accounts for lattice interactions and relies on the T-matrix of a single lattice constituent. In all calculations relating to scattering by lattices, relevant functions in the program *treams* [92] are leveraged. Chapter 2 concludes with how to obtain the ACD and TCD of an object. Importantly, it is explained how the TCD needs to be modified when considering objects of finite size.

Chapter 3 continues with the theoretical background, this time covering special relativity. Firstly, the Lorentz boost operator will be defined. The frame-hopping method (FHM) will also be outlined. The FHM dictates in which order Lorentz boosts and scattering calculations should occur. Next, Doppler shifting is discussed. In the context of electrodynamics, a Doppler shift corresponds to the stretching or contraction of electromagnetic waves as

viewed by an external, moving observer. Following this, the concept of length contraction and its effect on scattering calculations is outlined. Next, it is discussed how electromagnetic fields behave under Lorentz boosts. Highlighted are two specific examples: the boosted fields of a moving positive point charge and a boosted plane wave. Afterwards, it is shown how helical fields change under Lorentz boosts. Helical fields are described by the helicity λ, where $\lambda = +1$ denotes left-circularly polarised waves, while $\lambda = -1$ denotes right-circularly polarised waves. Crucially, the helicity of electromagnetic fields is invariant under Lorentz boosts, allowing for cleaner calculations.

Chapter 4 is based on the work done in Ref. [P1]. The goal was to investigate the backscattered signal from a relativistically moving, lossless sphere. In terms of the Mie angles mentioned above, a quantity known as the directivity is visualised. The directivity is the ratio of the backscattered energy density to the average scattered energy per unit solid angle. Furthermore, the backscattered directivity is minimised using optimisation techniques based on gradient descent. The ability to minimise backscattered light is leveraged by some plants, for example, to absorb as much light as possible [93].

Chapter 5 is based on Ref. [P2] and extends the work of the previous chapter to scattering by lattices containing spherical objects. Such structures resemble light sails proposed by the BSI mentioned before. As opposed to Chapter 4, a large backscattered field is desired. Recall that a high reflection corresponds to a large momentum transfer, reducing the acceleration time. The acceleration time is the time required for a light sail to reach its target speed. Furthermore, Chapter 5 considers lattices comprising multilayered spheres. An optimal sail consisting of silicon/silicon dioxide core-shell spheres is found, which exhibits high reflectance and low absorptance. The effects of adding an embedding to the lattice is discussed, as well as its influence on the acceleration time.

Chapter 6 is based on Ref. [P3] and serves as the final results chapter. It concerns the scattering of light by three relativistically moving biomolecules: B-DNA, chlorophyll *a* and chlorophyll *b*. Specifically, the effects of relativistic motion on the resulting TCD spectra will be observed.

In **Chapter 7**, the work in this thesis is concluded and potential future work is suggested.

2 | Electrodynamics

Before engaging in any applications, it is important to build a theoretical framework on which the results are based. The most logical place to start is Maxwell's equations, the cornerstone of electromagnetism. Arguably the most important application of Maxwell's equations in the context of this thesis comes in the form of light scattering by arbitrary objects. Here, vector spherical VSHs will be defined, which are elementary solutions to the vector Helmholtz equation. Furthermore, VSHs allow one to represent an electromagnetic field as an infinite series of multipolar contributions. For example, The first term in the series is the dipole, the second is the quadrupole, and so on. For numerical purposes, it is necessary to truncate multipolar fields up to a desired order. This maximum order depends on the material of a scattering object, as well as its relative size to the wavelength of the incident field. For example, for the molecules discussed in Chapter 6, only dipolar components contribute to the scattered field.

The field scattered by an object is conveniently obtained using the transition or T-matrix, which relates the incident field to the scattered field. Firstly, the T-matrix for a dielectric sphere will be discussed, as required in Chapter 4. Afterwards, it will be shown how one can convert a T-matrix from the parity basis to the helicity basis, as well as how to rotate it. Next, scattering by periodic and stratified media, like those considered in Chapter 5, will be highlighted. Finally, it will be shown how to obtain the ACD and TCD of an object.

2.1 Maxwell's equations

2.1.1 Time domain

To begin, it is necessary to define Maxwell's equations in their macroscopic form in the time-domain. The macroscopic Maxwell equations describe the behaviour of fields within a medium, and form the theoretical basis of all the work in this thesis. In the space-time domain $(\mathbf{r}, t)$, these are given by [94]:

$$\nabla \cdot \mathbf{D}(\mathbf{r}, t) = \rho(\mathbf{r}, t) \tag{2.1}$$

$$\nabla \times \mathbf{H}(\mathbf{r}, t) - \frac{\partial \mathbf{D}(\mathbf{r}, t)}{\partial t} = \mathbf{J}(\mathbf{r}, t) \tag{2.2}$$

$$\nabla \times \mathbf{E}(\mathbf{r}, t) + \frac{\partial \mathbf{B}(\mathbf{r}, t)}{\partial t} = \mathbf{0} \tag{2.3}$$

$$\nabla \cdot \mathbf{B}(\mathbf{r}, t) = 0, \tag{2.4}$$

where $\mathbf{E}(\mathbf{r}, t)$ and $\mathbf{B}(\mathbf{r}, t)$ represent the electric and magnetic fields, respectively, $\mathbf{D}(\mathbf{r}, t)$ is the displacement field and $\mathbf{H}(\mathbf{r}, t)$ is the magnetising field. Moreover, $\mathbf{J}(\mathbf{r}, t)$ and $\rho(\mathbf{r}, t)$ are the current and charge densities, respectively. Collectively, $\mathbf{D}(\mathbf{r}, t)$ and $\mathbf{H}(\mathbf{r}, t)$ are known as auxiliary fields and allow for a large-scale consideration of the behaviour of matter. These

auxiliary fields are related to $\mathbf{E}(\mathbf{r},t)$ and $\mathbf{B}(\mathbf{r},t)$ as follows:

$$\mathbf{D}(\mathbf{r},t) = \epsilon_0 \mathbf{E}(\mathbf{r},t) + \mathbf{P}(\mathbf{r},t) \tag{2.5}$$

$$\mathbf{H}(\mathbf{r},t) = \frac{1}{\mu_0}\mathbf{B}(\mathbf{r},t) - \mathbf{M}(\mathbf{r},t), \tag{2.6}$$

where ϵ_0 and μ_0 are the permittivity and permeability of free space, respectively, while $\mathbf{P}(\mathbf{r},t)$ and $\mathbf{M}(\mathbf{r},t)$ are the polarisation and magnetisation fields, respectively. The fields $\mathbf{P}(\mathbf{r},t)$ and $\mathbf{M}(\mathbf{r},t)$ depend on the electric field $\mathbf{E}(\mathbf{r},t)$ and magnetic field $\mathbf{B}(\mathbf{r},t)$. Assuming the electromagnetic field amplitudes are small enough, the polarisation $\mathbf{P}(\mathbf{r},t)$ can be directly proportional to $\mathbf{E}(\mathbf{r},t)$, where the resulting response is said to be linear. For non-local media, the elements $P_i(\mathbf{r},t)$ of $\mathbf{P}(\mathbf{r},t)$ can be written in terms of the elements $E_i(\mathbf{r},t)$ of $\mathbf{E}(\mathbf{r},t)$ as

$$P_i(\mathbf{r},t) = \epsilon_0 \sum_j \int_{\mathbb{R}^3} \mathrm{d}^3\mathbf{r}' \int_{-\infty}^{t} \mathrm{d}t' R_{ij}^{(\mathrm{e})}(\mathbf{r}-\mathbf{r}', t-t') E_j(\mathbf{r}', t'), \quad i,j \in \{x,y,z\} \tag{2.7}$$

where ϵ_0 is the permittivity of free space, and $R_{ij}^{(\mathrm{e})}(\mathbf{r}-\mathbf{r}', t-t')$ is the electric response function. The word 'response' is used, because the polarisation is caused by the electric field. Similarly, the elements $M_i(\mathbf{r},t)$ of the magnetisation $\mathbf{M}(\mathbf{r},t)$ are related to the elements $H_i(\mathbf{r},t)$ of $\mathbf{H}(\mathbf{r},t)$ as

$$M_i(\mathbf{r},t) = \sum_j \int_{\mathbb{R}^3} \mathrm{d}^3\mathbf{r}' \int_{-\infty}^{t} \mathrm{d}t' R_{ij}^{(\mathrm{m})}(\mathbf{r}-\mathbf{r}', t-t') H_j(\mathbf{r}', t')\,, \tag{2.8}$$

where $R_{ij}^{(\mathrm{m})}(\mathbf{r}-\mathbf{r}', t-t')$ is the magnetic response function. For local media, the spatial convolutions in Eqs (2.7) and (2.8) produce a delta distribution $\delta(\mathbf{r}-\mathbf{r}')$, such that $P_i(\mathbf{r},t)$ and $M_i(\mathbf{r},t)$ reduce to

$$P_i(\mathbf{r},t) = \epsilon_0 \sum_j \int_{-\infty}^{t} \mathrm{d}t' R_{ij}^{(\mathrm{e})}(\mathbf{r}, t-t') E_j(\mathbf{r}, t')\,, \tag{2.9}$$

and

$$M_i(\mathbf{r},t) = \sum_j \int_{-\infty}^{t} \mathrm{d}t' R_{ij}^{(\mathrm{m})}(\mathbf{r}, t-t') H_j(\mathbf{r}, t')\,. \tag{2.10}$$

2.1.2 Frequency domain

It is common to study linear media in the frequency domain $(\mathbf{r},\omega)$, where ω is the temporal frequency. Accordingly, a general field $\mathbf{F}(\mathbf{r},t)$ in Maxwell's equations needs to be converted via a Fourier transform to $\widetilde{\mathbf{F}}(\mathbf{r},\omega)$, where

$$\widetilde{\mathbf{F}}(\mathbf{r},\omega) = \int_{-\infty}^{\infty} \mathrm{d}t\, \mathbf{F}(\mathbf{r},t)\mathrm{e}^{\mathrm{i}\omega t}. \tag{2.11}$$

Coupled with the Fourier transform of the time differential

$$\frac{\partial}{\partial t} \xrightarrow{\mathrm{FT}} -\mathrm{i}\omega, \tag{2.12}$$

Maxwell's equations in the frequency domain read

$$\nabla \cdot \widetilde{\mathbf{D}}(\mathbf{r},\omega) = 0 \tag{2.13}$$

$$\nabla \times \widetilde{\mathbf{H}}(\mathbf{r},\omega) = -\mathrm{i}\omega\widetilde{\mathbf{D}}(\mathbf{r},\omega) \tag{2.14}$$

$$\nabla \times \widetilde{\mathbf{E}}(\mathbf{r},\omega) = \mathrm{i}\omega\widetilde{\mathbf{B}}(\mathbf{r},\omega) \tag{2.15}$$

$$\nabla \cdot \widetilde{\mathbf{B}}(\mathbf{r},\omega) = 0\,, \tag{2.16}$$

where there are no external charges ($\rho = 0$) or external currents ($\mathbf{J}(\mathbf{r},t) = \mathbf{0}$) exist, as is the case in the entirety of this thesis. For completion, the Fourier transformed polarisation $\widetilde{P}_i(\mathbf{r},\omega)$ and magnetisation elements $\widetilde{M}_i(\mathbf{r},\omega)$ are given by

$$\widetilde{P}_i(\mathbf{r},\omega) = \epsilon_0 \sum_j \chi_{ij}^{(\mathrm{e})}(\mathbf{r},\omega)\widetilde{E}_j(\mathbf{r},\omega)\,, \tag{2.17}$$

and

$$\widetilde{M}_i(\mathbf{r},\omega) = \sum_j \chi_{ij}^{(\mathrm{m})}(\mathbf{r},\omega)\widetilde{H}_j(\mathbf{r},\omega)\,, \tag{2.18}$$

where $\chi_{ij}^{(\mathrm{e})}(\mathbf{r},\omega)$ and $\chi_{ij}^{(\mathrm{m})}(\mathbf{r},\omega)$ are the electric and magnetic susceptibilities, respectively.

When discussing spherical electric fields in the next chapter, the electric field in a homogeneous and isotropic medium will be considered. The homogeneity means that the susceptibility tensors are independent of $\mathbf{r}$. Due to isotropy, the susceptibility tensors only contain components along their leading diagonals, which are all equal. As a result, the electric and magnetic susceptibilities can be treated as scalars $\chi^{(\mathrm{e})}(\omega)$ and $\chi^{(\mathrm{m})}(\omega)$, respectively, where

$$\widetilde{\mathbf{P}}(\mathbf{r},\omega) = \epsilon_0\chi^{(\mathrm{e})}(\omega)\widetilde{\mathbf{E}}(\mathbf{r},\omega)\,, \tag{2.19}$$

and

$$\widetilde{\mathbf{M}}(\mathbf{r},\omega) = \chi^{(\mathrm{m})}(\omega)\widetilde{\mathbf{H}}(\mathbf{r},\omega)\,. \tag{2.20}$$

Correspondingly, one sees from Eqs (2.5) and (2.6) that the fields $\widetilde{\mathbf{D}}(\mathbf{r},\omega)$ and $\widetilde{\mathbf{B}}(\mathbf{r},\omega)$ simplify to

$$\widetilde{\mathbf{D}}(\mathbf{r},\omega) = \epsilon(\omega)\widetilde{\mathbf{E}}(\mathbf{r},\omega) \quad \text{and} \quad \widetilde{\mathbf{B}}(\mathbf{r},\omega) = \mu(\omega)\widetilde{\mathbf{H}}(\mathbf{r},\omega) \tag{2.21}$$

where [95]

$$\epsilon(\omega) = \epsilon_0[1+\chi^{(\mathrm{e})}(\omega)] \quad \text{and} \quad \mu(\omega) = \mu_0[1+\chi^{(\mathrm{m})}(\omega)]\,. \tag{2.22}$$

In this section, the theoretical foundation of this thesis was laid by defining Maxwell's equations in the time and frequency domains. In the next section, the vector Helmholtz equation will be discussed, paving way for the development of the T-matrix method and Mie theory.

2.2 T-matrix method and Mie theory

After having covered Maxwell's equations, one can now apply them to develop the T-matrix method and Mie theory. The T-matrix method is used to obtain an expression for the field scattered by an object. Specifically, the T-matrix relates the incident field to the scattered field. Before defining the T-matrix, however, it is necessary to obtain expressions for the vector spherical harmonics (VSHs). VSHs are the elementary solutions to the spherical Helmholtz equation, which will now be discussed.

2.2.1 The Helmholtz equation and vector spherical harmonics

Using the frequency domain Maxwell's equations from the previous section, one can derive a vector differential equation in terms of the spatial electric field $\mathbf{E}(\mathbf{r})$. Note that the tilde $\tilde{}$ and frequency argument ω have been dropped for brevity, and a time harmonic field described by $\exp(-\mathrm{i}\omega t)$ is assumed. Moreover, although an accompanying magnetic field $\mathbf{B}(\mathbf{r})$ will always exist, one can obtain it from the electric field using Maxwell's equations. As a result, explicit reference to the magnetic field will be omitted in this section.

This required differential equation for $\mathbf{E}(\mathbf{r})$ is known as the Helmholtz equation, and is given by [17, Eq. (C.13)]

$$(\nabla^2 + k^2)\mathbf{E}(\mathbf{r}) = \mathbf{0}\,, \tag{2.23}$$

where $k = \omega/c$ and $\mathbf{0}$ is the zero vector. When deriving Eq. (2.23), it is assumed that $\mathbf{E}(\mathbf{r})$ is divergence free. This is the case for isotropic, linear and homogeneous media. In the Cartesian basis, the elementary solutions to Eq. (2.23) are elliptically polarised plane waves, where

$$\mathbf{E}(\mathbf{r}) = \boldsymbol{\mathcal{E}}_1 \mathrm{e}^{\mathrm{i}\mathbf{k}\cdot\mathbf{r}} + \boldsymbol{\mathcal{E}}_2 \mathrm{e}^{-\mathrm{i}\mathbf{k}\cdot\mathbf{r}}\,, \tag{2.24}$$

where $\mathbf{k}$ is the wave vector, and $\boldsymbol{\mathcal{E}}_1$ and $\boldsymbol{\mathcal{E}}_2$ contain the polarisation and amplitude of each constituent solution. As mentioned, however, the elementary solutions in the spherical basis are required. In this case, a scalar field ansatz $\psi(kr, \theta, \phi)$ is used, which satisfies the scalar Helmholtz equation

$$(\nabla^2 + k^2)\psi(kr, \theta, \phi) = 0\,, \tag{2.25}$$

where $\theta \in [0, \pi\}$ and $\phi \in [0, 2\pi]$ are the polar and azimuthal angles, respectively. As shown in Ref. [96], if $\psi(kr, \theta, \phi)$ is a solution to the scalar Helmholtz equation, then the VSHs of well-defined parity

$$\mathbf{M}^{(j)}_{\ell m}(k\mathbf{r}) = \nabla \times [\mathbf{r}\psi^{(j)}_{\ell m}(\mathbf{r})] \tag{2.26}$$

and

$$\mathbf{N}^{(j)}_{\ell m}(k\mathbf{r}) = \frac{1}{k}\nabla \times \mathbf{M}^{(j)}_{\ell m}(k\mathbf{r}) \tag{2.27}$$

are elementary solutions to the vector Helmholtz equation Eq. (2.23), where the index ℓ represents the considered multipolar order. Specifically, $\ell = 1, 2, \ldots, \ell_{\max}$, where the values $1, 2, \ldots$ correspond to dipoles, quadrupoles, and so on. Although there are infinitely

many multipolar orders, one requires a truncation order $\ell_{\max}$ for numerical purposes when describing incident and scattered fields. The expressions for said fields depend on $\mathbf{M}_{\ell m}^{(j)}(k\mathbf{r})$ and $\mathbf{N}_{\ell m}^{(j)}(k\mathbf{r})$, and will be discussed in the following subsection.

The choice for $\ell_{\max}$ depends on the size and material of the scattering object. When molecules are considered in Chapter 6, a dipolar truncation order of $\ell_{\max} = 1$ will be considered, due to the molecules only being of nanometre scale. The index m stands for the angular momentum along the z-axis and is related to ℓ as $m \in [-\ell_{\max}, ..., -2, -1, 0, 1, 2, ..., \ell_{\max}]$. The superscript j refers to the corresponding Bessel ($j = 1$) and Hankel ($j = 3$) functions of the first kind, $z_{\mathrm{M},\ell}^{(j)}(kr)$. The choice of function corresponds to boundary conditions incident and scattered fields need to obey; this aspect will be elaborated on in a later subsection.

To write the VSHs $\mathbf{M}_{\ell m}^{(j)}(k\mathbf{r})$ and $\mathbf{N}_{\ell m}^{(j)}(k\mathbf{r})$ more explicitly, one requires the solution to $\psi_{\ell m}^{(j)}(\mathbf{r})$, which is given by

$$\psi_{\ell m}^{(j)}(\mathbf{r}) = z_{\mathrm{M},\ell}^{(j)}(kr) Y_\ell^m(\theta, \phi)\,, \tag{2.28}$$

where $Y_\ell^m(\theta, \phi)$ are the spherical harmonics

$$Y_\ell^m(\theta, \phi) = \Omega_{\ell m} P_\ell^m(\cos\theta) \mathrm{e}^{\mathrm{i}m\phi}, \tag{2.29}$$

and $P_\ell^m(\cos\theta)$ are the associated Legendre functions. Moreover, the factor

$$\Omega_{\ell m} = \sqrt{\frac{(2\ell+1)(\ell-m)!}{4\pi\ell(\ell+1)(\ell+m)!}} \tag{2.30}$$

represents the corresponding normalisation [17, Eq. (C.22)].

As a result, $\mathbf{M}_{\ell m}^{(j)}(k\mathbf{r})$ and $\mathbf{N}_{\ell m}^{(j)}(k\mathbf{r})$ can be written as [96]:

$$\begin{aligned}
\mathbf{M}_{\ell m}^{(j)}(k\mathbf{r}) &= \nabla \times \left[\mathbf{r} z_{\mathrm{M},\ell}^{(j)}(kr) Y_\ell^m(\theta, \phi)\right] \\
&= z_{\mathrm{M},\ell}^{(j)}(kr) \mathbf{m}_{\ell m}(\hat{\mathbf{r}}), \qquad (2.31) \\
\mathbf{N}_{\ell mk}^{(j)}(\mathbf{r}) &= \frac{1}{k} \nabla \times \mathbf{M}_{\ell mk}^{(j)}(\mathbf{r}) \\
&= \hat{\mathbf{r}} \frac{\ell(\ell+1)}{k_0 r} z_{\mathrm{M},\ell}^{(j)}(kr) Y_\ell^m(\theta, \phi) + z_{\mathrm{N},\ell}^{(j)}(kr) \mathbf{n}_{\ell m}(\hat{\mathbf{r}}), \qquad (2.32)
\end{aligned}$$

where

$$\mathbf{m}_{\ell m}(\hat{\mathbf{r}}) = \Omega_{\ell m} \left[\hat{\theta} \mathrm{i} \pi_{\ell m}(\theta) - \hat{\phi} \tau_{\ell m}(\theta)\right] \mathrm{e}^{\mathrm{i}m\phi}, \tag{2.33}$$

$$\mathbf{n}_{\ell m}(\hat{\mathbf{r}}) = \Omega_{\ell m} \left[\hat{\theta} \tau_{\ell m}(\theta) + \mathrm{i} \hat{\phi} \pi_{\ell m}(\theta)\right] \mathrm{e}^{\mathrm{i}m\phi}. \tag{2.34}$$

Moreover, the functions

$$z_{\mathrm{N},\ell}^{(j)}(kr) = \frac{1}{kr} \frac{\mathrm{d}}{\mathrm{d}(kr)} \left[kr z_{\mathrm{M},\ell}^{(j)}(kr)\right] \tag{2.35}$$

are the corresponding Riccati functions,

$$\pi_{\ell m}(\theta) = m \frac{P_\ell^m(\cos\theta)}{\sin\theta} \tag{2.36}$$

and

$$\tau_{\ell m}(\theta) = \frac{\mathrm{d}P_\ell^m(\cos\theta)}{\mathrm{d}\theta}\,. \tag{2.37}$$

Now that the VSHs have been defined in the parity basis, one can utilise the obtained expressions to define analogous quantities in the helicity basis. This will be of great significance in Chapters 4 and 6, where helicity basis is leveraged due to its invariance under Lorentz boosts.

The VSHs $\mathbf{\Lambda}^{(j)}_{\lambda,\ell m}(k\mathbf{r})$ corresponding to a well-defined helicity $\lambda = \pm 1$ are defined in terms of the VSHs in the parity basis as [16]:

$$\begin{aligned}\mathbf{\Lambda}^{(j)}_{\lambda,\ell m}(k\mathbf{r}) &= \frac{\mathbf{M}^{(j)}_{\ell m}(k\mathbf{r}) + \lambda\mathbf{N}^{(j)}_{\ell m}(k\mathbf{r})}{\sqrt{2}} \\ &= \frac{\lambda}{\sqrt{2}}\frac{\ell(\ell+1)}{kr} z^{(j)}_{\mathrm{M},\ell}(kr) Y^m_\ell(\theta,\phi)\hat{\mathbf{r}} \\ &+ \sum_{\lambda'=\pm 1}\Big[\frac{z^{(j)}_{\mathrm{M},\ell}(kr) + \lambda\lambda' z^{(j)}_{\mathrm{N},\ell}(kr)}{2}\mathbf{f}_{\lambda',\ell m}(\hat{\mathbf{r}})\Big]\,.\end{aligned} \tag{2.38}$$

For a helical polarisation

$$\hat{\mathbf{e}}_\lambda(\hat{\mathbf{r}}) = \frac{-\lambda\hat{\boldsymbol{\theta}}(\hat{\mathbf{r}}) - \mathrm{i}\hat{\boldsymbol{\phi}}(\hat{\mathbf{r}})}{\sqrt{2}} \tag{2.39}$$

described by the spherical unit vectors $\hat{\boldsymbol{\theta}}(\hat{\mathbf{r}})$ and $\hat{\boldsymbol{\phi}}(\hat{\mathbf{r}})$, the quantity $\mathbf{f}_{\lambda,\ell m}(\hat{\mathbf{r}})$ is defined in terms of $\mathbf{m}_{\ell m}(\hat{\mathbf{r}})$ and $\mathbf{n}_{\ell m}(\hat{\mathbf{r}})$ as

$$\mathbf{f}_{\lambda,\ell m}(\hat{\mathbf{r}}) = \frac{\mathbf{m}_{\ell m}(\hat{\mathbf{r}}) + \lambda\mathbf{n}_{\ell m}(\hat{\mathbf{r}})}{\sqrt{2}}. \tag{2.40}$$

Note that the vector function $\mathbf{f}_{\lambda,\ell m}(\hat{\mathbf{r}})$ obeys the orthogonality property

$$\int_0^{2\pi}\mathrm{d}\phi\int_0^{\pi}\sin\theta\mathrm{d}\theta\,\mathbf{f}_{\lambda,\ell m}(\hat{\mathbf{r}})\cdot\mathbf{f}^*_{\lambda',\ell' m'}(\hat{\mathbf{r}}) = \delta_{\lambda\lambda'}\delta_{\ell m}\delta_{\ell' m'}. \tag{2.41}$$

Importantly, the vector quantities $\mathbf{\Lambda}^{(j)}_{\lambda,\ell m}(k\mathbf{r})$ exhibit a useful property in that their curl is proportional to the vectors themselves [16]:

$$\frac{\nabla\times}{k}\mathbf{\Lambda}^{(j)}_{\lambda,\ell m}(k\mathbf{r}) \quad = \quad \lambda\mathbf{\Lambda}^{(j)}_{\lambda,\ell m}(k\mathbf{r}). \tag{2.42}$$

In other words, $\mathbf{\Lambda}^{(j)}_{\lambda,\ell m}(k\mathbf{r})$ are eigenstates of the helicity operator $\frac{\nabla\times}{k}$ with eigenvalue λ. Such fields are known as Beltrami fields [97, 98], but will be referred to as helical fields in this thesis.

In Chapter 4, far fields will be considered. Correspondingly, one can utilise an approximation to simplify the expressions for scattered fields. This simplification is achieved by making use of the asymptotic behaviour of the Hankel functions

$$z^{(3)}_{\alpha,\ell}(x) \xrightarrow{x>>1} \begin{cases} \dfrac{\mathrm{e}^{\mathrm{i}x}}{x}(-\mathrm{i})^\ell \quad \text{for} \quad \alpha = \mathrm{N} & (2.43) \\ \dfrac{\mathrm{e}^{\mathrm{i}x}}{x}(-\mathrm{i})^{\ell+1} \quad \text{for} \quad \alpha = \mathrm{M}, & (2.44)\end{cases}$$

where the $\mathcal{O}(1/x^2)$ terms are negligible and therefore ignored.

Finally, by substituting Eqs. (2.43) and (2.44) into Eq. (2.38), one obtains the expression for the far-field helical VSHs $\left[\mathbf{\Lambda}^{(3)}_{\lambda,\ell m}(k\mathbf{r})\right]^{\mathrm{ff}}$ given by

$$\left[\mathbf{\Lambda}^{(3)}_{\lambda,\ell m}(k\mathbf{r})\right]^{\mathrm{ff}} \quad = \quad (-\mathrm{i})^{\ell}\, \mathbf{f}_{\lambda,\ell m}(\hat{\mathbf{r}})\, \frac{\mathrm{e}^{\mathrm{i}kr}}{kr}, \tag{2.45}$$

where the 'ff' superscript denotes 'far field'.

In the next subsection, the VSHs will be used to construct the incident and scattered fields.

2.2.2 The T-matrix of an arbitrary object

One is now at a point where the incident and scattered fields can be expressed in terms of VSHs. For now, this will be done in the parity basis using $\mathbf{M}^{(j)}_{\ell m}(k\mathbf{r})$ and $\mathbf{N}^{(j)}_{\ell m}(k\mathbf{r})$. The analogous treatment using the helical VSHs $\mathbf{\Lambda}^{(j)}_{\lambda,\ell m}(k\mathbf{r})$ will be discussed in Chapter 4.

Consider a object of arbitrary shape illuminated by a plane wave electric field $\mathbf{E}_{\mathrm{i}}(\mathbf{r})$ of the form

$$\mathbf{E}_{\mathrm{i}}(\mathbf{r}) = \mathbf{E}_0 \mathrm{e}^{\mathrm{i}k_{\mathrm{i}}\hat{\mathbf{k}}_{\mathrm{i}}\cdot\mathbf{r}}, \tag{2.46}$$

where

$$\mathbf{E}_0 \cdot \hat{\mathbf{k}}_{\mathrm{i}} = 0\,, \tag{2.47}$$

k_{i} is the wavenumber of the incident field in the embedding medium containing the object and $\hat{\mathbf{k}}_{\mathrm{i}} = \mathbf{k}_{\mathrm{i}}/k_{\mathrm{i}}$ is the unit wave vector. The field $\mathbf{E}_{\mathrm{i}}(\mathbf{r})$ can be expanded in terms of the vector spherical harmonics $\mathbf{M}^{(1)}_{\ell m}(k_{\mathrm{i}}\mathbf{r})$ and $\mathbf{N}^{(1)}_{\ell m}(k_{\mathrm{i}}\mathbf{r})$ defined in Eqs (2.31) and (2.32) as follows [17, Eq. (5.2)]:

$$\mathbf{E}_{\mathrm{i}}(\mathbf{r}) = \sum_{\ell=1}^{\infty}\sum_{m=-\ell}^{\ell}\left[a_{\ell m}\mathbf{M}^{(1)}_{\ell m}(k_{\mathrm{i}}\mathbf{r}) + b_{\ell m}\mathbf{N}^{(1)}_{\ell m}(k_{\mathrm{i}}\mathbf{r})\right], \tag{2.48}$$

where $a_{\ell m}$ and $b_{\ell m}$ are expansion coefficients [17, Eqs (5.4, 5.5)]. Recall for numerical purposes, the infinite sum needs to be capped at a maximum multipolar order $\ell_{\max}$.

Similarly, the scattered field $\mathbf{E}_{\mathrm{s}}(\mathbf{r})$ can be written in terms of the scattering expansion coefficients $p_{\ell m}$ and $q_{\ell m}$ as [17, Eq. (5.3)]

$$\mathbf{E}_{\mathrm{s}}(\mathbf{r}) = \sum_{\ell=1}^{\infty}\sum_{m=-\ell}^{\ell}\left[p_{\ell m}\mathbf{M}^{(3)}_{\ell m}(k_{\mathrm{i}}\mathbf{r}) + q_{\ell m}\mathbf{N}^{(3)}_{\ell m}(k_{\mathrm{i}}\mathbf{r})\right], \quad r > r_\sigma, \tag{2.49}$$

where r_σ is the radius of the smallest circumscribing sphere surrounding the object. It should be emphasised that Eq. (2.49) is only valid when $r > r_\sigma$, where $r = |\mathbf{r}|$ (c.f. Fig 2.1). Note that the (1) superscript in Eq. (2.48) corresponding to the spherical Bessel function $j(k_{\mathrm{i}}r)$ of the first kind is used for the incident field. Conversely, the superscript (3) in Eq. (2.49) corresponds to the spherical Hankel function of the first kind $h(k_{\mathrm{i}}r)$ used for the scattered field. This correct choice of function ensures that the incident field is finite at the origin and the scattered field obeys an outgoing radiation condition. According to the

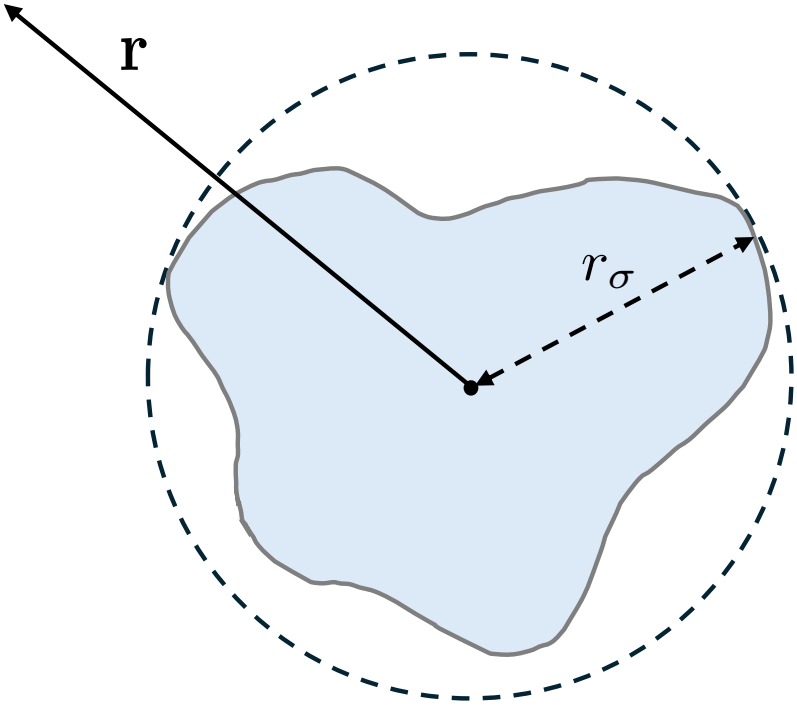

Figure 2.1: An arbitrary scatterer (blue) surrounded by the smallest circumscribing sphere (dashed circle) with radius r_σ. The vector $\mathbf{r}$ corresponds to the point at which the scattered field is observed.

radiation condition, the transverse component of the field decays as $1/r$, while the radial part decays even faster for large r.

Upon obtaining the scattered field $\mathbf{E}_\mathrm{s}(\mathbf{r})$, one can now relate its expansion coefficients to those of the incident field $\mathbf{E}_\mathrm{i}(\mathbf{r})$ as [17, Eqs (5.6, 5.7)]

$$p_{\ell m} = \sum_{\ell'=1}^{\infty} \sum_{m'=-\ell'}^{\ell'} (T^{\mathrm{NN}}_{\ell m \ell' m'} a_{\ell' m'} + T^{\mathrm{NM}}_{\ell m \ell' m'} b_{\ell' m'}) \tag{2.50}$$

$$q_{\ell m} = \sum_{\ell'=1}^{\infty} \sum_{m'=-\ell'}^{\ell'} (T^{\mathrm{MN}}_{\ell m \ell' m'} a_{\ell' m'} + T^{\mathrm{MM}}_{\ell m \ell' m'} b_{\ell' m'}), \tag{2.51}$$

where $T^{\mathrm{NN}}_{\ell m \ell' m'}$, $T^{\mathrm{NM}}_{\ell m \ell' m'}$, $T^{\mathrm{MN}}_{\ell m \ell' m'}$ and $T^{\mathrm{MM}}_{\ell m \ell' m'}$ represent the electric-electric, electric-magnetic, magnetic-electric and magnetic-magnetic components of the transition matrix $\mathbf{T}$, commonly known as the T-matrix, where

$$\mathbf{T} = \begin{pmatrix} \mathbf{T}_{\mathrm{NN}} & \mathbf{T}_{\mathrm{NM}} \\ \mathbf{T}_{\mathrm{MN}} & \mathbf{T}_{\mathrm{MM}} \end{pmatrix} \tag{2.52}$$

and each element of $\mathbf{T}$ is a $\ell_{\max}(\ell_{\max}+2) \times \ell_{\max}(\ell_{\max}+2)$ matrix for the considered maximum multipolar order $\ell_{\max}$. In matrix form, Eqs (2.50) and (2.51) can be expressed as

$$\begin{pmatrix} \mathbf{p} \\ \mathbf{q} \end{pmatrix} = \mathbf{T} \begin{pmatrix} \mathbf{a} \\ \mathbf{b} \end{pmatrix}. \tag{2.53}$$

The application of the T-matrix is presented pictorially in Fig. 2.2.

From the T-matrix, one can also define the S-matrix $\mathbf{S}$, which relates incoming to outgoing fields and is defined as [17]

$$\mathbf{S} = \mathbf{I} + 2\mathbf{T}. \tag{2.54}$$

The difference between incident and incoming fields is that an incident field contains both incoming and outgoing components [99]. The incoming component is the total incoming field, while the outgoing part combined with the scattered field form the outgoing field. For example, in Chapter 6 where scattering by molecules is considered, the incident field is a plane wave. After converting the incident field to the spherical basis, its dipolar components interact with the molecules to produce the scattered field. The outgoing component of the incident field in this case contains the higher-order multipolar components that simply pass through the molecules without interacting with them.

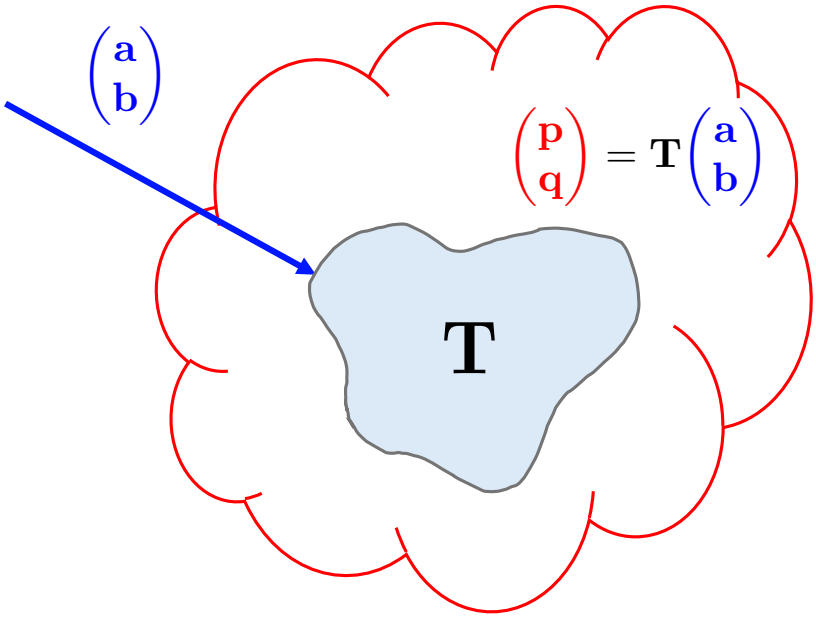

Figure 2.2: A visual depiction of how the T-matrix $\mathbf{T}$ links an incident field to a scattered field. The incident field (blue) has expansion coefficients $(\mathbf{a}, \mathbf{b})$. The scattered field (red) expansion coefficients $(\mathbf{p}, \mathbf{q})$ are obtained by applying $\mathbf{T}$, which depends on the geometry and material of the scatterer, to the incident field expansion coefficients.

2.2.3 The T-matrix of a dielectric sphere

In Chapter 4, electromagnetic scattering by a single dielectric sphere is explored. Here, the $\mathbf{T}_{\mathrm{NM}}$ and $\mathbf{T}_{\mathrm{MN}}$ components of $\mathbf{T}$ disappear such that

$$\mathbf{T}_{\mathrm{S}} = \begin{pmatrix} \mathbf{T}_{\mathrm{NN}} & 0 \\ 0 & \mathbf{T}_{\mathrm{MM}} \end{pmatrix}, \tag{2.55}$$

where the 'S' subscript stands for 'sphere'. Moreover, the elements of $\mathbf{T}_{\mathrm{S}}$

$$\mathbf{T}_{\mathrm{NN}} = \begin{pmatrix} a_1 & \dots & 0 \\ \vdots & \ddots & \vdots \\ 0 & \dots & a_{\ell_{\max}} \end{pmatrix}, \tag{2.56}$$

$$\mathbf{T}_{\mathrm{MM}} = \begin{pmatrix} b_1 & \dots & 0 \\ \vdots & \ddots & \vdots \\ 0 & \dots & b_{\ell_{\max}} \end{pmatrix} \tag{2.57}$$

are diagonal matrices and a_ℓ and b_ℓ are the electric and magnetic Mie coefficients defined by [100, Eqs (4.53)]

$$a_\ell = \frac{\mu_{\mathrm{m}} m^2 j_\ell(mx)[x j_\ell(x)]' - \mu_{\mathrm{S}} j_\ell(x)[mx j_\ell(mx)]'}{\mu_{\mathrm{m}} m^2 j_\ell(mx)[x h_\ell(x)]' - \mu_{\mathrm{S}} h_\ell(x)[mx j_\ell(mx)]'} \tag{2.58}$$

and

$$b_\ell = \frac{\mu_{\mathrm{S}} j_\ell(mx)[x j_\ell(x)]' - \mu_{\mathrm{m}} j_\ell(x)[mx j_\ell(mx)]'}{\mu_{\mathrm{S}} j_\ell(mx)[x h_\ell(x)]' - \mu_{\mathrm{m}} h_\ell(x)[mx j_\ell(mx)]'}. \tag{2.59}$$

In these expressions, the prime represents differentiation with respect to the argument of the relevant function, and μ_{m} and μ_{S} are the magnetic permeabilities of the surrounding medium and the sphere, respectively. Moreover, the parameters x and m are respectively defined as

$$x = \frac{R\omega}{c}\sqrt{\epsilon_{\mathrm{m}}(\omega_0)\mu_{\mathrm{m}}(\omega_0)} \tag{2.60}$$

and

$$m = \sqrt{\frac{\epsilon_{\mathrm{S}}(\omega_0)\mu_{\mathrm{S}}(\omega_0)}{\epsilon_{\mathrm{m}}(\omega_0)\mu_{\mathrm{m}}(\omega_0)}}, \tag{2.61}$$

where R is the radius of the sphere, c is the speed of light in vacuum, ω_0 is the frequency of the incident field, and $\epsilon_{\mathrm{m}}(\omega)$ and $\epsilon_{\mathrm{S}}(\omega)$ are the electric permittivities of the surrounding medium and sphere, respectively.

2.2.4 The T-matrix in the helicity basis

Armed with the matrix $\mathbf{T}$ in the parity basis, one can obtain an analogous matrix $\mathbf{T}^{\mathrm{H}}$ in the helicity basis. The matrix $\mathbf{T}^{\mathrm{H}}$ relates incident and scattered helical fields described by helical VSHs defined in Eq. (2.38). Mathematically, the transformation from the parity basis to the helicity basis reads [101, Eq. (2)]

$$\mathbf{T}^{\mathrm{H}} = \mathbf{P}^{-1}\mathbf{T}\mathbf{P}, \tag{2.62}$$

where the 'H' superscript denotes the helicity basis and

$$\mathbf{P} = \frac{1}{\sqrt{2}}\begin{pmatrix} 1 & 1 \\ 1 & -1 \end{pmatrix} \tag{2.63}$$

is the transformation matrix. Explicitly, $\mathbf{T}^{\mathrm{H}}$ can be written as

$$\mathbf{T}^{\mathrm{H}} = \begin{pmatrix} \mathbf{T}_{++} & \mathbf{T}_{+-} \\ \mathbf{T}_{-+} & \mathbf{T}_{-} \end{pmatrix} \tag{2.64}$$

where $\mathbf{T}_{++}$, $\mathbf{T}_{+-}$, $\mathbf{T}_{-+}$, $\mathbf{T}_{-}$ represent the plus-plus, plus-minus, minus-plus and minus-minus helicity components of $\mathbf{T}^{\mathrm{H}}$, respectively.

In Chapter 4, the helicity T-matrix of a dielectric sphere is required. In this case, $\mathbf{T}^{\mathrm{H}}$ reduces to

$$\mathbf{T}^{\mathrm{H}} = \frac{1}{2}\begin{bmatrix} (\mathbf{T}_{\mathrm{NN}} + \mathbf{T}_{\mathrm{MM}}) & (\mathbf{T}_{\mathrm{NN}} - \mathbf{T}_{\mathrm{MM}}) \\ (\mathbf{T}_{\mathrm{NN}} - \mathbf{T}_{\mathrm{MM}}) & (\mathbf{T}_{\mathrm{NN}} + \mathbf{T}_{\mathrm{MM}}) \end{bmatrix}, \tag{2.65}$$

such that the components $T_{\lambda_{\mathrm{s}},\lambda_{\mathrm{i}},\ell}$ of $\mathbf{T}^{\mathrm{H}}$ are given by

$$T_{\lambda_{\mathrm{s}},\lambda_{\mathrm{i}},\ell} = a_\ell + \lambda_{\mathrm{i}}\lambda_{\mathrm{s}} b_\ell \,. \tag{2.66}$$

In the previous equation, λ_{i} and λ_{s} are the helicities of the incident and scattered fields, respectively.

2.2.5 Rotating the T-Matrix

In Chapter 6 necessary to rotate the T-matrix. Rotating a T-matrix corresponds to rotating the scattering object itself, and allows one to observe the scattering pattern for an arbitrary incident field angle. The rotated T-matrix operator $\mathbf{T}_{\mathrm{R}}(\Psi, \Theta, \Phi)$ described by the three Euler angles $\Psi \in [0, 2\pi), \Theta \in [0, \pi], \Phi \in [0, 2\pi)$ is given by

$$\mathbf{T}_{\mathrm{R}}(\Psi, \Theta, \Phi) = \mathbf{R}(\Psi, \Theta, \Phi)\mathbf{T}\mathbf{R}^{-1}(\Psi, \Theta, \Phi), \tag{2.67}$$

where $\mathbf{R}(\Psi, \Theta, \Phi)$ is the rotation matrix. To carry out T-matrix rotations, the program *treams* was utilised [92], where the rotation follows the $z - y - z$ convention. In other words, the first rotation is about the z-axis, the second about the y-axis and the third about the z-axis. Furthermore, Eq. (2.67) is also valid for the helicity T-matrix $\mathbf{T}^{\mathrm{H}}$.

In this section, the VSHs in the parity basis and helicity basis were defined. It was then shown how VSHs can be used to describe electromagnetic fields as a sum of constituent multipoles. The T-matrix formalism was also outlined, which links incident fields to scattered fields. The T-matrix of a dielectric sphere required in Chapter 4 was highlighted. Moreover, it was shown how to transform a T-matrix from the parity to the helicity basis, as well as how to rotate it. As an extension to a single scatterer, periodic and stratified media will be discussed in the following section.

2.3 Scattering by periodic and stratified media

In addition to individual objects, the scatterer can also be a composite system. One example is a periodic, two-dimensional array of spheres infinitely extended in the x-y plane, as will be the case in Chapter 5. To determine the scattered field by such a structure, one requires what is known as the re-normalised T-matrix given by [102, Eq. (17)]

$$\mathbf{T}_{\mathrm{ren}} = \left(\mathbf{I} - \mathbf{T}\sum_{\mathbf{R}\neq 0} \mathbf{C}_{\mathrm{s}}(-\mathbf{R})\mathrm{e}^{\mathrm{i}\mathbf{k}_{\parallel}(\omega)\mathbf{R}}\right)^{-1} \mathbf{T} \,. \tag{2.68}$$

In Eq. (2.68), $\mathbf{T}$ is the T-matrix of a constituent sphere, $\mathbf{R}$ is a two-dimensional lattice vector, $\mathbf{C}_\mathrm{s}(-\mathbf{R})$ is a translation matrix and $\mathbf{k}_\parallel$ is the component of the wave vector of the incident plane wave with frequency ω parallel to the lattice. In Chapter 5, only plane waves of normal incidence will be considered such that $\mathbf{k}_\parallel = \mathbf{0}$. The re-normalised T-matrix reveals information about the optical response of a scatterer in a two-dimensional lattice. Armed with $\mathbf{T}_\mathrm{ren}$, one can compute the scattered electric field of the lattice (cf. Eqs. (21, 22) from Ref. [102]) and finally the S-matrix $\mathbf{S}$. Recall that the S-matrix relates the incoming field to the outgoing field.

Additionally, one can add an embedding to the spherical array. By combining the lattice with the embedding, one forms a stacked structure that requires a new approach to determine the outgoing field. This new formalism should take into account lattice interactions and the effects each layer in the stack has on the outgoing field. A layer can take the form of either a homogeneous slab, a two-dimensional lattice or an interface between two materials. A depiction of a stack is given in Fig. 2.3. In Fig. 2.3, the stack contains the surrounding vacuum, two slabs forming the embedding, a two-dimensional lattice of spheres and two interfaces.

Since the structure is infinitely extended in two dimensions, the natural way to express the electric field $\mathbf{E}(\mathbf{r})$ leaving a given layer is as a sum of plane waves. For an electric field with general expansion coefficients $\eta_{\mathbf{g},\,\lambda,\,d}$ and wave vector $\mathbf{k}_{\mathbf{g},\,\lambda,\,d}$, one has that [102, Eq. (5)]

$$\mathbf{E}(\mathbf{r}) = \sum_{\lambda=\pm1} \sum_{d=\uparrow\downarrow} \sum_{\mathbf{g}} \eta_{\mathbf{g},\,\lambda,\,d}\, \hat{\mathbf{e}}_\lambda(\mathbf{k}_{\mathbf{g},\,\lambda,\,d}) \mathrm{e}^{\mathrm{i}\mathbf{k}_{\mathbf{g},\,\lambda,\,d}\cdot\mathbf{r}}\,. \tag{2.69}$$

In the previous equation, λ is the helicity of the incident plane wave and $\hat{\mathbf{e}}_\lambda(\mathbf{k}_{\mathbf{g},\,\lambda,\,d})$ is the polarisation vector. The vectors $\mathbf{g}$ are reciprocal lattice vectors and represent the allowed diffraction orders, while the quantity $d = \uparrow\downarrow$ denotes a plane wave propagating in the $+z$- ($\uparrow$) or $-z$- ($\downarrow$) direction. In Chapter 5, only zeroth order diffraction will be considered, where $\mathbf{g} = \mathbf{0}$. Furthermore, since the incident plane wave propagates along the $+z$-axis, one has $\mathbf{k}_{\mathbf{g},\,\lambda,\,d} = \mathbf{k}_{\mathbf{0},\,\lambda,\,\uparrow}$.

The expansion coefficients for a field entering or leaving the half-space above a layer (denoted by the subscript '2') are related to those for a field entering or leaving the half-space below (denoted by the subscript '1') in matrix form as [102, Eq. (6)]:

$$\begin{pmatrix} \boldsymbol{\eta}_{2,\uparrow} \\ \boldsymbol{\eta}_{1,\downarrow} \end{pmatrix} = \begin{pmatrix} \mathbf{S}_{\uparrow\uparrow} & \mathbf{S}_{\uparrow\downarrow} \\ \mathbf{S}_{\downarrow\uparrow} & \mathbf{S}_{\downarrow\downarrow} \end{pmatrix} \begin{pmatrix} \boldsymbol{\eta}_{1,\uparrow} \\ \boldsymbol{\eta}_{2,\downarrow} \end{pmatrix}. \tag{2.70}$$

where $\mathbf{S}_{dd'}$ are S-matrices linking two adjacent layers. Qualitatively, the coefficients on the left of Eq. (2.70) represent a field outgoing from a layer, while those on the right correspond to a field incoming on a layer.

The power of the above formalism is evident in its recursive application. To obtain the total outgoing field leaving a stack, one can successively apply the S-matrices for each layer in Eq. (2.70). For a more in-depth discussion about this iterative technique, one can refer to Ref. [103]. From the incoming and outgoing expansion coefficients, one can obtain the corresponding reflectance and transmittance [102]. The reflectance and transmittance measure how much of an incoming wave is reflected or transmitted, respectively. In Chapter 5, the reflectance corresponding to the system shown in Fig 2.3 will be obtained using *treams* [92]. For this structure, five S-matrices are required: two for the interfaces, two for the slabs and one for the lattice.

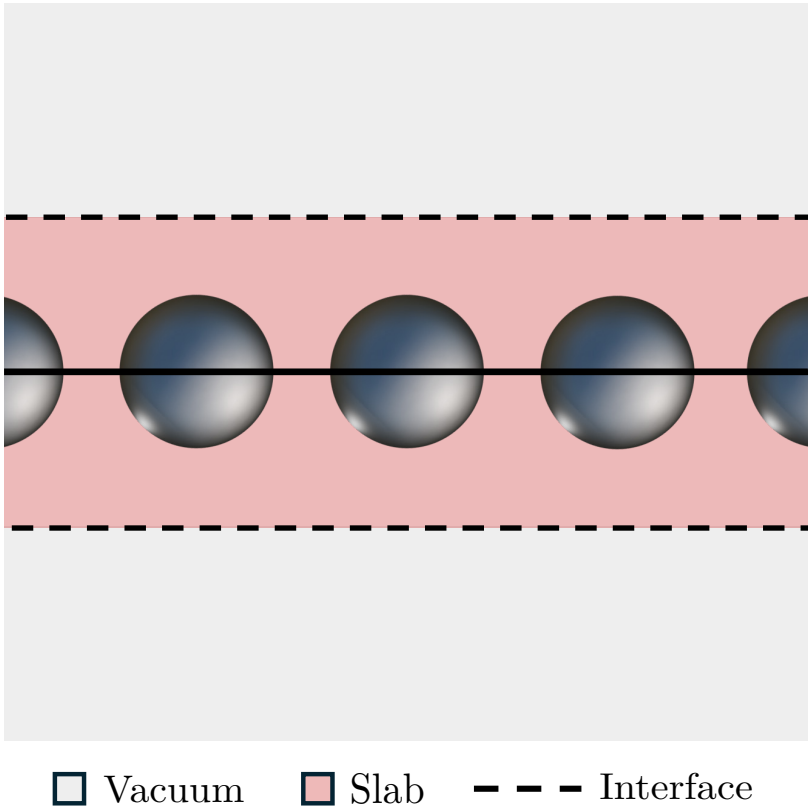

Figure 2.3: A stack consisting of two homogeneous slabs and a lattice of spheres. The stack is suspended in a vacuum. The dashed lines represent interfaces between two layers, while the solid line depicts the joining point of the two slabs.

2.4 Circular dichroism (CD) and rotational averaging

Circular dichroism (CD) is a prime quantity in the that describes the difference in the absorptance or transmittance of left- and right-handed circularly-polarised waves by an object [80–87, 104–107]. Circular dichroism relating to absorption is known as absorption CD (ACD), while that relating to transmission is called transmission CD (TCD). In this section, both types of CD will be discussed, beginning with ACD.

2.4.1 Absorption CD (ACD)

The determination of the ACD of a object reveals important details about its internal structures, an example being exploring the secondary structure of molecules such as proteins [108].

For a given direction corresponding to a wave vector $\mathbf{k}$, the ACD $\Delta\mathcal{A}(\mathbf{k})$ is given by

$$\Delta\mathcal{A}(\mathbf{k}) = A^{+}(\mathbf{k}) - A^{-}(\mathbf{k}), \tag{2.71}$$

where $A^{+}(\mathbf{k})$ and $A^{-}(\mathbf{k})$ are the absorptances of the left- and right-handed circularly-polarised waves with helicities $\lambda = +1$ and $\lambda = -1$, respectively. To obtain expressions for the absorptances, one requires the use of the S-matrix in the helicity basis $\mathbf{S}^{\mathrm{H}}$ which relates helical

incoming to outgoing waves. The matrix $\mathbf{S}^{\mathrm{H}}$ is related to $\mathbf{T}^{\mathrm{H}}$ (Eq. (2.64)) as [99, Eq. (S16)]

$$\mathbf{S}^{\mathrm{H}} = \mathbf{I} + 2\mathbf{T}^{\mathrm{H}}, \tag{2.72}$$

where $\mathbf{I}$ is the identity matrix with dimensions $\ell_{\max}(\ell_{\max}+2) \times \ell_{\max}(\ell_{\max}+2)$ and $\ell_{\max}$ is defined directly after Eq. (2.27).

As per [99, Eq. (S17)], the absorptances $A^{\pm}(\mathbf{k})$ are defined as the difference of the magnitudes squared of the corresponding incoming and outgoing field coefficients, where

$$A^{\pm}(\mathbf{k}) = \boldsymbol{a}^{\pm\dagger}(\mathbf{k})\boldsymbol{a}^{\pm}(\mathbf{k}) - \boldsymbol{a}^{\pm\dagger}(\mathbf{k})\mathbf{S}^{\mathrm{H}\dagger}\mathbf{S}^{\mathrm{H}}\boldsymbol{a}^{\pm}(\mathbf{k})\,. \tag{2.73}$$

The vectors $\boldsymbol{a}^{\pm}(\mathbf{k})$ contain the multipolar expansion coefficients of the incoming wave, where the '$+$' and '$-$' superscripts refer to incoming waves of pure positive and negative helicity, respectively. Explicitly, these vectors are given by

$$\boldsymbol{a}^{+}(\mathbf{k}) = \begin{bmatrix} \boldsymbol{a}^{+}_{\ell_{\max}(\ell_{\max}+2)}(\mathbf{k}) \\ \mathbf{0}_{\ell_{\max}(\ell_{\max}+2)} \end{bmatrix} \tag{2.74}$$

$$\boldsymbol{a}^{-}(\mathbf{k}) = \begin{bmatrix} \mathbf{0}_{\ell_{\max}(\ell_{\max}+2)} \\ \boldsymbol{a}^{-}_{\ell_{\max}(\ell_{\max}+2)}(\mathbf{k}) \end{bmatrix}, \tag{2.75}$$

where $\mathbf{0}$ is the zero vector. The subscript $\ell_{\max}(\ell_{\max}+2)$ represents that each subvector has dimensions $\ell_{\max}(\ell_{\max}+2) \times 1$.

Examples of ACD spectra generated by Marjan Krstić using TURBOMOLE [109] are given in Figs 2.4 and 2.5 for B-DNA and two types of chlorophyll molecules (chlorophyll *a* and chlorophyll *b*), respectively. Technically, the spectra in Figs 2.4 and 2.5 show what is known as the rotationally averaged ACD (RAACD). The RAACD is obtained by illuminating an object from all directions $\mathbf{k}$ (as done in Ref. [110]), obtaining the ACD signals in each direction and dividing the sum of every ACD value by the number of illumination directions. The more illumination directions considered, the more accurate the result. A more detailed treatment of rotational averaging will be given in Chapter 6.

2.4.2 Transmission CD (TCD)

Another type of CD is the transmission circular dichroism (TCD) $\Delta\mathcal{T}(\mathbf{k})$, which is the difference between the transmittances $T^{\pm}(\mathbf{k})$ of right- and left-handed circularly-polarised light. Qualitatively, one has

$$\Delta\mathcal{T}(\mathbf{k}) = T^{-}(\mathbf{k}) - T^{+}(\mathbf{k}). \tag{2.76}$$

When defining the transmittances $T^{\pm}(\mathbf{k})$, one should usually assume a periodic scatterer to conform with the formalism described in Section 2.3. In Chapter 6, however, the TCD of a molecule illuminated by a plane wave will be investigated. Due to the small size of the molecule, only a dipolar scattering response is recorded, while the higher-order components of the incoming field pass straight through. For this reason, one cannot simply apply the S-matrix defined in Eq. (2.54) to obtain the outgoing field. For dipolar scattering, the T-matrix in Eq. (2.54) would only have dimensions of 6×6. By correspondingly restricting the dimensions of the identity matrix in Eq. (2.54), one would erroneously ignore higher-order components of the outgoing field. As a result, a correction to account for the higher-order terms is required. A more in-depth treatment of this correction will be given in Chapter 6.

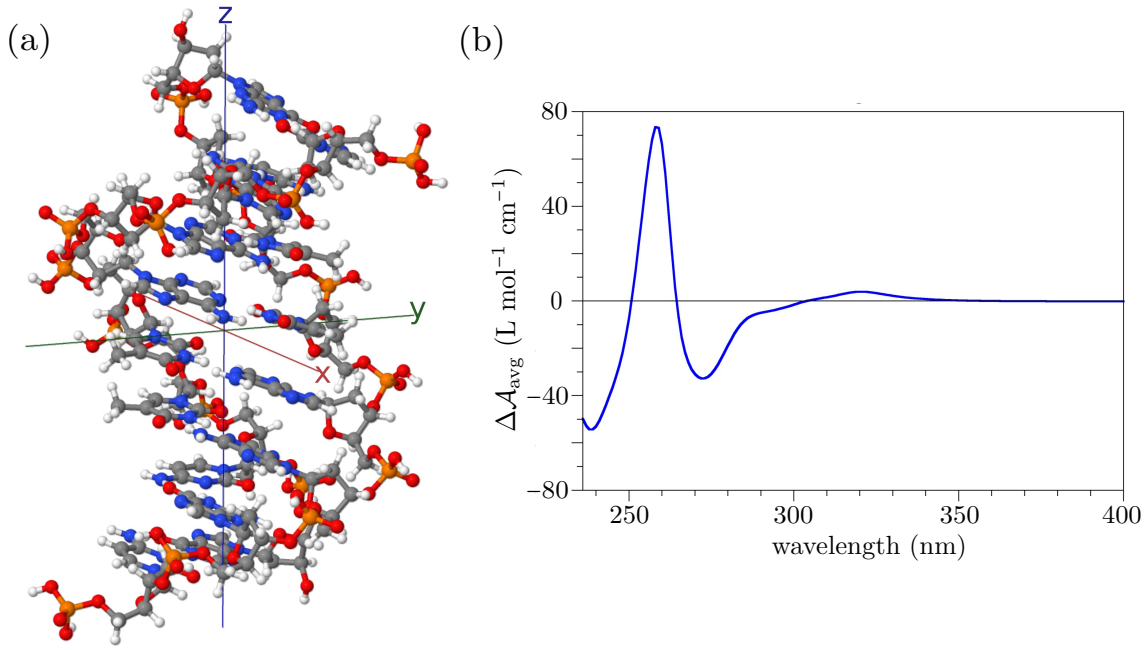

Figure 2.4: In tile (a), a B-DNA molecule is depicted; tile (b) contains its RAACD spectrum. Adapted from [P3] under the CC BY 4.0 license.

2.5 Summary

In this chapter, the theoretical background relating to electrodynamics was covered. To begin, Maxwell's equations were discussed. The vector Helmholtz equation derived from Maxwell's equations was then outlined, and its elementary solutions were given in both the Cartesian and spherical basis. The elementary solutions in the spherical basis are the vector spherical harmonics (VSHs), which are used to express electromagnetic fields as a sum of their multipolar components. Subsequently, the T-matrix formalism was introduced. The T-matrix relates field expansion coefficients of an incident field to those of a field scattered by an object. Although the scatterer can be arbitrarily shaped, a special case of scattering by a single sphere was highlighted. For individual spheres, the scattering process is described using Mie theory. Following this, it was outlined how one can transform a T-matrix from the parity basis to the helical basis, which links incident and scattered fields described by helical VSHs. A further transformation of a T-matrix, namely a rotation, was also discussed. Rotating the T-matrix corresponds to rotating the scatterer itself, allowing one to observe its scattering response from an arbitrary angle of orientation. As an extension to a single object, the formalism describing scattering by periodic and stratified media was developed. Finally, the concept of circular dichroism was defined. The next chapter addresses the second half of the theoretical background: special relativity.

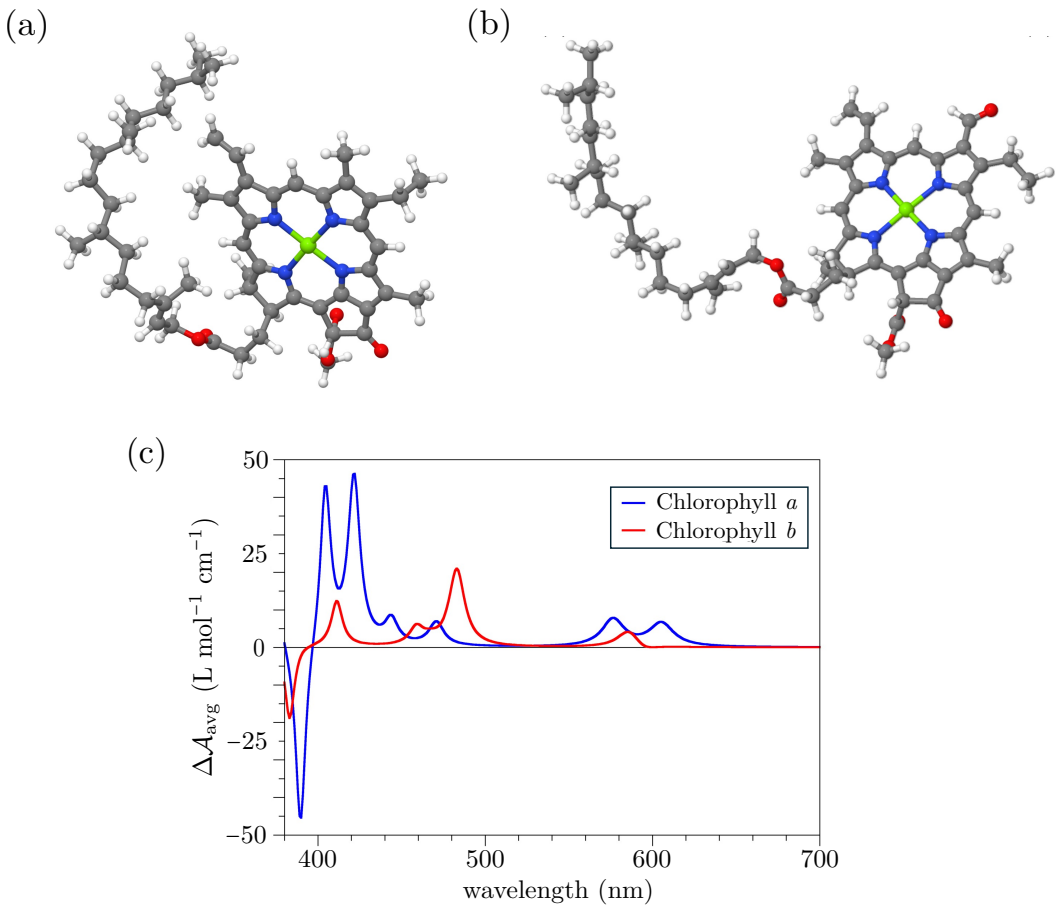

Figure 2.5: Tiles (a) and (b) contain depictions of a chlorophyll *a* and chlorophyll *b* molecule, respectively. Tile (c) shows the RAACD spectra of each molecule. Adapted from [P3] under the CC BY 4.0 license.

3 | Special Relativity

Arguably one of the most significant contributions to physics in the 20th century came in the form of the theory of special relativity, devised by Albert Einstein in his 1905 paper *Zur Elektrodynamik bewegter Körper* (On the Electrodynamics of Moving Bodies) [111]. In this third contribution to his affectionately coined *annus mirabilis* (miracle year) papers, Einstein formed a comprehensive description of special relativity that generalised work done previously by Henri Poincaré and Hendrik Lorentz under the framework of electrodynamics.

As outlined by Einstein, special relativity hinges on two postulates [94]:

1. **Principle of relativity**
   The laws of physics are identical in every inertial reference frame, where no acceleration occurs.

2. **Invariance of the speed of light in free space**
   The speed of light in free space is the same for every observer, independent of their motion relative to the source.

The principle of relativity is of utmost importance in this thesis, as will become evident in Chapters 4 and 6. This first postulate leads to great mathematical simplification by allowing one to employ a frame-hopping method (FHM) when describing the scattering of light by a relativistically moving object. The FHM will enable light scattering calculations in a stationary regime in an inertial reference frame, followed by Lorentz boosting the result back to an external lab frame. The Lorentz boost relates how various geometric and electromagnetic properties are observed in the inertial reference frame compared to the lab frame. It is in the lab frame where all final measurements are observed in later chapters, such as scattered energy and CD.

For a lab frame F with spatial coordinates (x, y, z) and an inertial reference frame F' with coordinates (x', y', z') (cf. Fig. 3.1), the FHM consists of the following steps [31, P1]:

1. The incident field is Lorentz boosted from F to F'.

2. The scattering problem is solved in frame F'.

3. Finally, the scattered field is Lorentz boosted from F' back to F.

In the entire thesis, only Lorentz boosts in the z–direction will be considered. Such a Lorentz boost $\hat{\mathbf{L}}_z(\beta)$ is characterised by the transformation matrix [112]

$$\hat{\mathbf{L}}_z(\beta) = \begin{pmatrix} \gamma & 0 & 0 & -\gamma\beta \\ 0 & 1 & 0 & 0 \\ 0 & 0 & 1 & 0 \\ -\gamma\beta & 0 & 0 & \gamma \end{pmatrix}, \tag{3.1}$$

where

$$\beta = \frac{v}{c}, \quad -1 < \beta < 1, \tag{3.2}$$

v is the speed of the object and c is the speed of light in vacuum. Moreover, the Lorentz factor γ is defined as

$$\gamma = \frac{1}{\sqrt{1-\beta^2}}. \tag{3.3}$$

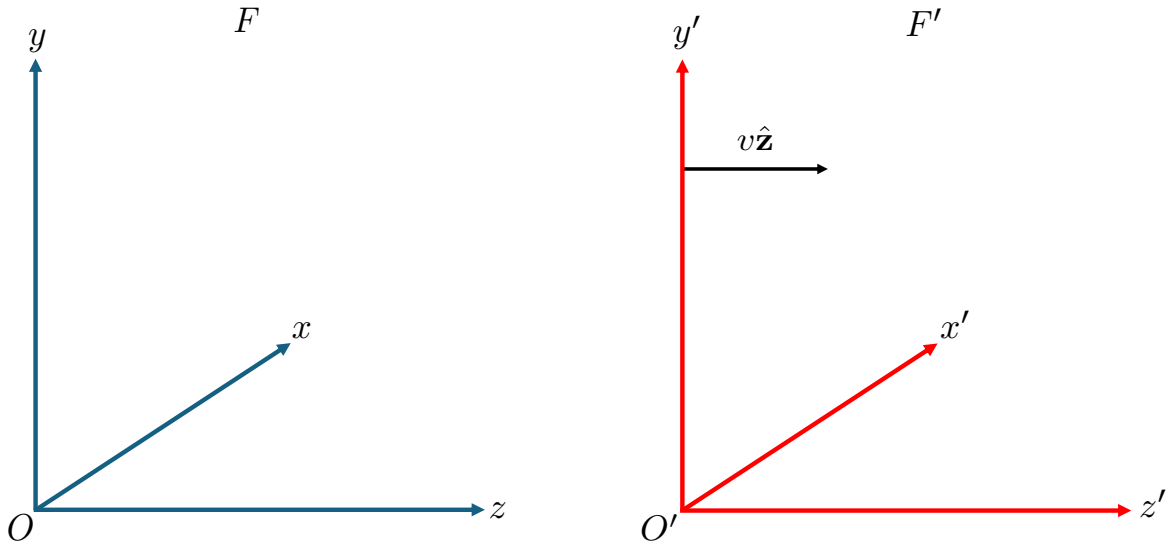

Figure 3.1: The lab frame F with coordinates (x, y, z) is shown on the left. On the right is the boosted frame F' that moves with velocity $v\hat{\mathbf{z}}$ relative to F and is described by coordinates (x', y', z'). Each frame has an origin O and O', respectively.

In the next section, the effects of Lorentz boosting are discussed. Just as frames F and F' are described by different coordinate systems (cf. Fig. 3.1), many quantities like the wavelength of an electromagnetic field and the length of an object are measured differently depending on the location of the observer. Firstly, the Doppler shift of an electromagnetic wave will be discussed, a concept which describes how the wave is perceived depending on the motion of an observer relative to the light source. In the language of reference frames, the wavelength of an electromagnetic wave emitted by a source stationary in frame F is viewed differently in frame F' moving at speed v relative to F. Afterwards, the concept of length contraction will be outlined and used to justify why electromagnetic scattering calculations should be done in frame F' instead of F. This will lead to a discussion on the Lorentz boost of electromagnetic fields. Afterwards, the boosted electric and magnetic fields will be expressed in the helicity basis, as required in later chapters. Finally, the Lorentz invariance of the helicity of an electromagnetic field will be demonstrated.

3.1 Effects arising from Lorentz boosts

3.1.1 The Doppler shift

If an observer in frame F' moves along the z–axis with speed v away from the source field in frame F, they will observe a stretched (redshifted) wave with a longer wavelength compared to that in frame F. Conversely, if the observer in frame F' moves towards the source, the wave would appear compressed (blueshifted) with a shorter wavelength compared to that in frame F. This concept is known as Doppler shifting and is depicted in Fig 3.2. In everyday life, Doppler shifting is often heard when an ambulance with blaring sirens passes by. As the ambulance approaches the observer, the pitch of the sound becomes higher since its wavelength decreases and the frequency correspondingly increases. The opposite occurs when the ambulance moves away from the observer.

Doppler shifting will be of great importance in later chapters since they concern signals sent from Earth to relativistically moving objects in outer space. In all cases, the objects scatter an incident electromagnetic field and are stationary in frame F'. Here, the objects will observe a Doppler–shifted incident wave compared to that viewed on Earth (in frame F). For a wave with wavelength L in frame F, the Doppler–shifted wavelength L' in frame F' is obtained by applying the Lorentz boost operator $\hat{\mathbf{L}}_z(\beta)$ to the four-wavevector $\mathbf{K}(\omega, \mathbf{k}) = (\omega/c, \mathbf{k})^{\mathrm{T}}$ in frame F to obtain that in frame F' denoted by $\mathbf{K}'(\omega', \mathbf{k}') = (\omega'/c, \mathbf{k}')^{\mathrm{T}}$, where

$$\mathbf{K}'(\omega', \mathbf{k}') = \hat{\mathbf{L}}_z(\beta)\mathbf{K}(\omega, \mathbf{k}). \tag{3.4}$$

The 'T' superscript denotes the transpose. In Eq. (3.4), ω and $\mathbf{k}$ are the frequency and three–dimensional wavevector of the plane–wave electromagnetic field in frame F, respectively. The analogous quantities in frame F' are denoted by a prime.

Upon carrying out the operation in Eq. (3.4), one obtains the Doppler–shifted wavelength $L'(\beta)$ given by

$$L'(\beta) = \frac{L}{\Delta(\beta, \theta_{\mathbf{k}})}, \tag{3.5}$$

where

$$\Delta(\beta, \theta_{\mathbf{k}}) = \gamma(1 - \beta\cos\theta_{\mathbf{k}}) \tag{3.6}$$

is the factor representing the Doppler shift for a plane wave with orientation $\theta_{\mathbf{k}}$ with respect to the z-axis. In this chapter, an angle of $\theta_{\mathbf{k}} = 0$ will be considered for demonstration purposes, such that Eq. (3.6) becomes

$$\Delta(\beta) = \sqrt{\frac{1-\beta}{1+\beta}}\,. \tag{3.7}$$

The sign of β dictates whether an object moves in the positive or negative z–direction. When $\beta > 0$, the scatterer moves away from the observer. When $\beta < 0$, the scatterer moves towards the observer (cf. Fig. 3.2). Moreover, one sees in Eq. (3.7) that as β increases, the perceived wavelength L' in frame F' increases, as expected. Likewise, the opposite occurs as β decreases.

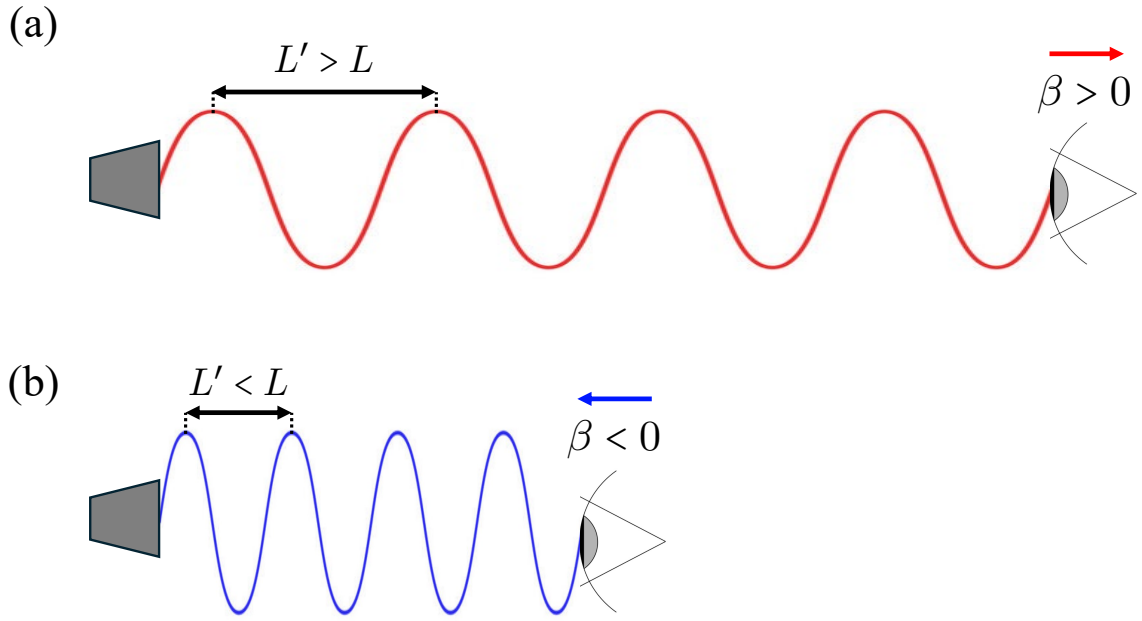

Figure 3.2: A depiction of the Doppler shift, where the wavelength of an electromagnetic field is L in frame F and $L' \neq L$ in frame F'. In (a), the observer in frame F' moves away from the field source in frame F with a speed ratio $\beta > 0$ and sees a red-shifted wave, where $L' > L$. In (b), the observer moves towards the source ($\beta < 0$) and observes a blue-shifted wave ($L' < L$).

In this subsection, the concept of the Doppler shift was introduced, which explains why the position of an observer moving relative to a wave source can affect the perceived wavelength. Both cases, *i.e.*, where an object moves away or towards a light source, were discussed. The next subsection will concern length contraction, a phenomenon that helps one to determine the reference frame in which Mie theory calculations should be performed. Specifically, it will be discussed why length contraction introduces mathematical complexity if the scattering calculation is carried out in frame F instead of F'.

3.1.2 Length contraction

Length contraction is the phenomenon where an object moving in frame F is measured to be compressed compared to its length in frame F', where the object is assumed to be at rest. The length in frame F' is called the proper length or rest length. In any other frame, the length will be compressed. To quantitatively describe length contraction, one needs to consider the relationships between the coordinates (x, y, z) in frame F and the coordinates (x', y', z') in frame F'. For an object stationary in frame F' moving with velocity $v\hat{\mathbf{z}}$ relative to F (cf. Fig. 3.1), the two coordinate systems are linked via the Lorentz boost operator

$\hat{\mathbf{L}}_z(\beta)$ as follows:

$$\begin{pmatrix} ct' \\ x' \\ y' \\ z' \end{pmatrix} = \hat{\mathbf{L}}_z(\beta) \begin{pmatrix} ct \\ x \\ y \\ z \end{pmatrix}, \tag{3.8}$$

such that

$$x' = x, \tag{3.9}$$
$$y' = y, \tag{3.10}$$
$$z' = \gamma(z - \beta ct), \tag{3.11}$$
$$t' = \gamma\left(t - \frac{\beta z}{c}\right). \tag{3.12}$$

One sees from Eq. (3.12) that time also depends on the reference frame (denoted by t in frame F and t' in frame F'). However, to discuss length contraction, explicit reference to time is omitted. The variance in time will be discussed in the next subsection.

An important property of length contraction can already be inferred from Eqs. (3.9)-(3.11). In Eqs. (3.9) and (3.10), the x and y coordinates remain unchanged after the Lorentz boost. As shown by Eq. (3.11), however, the z coordinate does change. The implication of this is that length contraction only occurs in the direction of motion, in this case along the z–axis. For example, a sphere boosted in the z–direction would remain a sphere in frame F', but would be measured as an ellipsoid in frame F due to the length contraction of its radius along the z–axis (cf. Fig. 3.3). The radii in the x and y directions remain unchanged.

To show the length contraction of a sphere's radius along the z-axis, consider two points given by $(0, 0, z_1')$ and $(0, 0, z_2')$ in frame F'. The sphere has radius R' in frame F' and moves in the $+z$–direction with speed v relative to F. In F, the same points are described by $(0, 0, z_1)$ and $(0, 0, z_2)$, where $z_2 > z_1$. In F', the distance D' between the points is given by $D' = z_2' - z_1'$. From Eq. (3.11), one can express D' in terms of the coordinates in frame F as

$$\begin{aligned} D' &= z_2' - z_1' \\ &= \gamma(z_2 - \beta ct_2) - \gamma(z_1 - \beta ct_1) \\ &= \gamma\left[(z_2 - z_1) - \beta c(t_2 - t_1)\right], \end{aligned} \tag{3.13}$$

where t_2 and t_1 are the times in frame F at which the two respective points z_2 and z_1 are measured. Assuming this measurement to occur simultaneously in frame F where $t_1 = t_2$, Eq. (3.13) becomes

$$\begin{aligned} D' &= \gamma\left[(z_2 - z_1) - \beta c(t_2 - t_1)\right] \\ &= \gamma(z_2 - z_1) \\ &= \gamma D, \end{aligned} \tag{3.14}$$

such that

$$D = \frac{D'}{\gamma}, \tag{3.15}$$

where $D = z_2 - z_1$ is the distance between z_1 and z_2 in frame F. In the case of a sphere centred at the origin in frame F' and moving along the $+z$–axis, the radius R' in frame F' can be described by the distance between the points $z_2' = (0, 0, R')$ and $z_1' = (0, 0, 0)$. With this in mind, Eq. (3.15) becomes

$$R_z = \frac{R'}{\gamma}. \tag{3.16}$$

Note that there is a 'z' subscript in R_z but not in R'. This signifies that the radius changes in frame F along the z–axis where $R_z \neq R'$. Since $\gamma > 1$ for a moving object, Eq. (3.16) confirms that the sphere becomes compressed in frame F, where the observer measures it as an ellipsoid. The different geometries can be seen in Fig. 3.3.

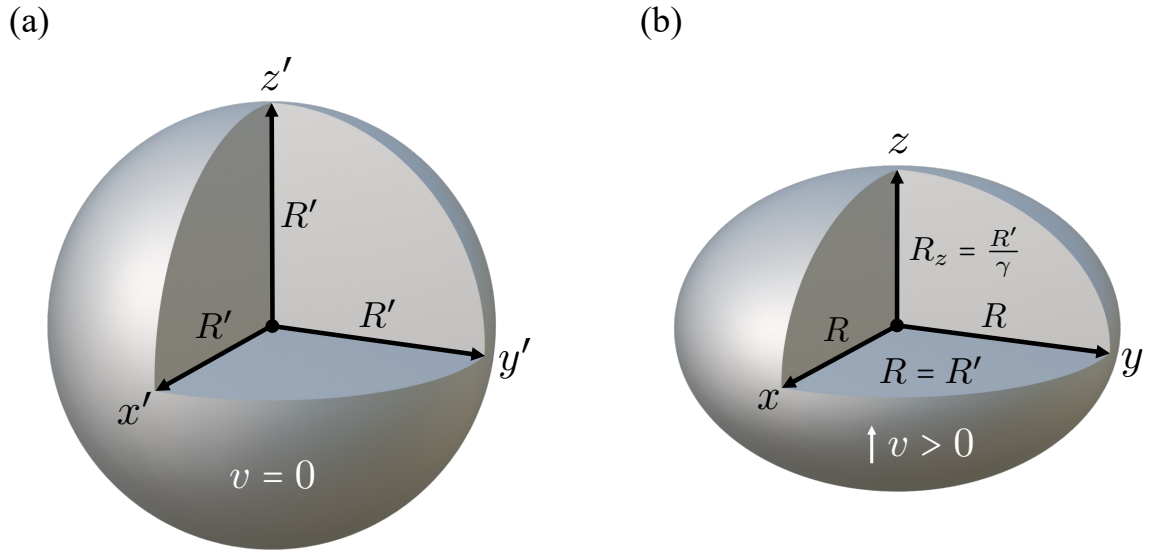

Figure 3.3: The effect of length contraction on a spherical scatterer moving along the z–axis. As shown in (a), the scatterer remains a sphere with radius R' in an inertial frame F'. In (b), it is shown how the object is perceived in the lab frame F. In F, length contraction occurs along the z–axis such that an observer in frame F measures an ellipsoid. Along the z–axis, the radius in frame F is reduced by a factor of $1/\gamma$. The compressed radius is denoted by R_z.

The result shown in Eq. (3.16) demonstrates that one could not directly apply Mie theory in frame F. In F, the scatterer is measured as an ellipsoid. Since Mie theory only pertains to spheres, one cannot implement it in frame F. Herein lies the added mathematical complexity mentioned above if one were to compute scattering calculations in frame F instead of F'. In F', the scatterer remains a sphere so Mie theory can be applied in the usual way here.

In this subsection, the concept of length contraction was introduced, and an explanation was given as to why Mie theory calculations should be carried out in frame F' and not F. Armed with this understanding, the Lorentz boost of an electromagnetic field will be discussed in the following subsection.

3.1.3 The Lorentz boost of electromagnetic fields and energy density

Followed by justifying in the previous subsection why Mie theory calculations should be carried out in frame F' and not in frame F, it is necessary to determine how electric and magnetic fields behave under Lorentz boosts from F to F'. As seen in [31], the electric field $\mathbf{E}'(\mathbf{r}', t')$ and magnetic field $\mathbf{B}'(\mathbf{r}', t')$ in frame F' can be related to those in frame F as

$$\mathbf{E}'(\mathbf{r}', t') = \gamma \left[\mathbf{E}(\mathbf{r}, t) + v\hat{\mathbf{v}} \times \mathbf{B}(\mathbf{r}, t)\right] + (1 - \gamma) \left[\hat{\mathbf{v}} \cdot \mathbf{E}(\mathbf{r}, t)\right] \hat{\mathbf{v}} \tag{3.17}$$

and

$$\mathbf{B}'(\mathbf{r}', t') = \gamma \left[\mathbf{B}(\mathbf{r}, t) - \frac{v\hat{\mathbf{v}} \times \mathbf{E}(\mathbf{r}, t)}{c^2}\right] + (1 - \gamma) \left[\hat{\mathbf{v}} \cdot \mathbf{B}(\mathbf{r}, t)\right] \hat{\mathbf{v}}, \tag{3.18}$$

where $\hat{\mathbf{v}}$ is the boosting direction. Moreover, the space and time coordinates $\mathbf{r}'$ and t' in frame F' are respectively given by

$$\mathbf{r}' = \mathbf{r} + \left[(\gamma - 1)\hat{\mathbf{v}} \cdot \mathbf{r} - \gamma v t\right] \hat{\mathbf{v}} \tag{3.19}$$

and

$$t' = \gamma \left(t - \frac{\beta \hat{\mathbf{v}} \cdot \mathbf{r}}{c}\right). \tag{3.20}$$

Note that Eq. (3.19) collapses to Eqs (3.9)-(3.11) for motion along the z–axis. Furthermore, one sees that time is measured differently depending on the reference frame. Specifically, a clock moving with an object in frame F' relative F would measure less elapsed time compared to a clock held by an observer in frame F. The variance in time explains many arguably counter-intuitive phenomena, including why muons traversing the atmosphere hit the Earth before decaying. An observer on Earth measures the muons' clock to be ticking slowly, meaning the muons reach the Earth before reaching their decay time. From the perspective of the muons, the distance between them and Earth is contracted in line with Eq. (3.15). This means the muons measure a shorter travel distance, thus explaining their survival from the perspective of both reference frames.

As already mentioned, objects moving in the $\hat{\mathbf{v}}$=$\hat{\mathbf{z}}$ direction relative to an incident light source are considered in this thesis. For this specification, Eqs (3.17) and (3.18) become

$$\begin{pmatrix} E'_x \\ E'_y \\ E'_z \end{pmatrix} = \begin{pmatrix} \gamma(E_x - \beta c B_y) \\ \gamma(E_y + \beta c B_x) \\ E_z \end{pmatrix} \tag{3.21}$$

and

$$\begin{pmatrix} B'_x \\ B'_y \\ B'_z \end{pmatrix} = \begin{pmatrix} \gamma(B_x + \frac{\beta}{c} E_y) \\ \gamma(B_y - \frac{\beta}{c} E_x) \\ B_z \end{pmatrix}. \tag{3.22}$$

Interestingly, Eq. (3.21) shows that only the components of $\mathbf{E}(\mathbf{r}, t)$ and $\mathbf{B}(\mathbf{r}, t)$ perpendicular to the direction of motion are affected. Specifically, the magnitudes of the x and y components become larger with speed, meaning an observer in frame F' views an ever-flattening

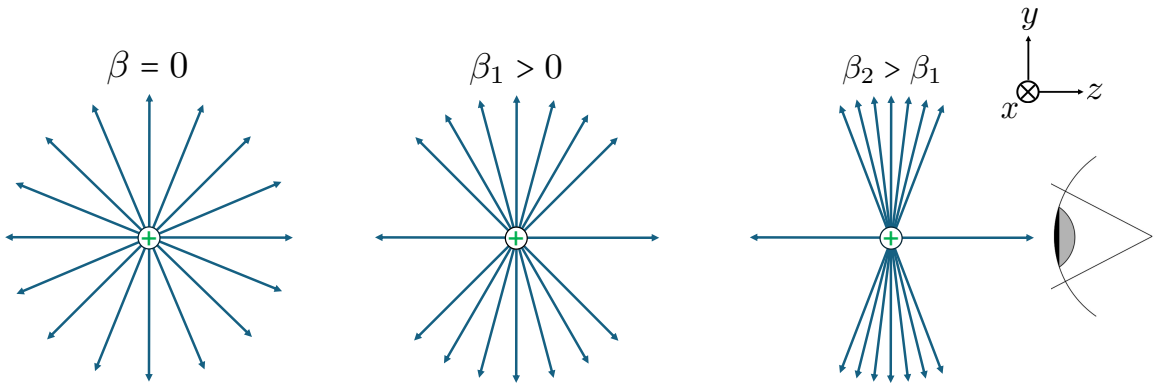

Figure 3.4: How the electric field line distribution of a positive point charge stationary in frame F changes in the y–z plane as an observer in frame F' moves along the $+z$–axis. Depictions for three speed ratios $\beta = 0$, β_1 and β_2 are shown, where $\beta_2 > \beta_1 > 0$.

field as v increases. A classic example of demonstrating this flattening is to consider how the field lines of a point charge stationary in frame F observed from a moving frame F' change with speed (cf. Fig. 3.4). Three speeds are considered, namely $\beta \in \{0, \beta_1, \beta_2\}$, where $\beta_2 > \beta_1 > 0$. For demonstration purposes, only the y–z–plane is depicted.

Another important case is a plane-wave electromagnetic field since plane waves play an important role in all future chapters. The variation of an incident plane-wave electric field illuminating an object will now be examined. Firstly, the electric and magnetic fields will be defined in frame F', since this is the reference frame in which Mie theory calculations must be done. Next, the fields in frame F' will be expressed in terms of the known quantities of the incident field in frame F. For example, the Doppler–shifted wavelength $L'(\beta)$ of the incident light as observed in frame F' must be expressed in terms of the wavelength L in frame F (cf. Eq. (3.5)). Subsequently, the properties of a plane wave will be exploited to allow one to express the magnetic field in terms of the electric field, revealing an explicit dependence of the electromagnetic field amplitudes on β. From this, the Lorentz-boosted energy density will be explored as it provides a direct visualisation of the effect of the varying field amplitudes.

The effect of a Lorentz boost on the amplitude of the field will now be derived mathematically. The focus will mainly be on the electric field during the derivation as one can directly obtain the magnetic field from the result. For demonstration purposes, the time dependence in both reference frames will be dropped, but the result can be extended to all polarisations and times.

Beginning with the derivation, the spatial part of an x-polarised plane wave electric field $\mathbf{E}'(z', \beta)$ in frame F' with wavelength L' and propagating in the $+z$–direction is given by

$$\begin{aligned}\mathbf{E}'(z', \beta) &= \mathbf{E}'_0(\beta) \sin\left(\frac{2\pi z'}{L'(\beta)}\right) \\ &= \hat{\mathbf{x}} E'_0(\beta) \sin\left(\frac{2\pi z'}{L'(\beta)}\right) \\ &= \hat{\mathbf{x}} E'_x(z', \beta), \end{aligned} \tag{3.23}$$

where $L'(\beta)$ is obtained from Eq. (3.5) and $E_0'(\beta)$ is the electric field amplitude in frame F'.

The corresponding magnetic field $\mathbf{B}'(z',\beta)$ polarised in the y–direction is given by

$$\begin{aligned}\mathbf{B}'(z',\beta) &= \mathbf{B}_0'(\beta)\sin\left(\frac{2\pi z'}{L'(\beta)}\right)\\ &= \hat{\mathbf{y}}B_0'(\beta)\sin\left(\frac{2\pi z'}{L'(\beta)}\right)\\ &= \hat{\mathbf{y}}B_y'(z',\beta),\end{aligned} \tag{3.24}$$

where $B_0'(\beta)$ is the magnetic field amplitude in frame F'.

It is now necessary to obtain the fields in frame F' in terms of the known quantities in frame F. Beginning with determining $\mathbf{E}_0'(\beta)$, one finds from Eq. (3.21) that

$$E_0'(\beta) = \gamma(E_0 - \beta c B_0), \tag{3.25}$$

where E_0 and B_0 come from the electric and magnetic fields as perceived in frame F given by

$$\mathbf{E}(z,t) = \hat{\mathbf{x}}E_0\sin\left(\frac{2\pi z}{L}\right) \tag{3.26}$$

and

$$\mathbf{B}(z,t) = \hat{\mathbf{y}}B_0\sin\left(\frac{2\pi z}{L}\right), \tag{3.27}$$

respectively. A value of E_0 will always be assumed.

Using the Maxwell equation given by Eq. (2.3), one can further simplify Eq. (3.25) by writing B_0 in terms of E_0. As mentioned above, this is why it is initially sufficient to only consider the Lorentz boost of the electric field. By substituting Eqs (3.26) and (3.27) into Eq. (2.3), one finds that

$$B_0 = \frac{1}{c}E_0. \tag{3.28}$$

Following this, the final expression for the electric field amplitude in frame F' is obtained upon substitution of Eq. (3.28) into Eq. (3.25), where

$$E_0'(\beta) = E_0\Delta(\beta). \tag{3.29}$$

One sees that the magnetic field amplitude obeys the same relation by substituting Eq. (3.28) into Eq. (3.29), along with the analogous expression in frame F' given by

$$B_0'(\beta) = \frac{1}{c}E_0'(\beta). \tag{3.30}$$

Note that one is allowed to replace the field amplitudes in frame F in Eq. (3.28) with those in frame F' since a plane wave in frame F remains a plane wave when boosted to F'. Also worth noting is the similarity of Eq. (3.29) to Eq. (3.5), where the same Doppler shift factor $\Delta(\beta)$ appears. As a result, both the wavelength L of an electromagnetic field and the field amplitudes change under Lorentz boosts.

Next, the oscillatory part of Eq. (3.23) must be expressed in terms of the known wavelength in frame F. To do this, one can exploit Eq. (3.5) for the Doppler–shifted wavelength and obtain

$$\sin\left(\frac{2\pi z'}{L'}\right) = \sin\left[\frac{2\pi z'\Delta(\beta)}{L}\right]. \tag{3.31}$$

As a result, the complete electric field in frame F' is given by

$$\begin{aligned}\mathbf{E}'(z',\beta) &= \hat{\mathbf{x}}E_0\Delta(\beta)\sin\left[\frac{2\pi z'\Delta(\beta)}{L}\right] \\ &= \hat{\mathbf{x}}E_x'(z',\beta).\end{aligned} \tag{3.32}$$

When F' moves away from F ($\beta > 0$), one sees from Eq. (3.32) that the wavelength of the electric field increases, while the amplitude of the electric field decreases. Conversely, the wavelength decreases and the magnitude of the electric field increases when F' moves towards F ($\beta < 0$). A colour plot showing the variation of $E_x'(z',\beta)$ is given in Fig. 3.5, along with a graph of $E_x'(z',\beta)$ for fixed values of $\beta \in \{-0.6, -0.3, 0, 0.3, 0.6\}$. Recall that the corresponding equation for the magnetic field $\mathbf{B}'(z',\beta)$ can be obtained by substituting Eq. (3.32) into Eq. (2.3), such that

$$B_y'(z',\beta) = \frac{1}{c}E_x'(z',\beta). \tag{3.33}$$

A physical consequence of Eqs (3.32) and (3.33) can be found by considering the energy density $u'(z',\beta)$ of the plane wave in frame F'. The energy density is the energy per unit volume stored in an electromagnetic field. Since the electromagnetic field in frame F' has the same polarisations as in frame F, the equation for $u'(z',\beta)$ is given by [94]

$$u'(z',\beta) = \frac{1}{2}\left[\epsilon_0|E_x'(z',\beta)|^2 + \frac{1}{\mu_0}|B_y'(z',\beta)|^2\right] \tag{3.34}$$

for an object moving along the z–axis.

One can simplify Eq. (3.34) by substituting Eq. (3.33) into Eq. (3.34), where

$$u'(z',\beta) = \epsilon_0|E_x'(z',\beta)|^2, \tag{3.35}$$

thus yielding the final expression for the energy density of a plane wave in frame F'.

A colour plot of $u'(z',\beta)/\epsilon_0$ is given in Fig 3.6 (a). Graphs of $u'(z',\beta)/\epsilon_0$ for fixed speed ratios $\beta \in \{-0.6, -0.3, 0, 0.3, 0.6\}$ are given in Fig. 3.6 (b). When $\beta < 0$, the energy density perceived in frame F' increases with speed. This makes sense, since the amplitude of $E_x'(z',\beta)$ increases by a factor of $\Delta(\beta)$ as β decreases (cf. Eq. (3.32)). Since a wave with a high amplitude carries a large energy density, the energy density correspondingly increases. When $\beta > 0$, the opposite is seen since a wave with a low amplitude carries a lower energy density.

For a wave that isn't infinitely extended in space, the total energy of an electromagnetic field changes under Lorentz boosts [31, P1]. This energy change will be implemented in Chapter 4. Here, the effects of an object's speed on the scattered energy will be considered. In this case, all fields will be expressed in the helicity basis. The reason why will be discussed in the next subsection.

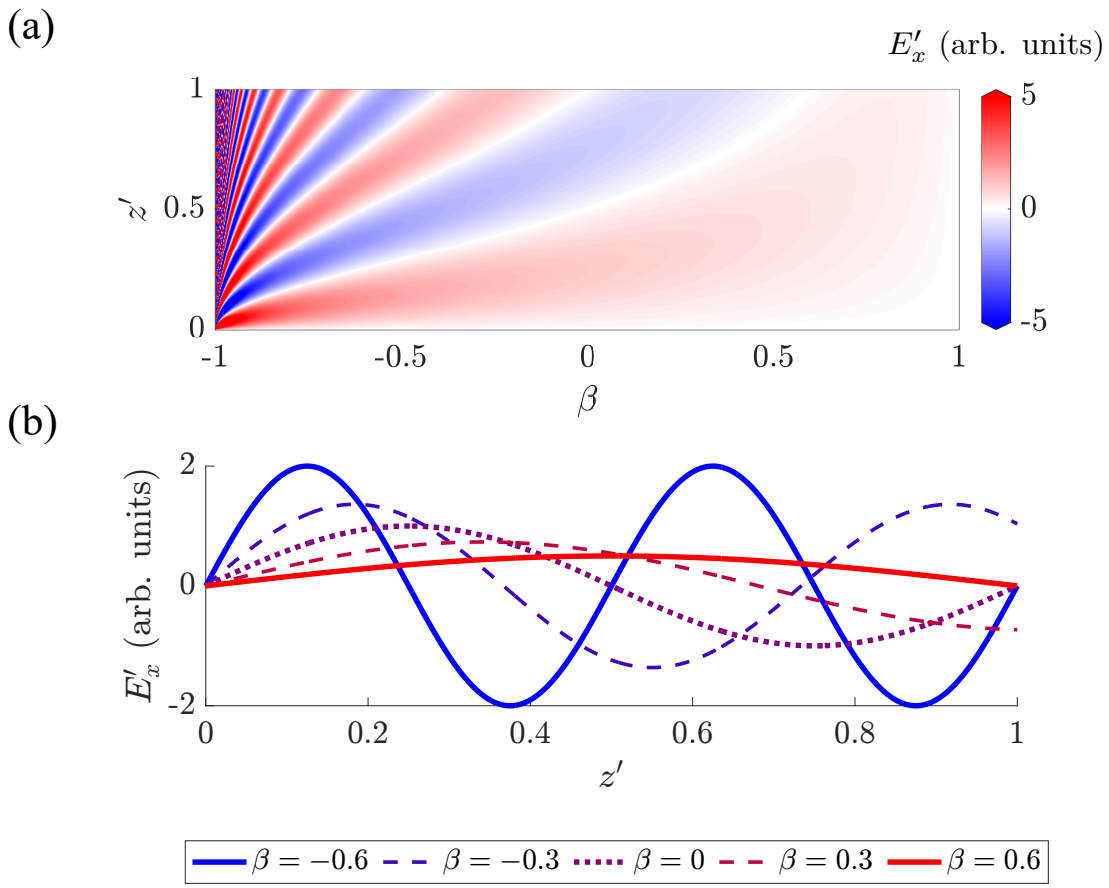

Figure 3.5: In (a), the electric field E'_x in frame F' is given as a function of the speed ratio β and position z'. In (b), the same electric field is given as a function of z' for select β values.

3.1.4 Lorentz boosted fields in the helicity basis

Although relativistic calculations can be carried out in the parity basis by considering transverse electric (TE) and transverse magnetic (TM) modes, it is arguably more practical to consider fields in the helicity basis. The reason for this is that the helicity of an electromagnetic field is invariant under Lorentz boosts [113], which makes calculations easier compared to those using electromagnetic fields in the parity basis. This helicity invariance will be explicitly demonstrated in the next subsection.

For plane waves, the incident electric field in frame F is circularly-polarised with polarisation $\hat{\mathbf{e}}_\lambda(\hat{\mathbf{k}})$ as defined in Eq. (2.39), where

$$\mathbf{E}(\mathbf{r}, t) = \hat{\mathbf{e}}_\lambda(\hat{\mathbf{k}}) E_0 \exp\{\mathrm{i}\omega[(\hat{\mathbf{k}} \cdot \mathbf{r}/c) - t]\}. \tag{3.36}$$

In the above equation, λ is the helicity of the field, ω is the field frequency and $\hat{\mathbf{k}}$ is the unit wavevector that describes the propagation direction. Note that reference to a magnetic field is omitted at this point as the relevant expression will later be directly obtained from $\mathbf{E}(\mathbf{r}, t)$ using Maxwell's equations.

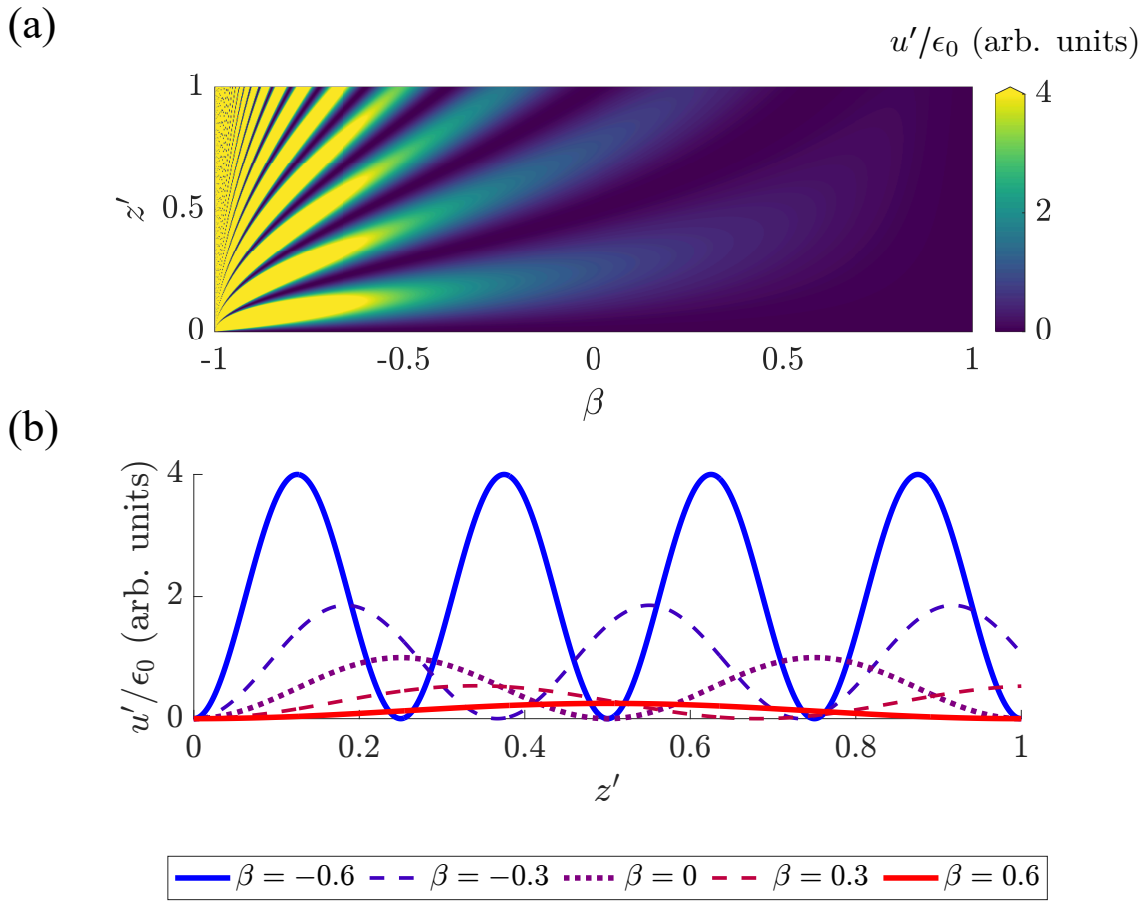

Figure 3.6: In (a), the energy density u' in frame F' normalised with the permittivity of free space ϵ_0 is given as a function of the speed ratio β and position z'. In (b), the same normalised energy density is given as a function of z for select β values.

Fields that take the form of Eq. (3.36) are known as Beltrami fields [97, 98]. In the optics community, such fields are also referred to as helical fields [114]. The latter nomenclature will be used from here on in. A characteristic of helical plane waves is that they are eigenstates of the helicity operator $\frac{\nabla\times}{k}$ [16, 114], which is also present in Eq. (2.42). From (2.42), one finds that

$$\nabla \times \mathbf{E}(\mathbf{r}, t) = \lambda k \mathbf{E}(\mathbf{r}, t). \tag{3.37}$$

Qualitatively speaking, Eq. (3.37) demonstrates that helical fields are directly proportional and parallel to their curl.

The magnetic field $\mathbf{B}(\mathbf{r}, t)$ can be obtained by substituting Eq. (3.37) into Eq. (2.3). In doing this, one obtains

$$\mathbf{B}(\mathbf{r}, t) = \frac{\lambda}{\mathrm{i}c}\mathbf{E}(\mathbf{r}, t). \tag{3.38}$$

Finally, Eq. (3.38) can be substituted into Eq. (3.17) to obtain the Lorentz-boosted helical electric field given by

$$\mathbf{E}'(\mathbf{r}',t') = \gamma\left[\mathbf{E}(\mathbf{r},t) + \frac{\lambda v}{\mathrm{i}c}\hat{\mathbf{z}}\times\mathbf{E}(\mathbf{r},t)\right] + (1-\gamma)\left[\hat{\mathbf{z}}\cdot\mathbf{E}(\mathbf{r},t)\right]\hat{\mathbf{z}}, \tag{3.39}$$

where the following expression for the corresponding magnetic field $\mathbf{B}'(\mathbf{r}',t')$ is obtained via Eq. (3.38) using frame F' coordinates:

$$\mathbf{B}'(\mathbf{r}',t') = \frac{\lambda}{\mathrm{i}c}\mathbf{E}'(\mathbf{r}',t'). \tag{3.40}$$

It should again be emphasized that the relation between the electric and magnetic fields in frame F are the same as that between those in frame F'. This is because a plane wave in frame F remains a plane wave when boosted to F'. Due to its abovementioned invariance, the same helicity λ appears in the expressions for the electromagnetic fields in both frames F and F'. Helicity invariance under Lorentz boosts will now be shown explicitly.

3.2 The invariance of helicity under Lorentz boosts

Given that the Lorentz invariance of helicity underpins the work in this thesis, it makes sense to explicitly demonstrate it. Assume that the helicity λ' of the boosted field is not necessarily equal to the unboosted helicity λ'. In this case, Eq. (3.40) relating the boosted electric field $\mathbf{E}'(\mathbf{r}',t')$ to the boosted magnetic field $\mathbf{B}'(\mathbf{r}',t')$ would be written as

$$\mathbf{B}'(\mathbf{r}',t') = \frac{\lambda'}{\mathrm{i}c}\mathbf{E}'(\mathbf{r}',t'). \tag{3.41}$$

By substituting Eq. (3.39) for $\mathbf{E}'(\mathbf{r}',t')$ into the previous equation, one has

$$\begin{aligned}\mathbf{B}'(\mathbf{r}',t') &= \frac{\lambda'}{\mathrm{i}c}\left\{\gamma\left[\mathbf{E}(\mathbf{r},t) + \frac{\lambda v}{\mathrm{i}c}\hat{\mathbf{v}}\times\mathbf{E}(\mathbf{r},t)\right] + (1-\gamma)\left[\hat{\mathbf{v}}\cdot\mathbf{E}(\mathbf{r},t)\right]\hat{\mathbf{v}}\right\}\\ &= \gamma\frac{\lambda'}{\mathrm{i}c}\mathbf{E}(\mathbf{r},t) - \lambda'\lambda\frac{v\hat{\mathbf{v}}\times\mathbf{E}(\mathbf{r},t)}{c^2} + (1-\gamma)\left[\hat{\mathbf{v}}\cdot\frac{\lambda'}{\mathrm{i}c}\mathbf{E}(\mathbf{r},t)\right]\hat{\mathbf{v}},\end{aligned} \tag{3.42}$$

where $\hat{\mathbf{v}}$ is the direction of motion of the scattering object.

Immediately, one sees that Eq. (3.42) can only hold if $\lambda = \lambda'$ as this is the only way to reproduce the well-known and general formula for the boosted magnetic field $\mathbf{B}'(\mathbf{r}',t')$ given in Eq. (3.18).

3.3 Summary

In this chapter, special relativity was introduced by beginning with the concept of reference frames, where an inertial reference frame F' moves relative to a laboratory frame F along the z–axis. The Doppler shift was then defined, which explains how the wavelength of an incident electromagnetic field is measured differently depending on the frame in which it is observed. If an object moves away from an incident electromagnetic field, a longer wavelength is perceived. Conversely, an observer moving towards an incident field observes

a smaller wavelength. Afterwards, the coordinates in frame F were related to those in frame F' and were used to derive the formula for length contraction. Length contraction was then used as a justification as to why Mie theory calculations should be carried out in the inertial frame F' and not F. This is because an observer in frame F measures a length contracted radius of the spherical scatterer along the z–axis, effectively making it an ellipsoid. Mie theory is therefore invalid in frame F as it only applies to spheres. Next, the Lorentz boost of electromagnetic fields was discussed, along with visual examples of the resulting effects on the fields of a positive point charge and plane wave. It was also seen that the energy density of a plane-wave electromagnetic field scales with a factor represented by the Doppler shift. Afterwards, the electric and magnetic fields were expressed in the helicity basis. Finally, the invariance of helicity under Lorentz boosts was explicitly demonstrated, which will be required in the following chapter.

4 | Minimising the Backscattering by a Relativistically Moving Sphere

This chapter is based on the work in Ref. [P1] carried out with Aristeidis Lamprianidis and Yannick Augenstein, where the backscattered signal from a relativistically moving sphere was investigated. The consideration of a single sphere is an important prerequisite to studying more complex systems like lattices and molecules as done in the following chapters.

The specific quantity investigated is known as the directivity. The directivity is the ratio of the scattered energy density in a particular direction and the average scattered energy per unit solid angle [115]. In this chapter, only the backscattered direction will be considered. Due to the finite nature of the sphere, an incident field in the form of a Gaussian beam will be considered. The interaction is achieved by the sphere moving in through one side of the beam and out of the other, leading to a finite backscattered energy density from which the directivity is well-defined. From the formulas derived in [31], the FHM outlined in the previous section can easily be applied, allowing one to implement Mie theory to determine the scattered energy density.

A further analysis of the backscattered directivity comes in the form of its minimisation. The minimisation of backscattering is linked to what is known as the first Kerker condition and has many practical uses. For example, minimising the backscattered signal by an antenna ensures that as much information as possible is transmitted and not reflected away [116]. The first Kerker condition is also observed in nature, where plants exploit it to absorb as much sunlight as possible [93]. To theoretically investigate the first Kerker condition, a quantity known as the directivity will be considered. The directivity serves as a comprehensible figure of merit that relates the backscattered energy to the average scattered energy by the sphere. Specifically, one is able to see if most of the energy is concentrated in or away from the direction of backscattering.

In Section 4.1, the nature of the incident Gaussian beam will be explained along with how to best represent it to apply the FHM. The chosen method is the angular spectrum representation, which expresses the beam as a sum of its constituent plane waves. In doing this, one is able to apply the formulas for Lorentz-boosting plane waves derived in the previous chapter. Subsequently in Section 4.2, the scattering scenario will be outlined and all necessary reference frames will be defined. In Section 4.3 the first step of the FHM will then be carried out, where the incident field is boosted from the lab frame F to the sphere's frame F'. It is in frame F where the directivity is observed. Section 4.4 concerns itself with the second step of the FHM, where the scattered energy density is obtained in frame F'. Here, one applies the T–matrix formalism from Mie theory to obtain the scattered field and, consequently, the scattered energy density. Afterwards, the final step of the FHM is implemented in Section 4.5, and the backscattered energy density is Lorentz-boosted from frame F' to frame F. The final expression for the backscattered directivity is also given, and the backscattering is explored by varying a wide range of parameters. An example of such parameters are Mie angles, which parametrise Mie coefficients in an abstract way such that one can in-

vestigate the directivity of any possible spherical scatterer. Finally, the directivity will be minimised in Section 4.6, where a relativistic Kerker condition is devised. Specifically, the minimisation is carried out with respect to the Mie angles describing the sphere.

Note: in Ref. [P1], a different convention for the spherical harmonics was implemented. Specifically, a modified normalisation factor $\tilde{\Omega}_{\ell m}$ was used, which will be used in this chapter and is related to $\Omega_{\ell m}$ defined in Eq. (2.30) *as*

$$\tilde{\Omega}_{\ell m} = \mathrm{i}^m \Omega_{\ell m}. \tag{4.1}$$

The original normalisation $\Omega_{\ell m}$ will be used in subsequent chapters.

4.1 Angular spectrum representation of a monochromatic Gaussian beam

To describe the incident field in this chapter, the angular spectrum representation (ASR) will the implemented. The ASR is a technique that allows one to conveniently describe electromagnetic fields in homogeneous, isotropic, linear and sourceless media. In this chapter, the homogeneous medium is a vacuum. By employing the ASR, processes such as the focusing of light and propagation of laser beams is elegantly described [117].

The ASR hinges on expanding electromagnetic fields in terms of their constituent plane wave contributions. Each plane wave exhibits different polarisations and directions of propagation $\mathbf{k} = (k_x, k_y, k_z)$. As mentioned above, an incident monochromatic Gaussian beam will be considered in this chapter. Considering the spatial part $\mathbf{E}(\mathbf{r})$ of the beam's electric field $\mathbf{E}(\mathbf{r}, t)$ spanning the x–y–plane and propagating along the z-axis, one can expand an arbitrary field in the x–y–plane at a given coordinate z into a superposition of plane waves as [117, Eq. (2.119)]

$$\mathbf{E}(x, y, z) = \int_{-\infty}^{\infty} \mathrm{d}k_x \int_{-\infty}^{\infty} \mathrm{d}k_y \, \widetilde{\mathbf{E}}(k_x, k_y; z) \mathrm{e}^{\mathrm{i}(k_x x + k_y y)}, \tag{4.2}$$

where k_x and k_y are respectively the x and y wave vector components of each constituent plane wave, and $\widetilde{\mathbf{E}}(k_x, k_y; z)$ is the two dimensional Fourier transform of $\mathbf{E}(x, y, z)$ given by

$$\widetilde{\mathbf{E}}(k_x, k_y; z) = \frac{1}{4\pi^2} \int_{-\infty}^{\infty} \mathrm{d}x \int_{-\infty}^{\infty} \mathrm{d}y \, \mathbf{E}(x, y, z) \mathrm{e}^{-\mathrm{i}(k_x x + k_y y)}. \tag{4.3}$$

When substituted into Eq. (4.2), one obtains the ASR [117, Eq. (2.124)]

$$\mathbf{E}(\mathbf{r}) = \int_{-\infty}^{\infty} \mathrm{d}k_x \int_{-\infty}^{\infty} \mathrm{d}k_y \, \widetilde{\mathbf{E}}(k_x, k_y; 0) \mathrm{e}^{\mathrm{i}\mathbf{k}\cdot\mathbf{r}}. \tag{4.4}$$

Note that the presence of the $\mathrm{e}^{\mathrm{i}\mathbf{k}\cdot\mathbf{r}}$ in the previous equation implies that the beam propagates into the $z > 0$ half-plane. If the propagation occurred in the $-z$–direction, the $\mathrm{e}^{\mathrm{i}\mathbf{k}\cdot\mathbf{r}}$ term would become $\mathrm{e}^{\mathrm{i}(k_x x + k_y y - k_z z)}$.

For the specific case of a monochromatic Gaussian beam, $\widetilde{\mathbf{E}}(k_x, k_y; 0)$ is given by [117, Eq. (3.9)]

$$\widetilde{\mathbf{E}}(k_x, k_y; 0) = \mathbf{E}_0(\hat{\mathbf{k}}) \frac{w_o^2}{4\pi} \mathrm{e}^{-\frac{w_0^2}{4}(k_x^2 + k_y^2)}, \tag{4.5}$$

where $\mathbf{E}_0(\hat{\mathbf{k}})$ is a vector that contains information about the polarisation of the beam and its amplitude. Moreover, w_0 is the beam waist, which represents the size of the beam at its focus point $z = 0$. From w_0, one can obtain the beam radius $w(z)$, which is the radius at which the intensity of the beam falls to $1/\mathrm{e}^2$ of its axial value at z. In this chapter, the paraxial approximation will be implemented. The paraxial approximation is used to describe a beam with a large waist and narrow angular spectrum about the optical axis (in this section, the z–axis) [117, 118]. Correspondingly, the explicit expression for $w(z)$ obtained using the paraxial approximation is given by [117, Eq. (3.14)]

$$w(z) = w_0\sqrt{\left(1 + \frac{z^2}{z_0^2}\right)}, \tag{4.6}$$

where

$$z_0 = \frac{kw_0^2}{2} \tag{4.7}$$

is the Rayleigh length and $k = |\mathbf{k}|$. For a monochromatic Gaussian beam, each constituent plane wave has the same wavenumber k but different k_x, k_y and k_z components. Moreover, one sees from Eq. (4.6) that the beam waist is given by $w_0 = w(z = 0)$. A pictorial representation of the beam radius and waist is given in Fig. 4.1.

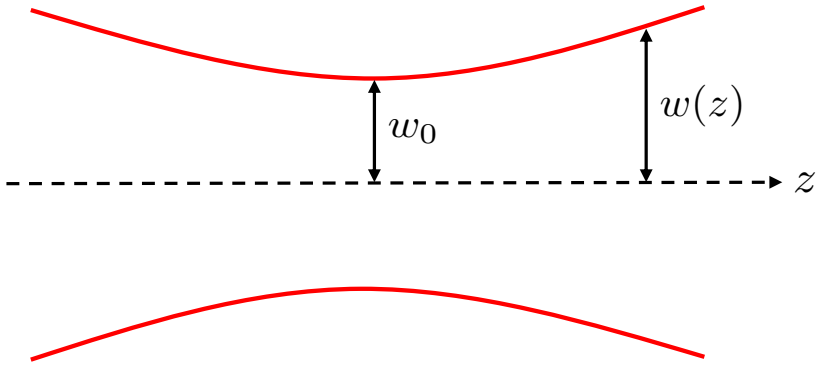

Figure 4.1: The outline of a Gaussian beam (red) with beam radius $w(z)$ and waist w_0 propagating along the z-axis.

In this chapter, Eq. (4.4) will be expressed in terms of the polar and azimuthal angles $\theta_{\mathbf{k}}$ and $\phi_{\mathbf{k}}$, respectively, which relate to the wavevector $\mathbf{k}$ of each constituent plane wave. This is achieved upon substitution of the relations

$$k_x = k\sin(\theta_{\mathbf{k}})\cos(\phi_{\mathbf{k}}), \tag{4.8}$$
$$k_y = k\sin(\theta_{\mathbf{k}})\sin(\phi_{\mathbf{k}}), \tag{4.9}$$

and the Jacobian transformation

$$\begin{aligned}\mathrm{d}k_x\mathrm{d}k_y &= \begin{vmatrix} \frac{\partial k_x}{\partial \theta_{\mathbf{k}}} & \frac{\partial k_y}{\partial \theta_{\mathbf{k}}} \\ \frac{\partial k_x}{\partial \phi_{\mathbf{k}}} & \frac{\partial k_y}{\partial \phi_{\mathbf{k}}} \end{vmatrix} \\ &= \frac{k}{2}\sin(2\theta_{\mathbf{k}})\mathrm{d}\theta_{\mathbf{k}}\mathrm{d}\phi_{\mathbf{k}}\end{aligned} \tag{4.10}$$

into Eq. (4.4). Finally, one obtains the expression for the electric field $\mathbf{E}(\mathbf{r})$ of a Gaussian beam given by

$$\mathbf{E}(\mathbf{r}) = \frac{k}{2}\int_0^{\pi} \mathrm{d}\theta_{\mathbf{k}}\, \sin(2\theta_{\mathbf{k}}) \int_0^{2\pi} \mathrm{d}\phi_{\mathbf{k}}\, \mathbf{E}_0 \frac{w_o^2}{4\pi} \exp\left(\mathrm{i}\lambda\phi_{\mathbf{k}} - \frac{w_0^2\omega^2}{4c^2}\sin^2(\theta_{\mathbf{k}})\right) \cdot H\left(\frac{\pi}{2} - \theta_{\mathbf{k}}\right) \exp(\mathrm{i}\mathbf{k}\cdot\mathbf{r}), \tag{4.11}$$

where the Heaviside function $H(\frac{\pi}{2} - \theta_{\mathbf{k}})$ ensures the exclusion of plane wave components moving away from the illuminated object. Note the $\exp(\mathrm{i}\lambda\phi_{\mathbf{k}})$ that appears in the previous equation to ensure that the angular momentum in the z–direction m_z has a value $m_z = \lambda$, where λ is the beam's helicity. This is required for a circularly polarised beam with a large beam waist w_0, as considered in this chapter. An explanation for the large waist will be given in the following section.

In this chapter, Dirac notation will be implemented such that $\mathbf{E}_0$ in Eq. (4.11) is represented by the following ket:

$$\mathbf{E}_0 \equiv E_0 \left|\lambda\, \hat{\mathbf{k}}\, \omega\right\rangle, \tag{4.12}$$

where

$$\left|\lambda\, \hat{\mathbf{k}}\, \omega\right\rangle \equiv \hat{\mathbf{e}}_\lambda(\hat{\mathbf{k}}) \exp\Big[\mathrm{i}\omega(\hat{\mathbf{k}}\cdot\mathbf{r}/c)\Big], \tag{4.13}$$

E_0 is the field amplitude, and $\hat{\mathbf{e}}_\lambda(\hat{\mathbf{k}})$ is defined in Eq. (2.39).

Succinctly, the total electric field of the beam $|\mathbf{E}\rangle$ given in Eq. (4.11) can be written in Dirac notation as

$$|\mathbf{E}\rangle = \sum_{\lambda=\pm1} \int_0^{2\pi} \mathrm{d}\phi_{\mathbf{k}} \int_0^{\pi} \mathrm{d}\theta_{\mathbf{k}} \int_0^{\infty} \mathrm{d}\omega\, \mathcal{G}_\lambda(\omega, \theta_{\mathbf{k}}, \phi_{\mathbf{k}}) \left|\lambda\, \hat{\mathbf{k}}\, \omega\right\rangle + \mathrm{c.c.}, \tag{4.14}$$

where

$$\mathcal{G}_\lambda(\omega, \theta_{\mathbf{k}}, \phi_{\mathbf{k}}) = E_0 \sin(2\theta_{\mathbf{k}}) \exp\left(\mathrm{i}\lambda\phi_{\mathbf{k}} - \frac{w_0^2\omega^2}{4c^2}\sin^2(\theta_{\mathbf{k}})\right)\delta(\omega - \omega_0) \tag{4.15}$$

and 'c.c.' denotes the complex conjugate of $|\mathbf{E}\rangle$. Note the appearance of the $\delta(\omega - \omega_0)$ term in Eq. (4.15), where ω_0 denotes the frequency of a non-transformed beam. In the next section, rotations and Lorentz-boosts of the beam will be considered, and the $\delta(\omega - \omega_0)$ term ensures the correct transformed frequency ω is considered.

In this section, the angular spectrum representation of a monochromatic Gaussian beam was discussed. Such a beam will be used as the incident field in this chapter. In the following section, the complete scattering scenario will be outlined.

4.2 Outlining the setup and scattering scenario

After having discussed the nature of the incident field, one can now build a picture of the scattering scenario. The considered scatterer is a lossless, dielectric sphere that moves with velocity $\mathbf{v} = v\hat{\mathbf{z}}$ through an incident electric field $\mathbf{E}_{\mathrm{i}}(\mathbf{r}, t)$ represented by a Gaussian beam

described by Eq. (4.14) (c.f. Fig. 4.2). In this chapter, a beam with helicity $\lambda_i = +1$ and waist $w_0 = 10L$ is considered, where L is the stationary wavelength of the beam. For such a large waist, the beam is approximately a plane wave but is finite in space. As a result, one can determine the total energy of the scattered field instead of an energy density, allowing one to determine the directivity later on. Another reason for considering a spatially-finite beam is that the interaction between the beam and the sphere would also be finite, where the sphere enters through one side of the beam and exits the other (c.f. Fig. 4.2 (b)). This would not be case for an infinitely extended plane wave, where the interaction would be incessant and the radiated field intensity would only vary azimuthally. In short, a localised interaction leads to the scattering of spherical waves, allowing one to consider the spherical basis in the upcoming scattering calculations.

Since the Gaussian beam can be represented as a sum of helical plane waves, only the electric field will be referenced in this chapter. The reason for this is that the boosted electromagnetic field can be fully expressed in terms of the electric field in line with Eqs (3.39) and (3.40). As a result, explicit reference to the magnetic field is not necessary.

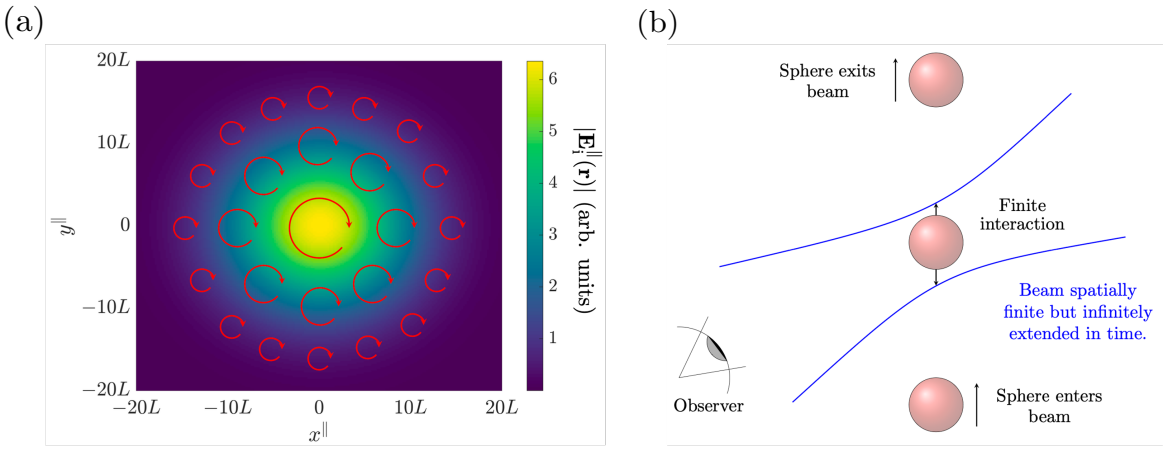

Figure 4.2: In (a), the magnitude of the incident Gaussian beam is depicted in the beam's $x^{\parallel}$–$y^{\parallel}$ plane. The beam has a large waist $w_0 = 10L$, where L is the incident wavelength of the beam. The red arrows depict the circular polarisation of the beam. In (b), the interaction process between the sphere and the incident beam is shown. Adapted from [P1]. Copyright © 2023 American Physical Society.

The Gaussian beam is oriented at an angle Θ_i to the sphere's direction of motion as seen in the lab frame F. Physically speaking, Θ_i is the angle between the beam's propagation direction and velocity of the sphere. Since the beam orientation can change, one requires an additional reference frame $F^{\parallel}$. In $F^{\parallel}$, the corresponding $z^{\parallel}$ axis aligns with the direction of propagation of the beam $\hat{\mathbf{k}}_i$. Consequently, an observer in frame F observes a beam rotated with angle Θ_i with respect to its own z–axis.

Of course, a boosted inertial reference frame F' in which the sphere is stationary is also required. As mentioned in Chapter 3, all scattering calculations need to be carried out in F' since Mie theory is only valid in this frame. Recall the invalidity of Mie theory in frame F. Here, an observer would measure a sphere undergoing length contraction along the z–axis,

essentially making it an ellipsoid (c.f. Fig. 3.3). As Mie theory only applies to spheres, one can therefore only apply it in F' to obtain the scattered field.

A depiction of each reference frame is given in Fig. 4.3. Note that terms with a prime pertain to frame F', while those without a prime relate to frame F. Terms with a '$\parallel$' superscript denote quantities in frame $F^{\parallel}$. Note also that the propagation direction $\hat{\mathbf{k}}_\mathrm{i}$ of the incident field in F is not the same as that in F' denoted by $\hat{\mathbf{k}}'_\mathrm{i}$. This is because there exist components of $\hat{\mathbf{k}}_\mathrm{i}$ in the x–y–plane that affect its component in the z–direction. Explicitly, one finds from Eq. (3.4) for a general direction of propagation $\mathbf{k} = (k_x, k_y, k_z)^\mathrm{T}$ in F that

$$\begin{aligned}\begin{pmatrix} k' \\ k'_x \\ k'_y \\ k'_z \end{pmatrix} &= \begin{pmatrix} \gamma & 0 & 0 & -\gamma\beta \\ 0 & 1 & 0 & 0 \\ 0 & 0 & 1 & 0 \\ -\gamma\beta & 0 & 0 & \gamma \end{pmatrix} \begin{pmatrix} k \\ k_x \\ k_y \\ k_z \end{pmatrix} \\ &= \begin{pmatrix} \gamma(k - \beta k_z) \\ k_x \\ k_y \\ \gamma(k_z - \beta k) \end{pmatrix}. \end{aligned} \tag{4.16}$$

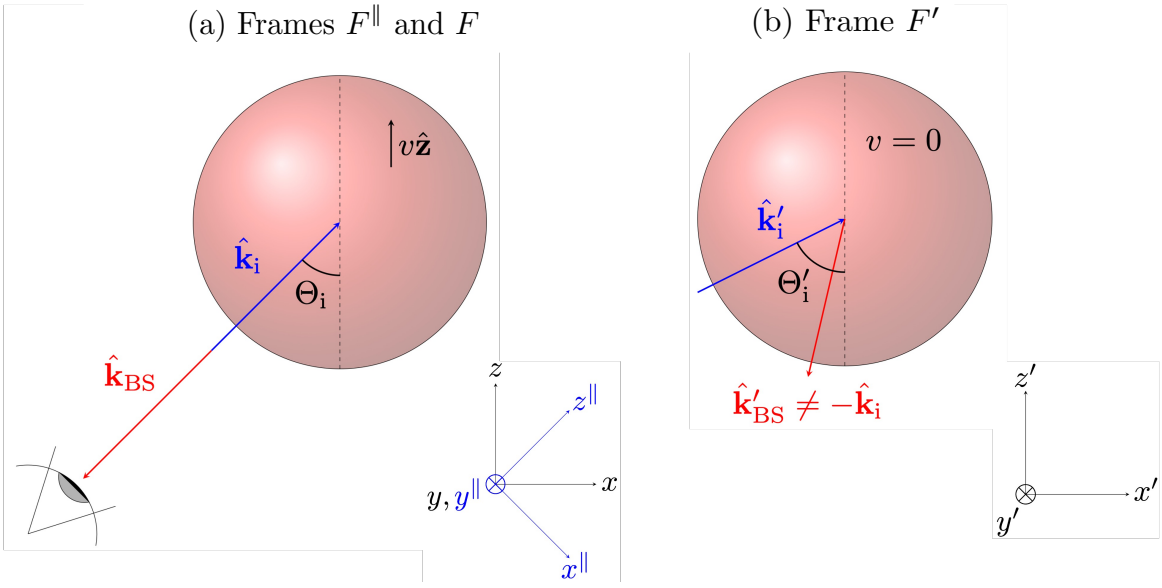

Figure 4.3: Illustration of the sphere in a) the beam's frame $F^{\parallel}$ and the rotated frame F, which includes an external observer (indicated by the eye), and b) the sphere's own inertial frame F'. In frame F, the sphere appears to move with velocity $v\hat{\mathbf{z}}$. The wave vector $\hat{\mathbf{k}}_\mathrm{i}$ is incident on the sphere at an angle Θ_i. In a), the backscattering direction $\hat{\mathbf{k}}_\mathrm{BS}$ (marked by the red arrow) is directly opposite to $\hat{\mathbf{k}}_\mathrm{i}$, and this direction will be used to establish a relativistic Kerker condition. In b), the sphere is at rest ($v = 0$) in F', and the incident field's Lorentz-transformed wave vector is $\hat{\mathbf{k}}'_\mathrm{i}$, incident with angle $\Theta'_\mathrm{i} \neq \Theta_\mathrm{i}$ when $\Theta_\mathrm{i} \notin \{0, \pi\}$ and $\Theta'_\mathrm{i} = \Theta_\mathrm{i}$ when $\Theta_\mathrm{i} \in \{0, \pi\}$. In F', the backscattering direction $\hat{\mathbf{k}}'_\mathrm{BS}$ is generally not opposite to $\hat{\mathbf{k}}_\mathrm{i}$ or $\hat{\mathbf{k}}'_\mathrm{i}$. Adapted from [P1]. Copyright © 2023 American Physical Society.

Upon determining the scattered electric field and the resulting directivity in F', the result must then be inverse Lorentz-boosted to frame F. In other words, the FHM outlined in Chapter 3 is applied.

Worth noting is that the azimuthal incidence angle of the beam Φ_i is set to $\Phi_\mathrm{i} = 0$. However, one could assign Φ_i an arbitrary value. The reason for such freedom is due to the spherical symmetry of the system. As the Lorentz boost occurs along the z–axis, the scattering pattern will therefore be invariant with respect to the orientation of the incident field in the x–y–plane.

In this section, the scattering setup was discussed and all necessary reference frames were defined. In the following section, the first step of the FHM will be implemented, where the incident field is boosted to frame F'.

4.3 Lorentz boosting the incident field into the scatterer's reference frame

In this section, the first step of the FHM will be carried out. Firstly, however, the incident beam needs to be rotated in frame F by the angle of incidence Θ_i. Such a rotation is applied to quantities in the beam's reference frame $F^\parallel$, where the electric field is given by Eq. (4.14) in $F^\parallel$ coordinates:

$$\left|\mathbf{E}_\mathrm{i}{}^\parallel\right\rangle = \sum_{\lambda=\pm1} \int_0^{2\pi} \mathrm{d}\phi_\mathbf{k}^\parallel \int_0^{\pi} \mathrm{d}\theta_\mathbf{k}^\parallel \int_0^{\infty} \mathrm{d}\omega^\parallel \, \mathcal{G}_\lambda(\omega^\parallel, \theta_\mathbf{k}^\parallel, \phi_\mathbf{k}^\parallel) \left|\lambda\, \hat{\mathbf{k}}^\parallel\, \omega^\parallel\right\rangle + \mathrm{c.c.}. \tag{4.17}$$

In Eq. (4.17), the subscript 'i' refers to the incident field

To obtain the rotated field in F, the following rotation operation is applied:

$$|\mathbf{E}_\mathrm{i}\rangle = \hat{\mathbf{R}}_y(\Theta_\mathrm{i}) \left|\mathbf{E}_\mathrm{i}^\parallel\right\rangle, \tag{4.18}$$

where

$$\hat{\mathbf{R}}_y(\Theta_\mathrm{i}) \left|\lambda^\parallel\, \hat{\mathbf{k}}^\parallel\, \omega^\parallel\right\rangle = \sum_\lambda \int_0^{2\pi} \mathrm{d}\phi_\mathbf{k} \int_0^{\pi} \mathrm{d}\theta_\mathbf{k} \int_0^{\infty} \mathrm{d}\omega \, \mathcal{R}_{\lambda^\parallel,\lambda}(\omega^\parallel, \theta_\mathbf{k}^\parallel, \phi_\mathbf{k}^\parallel, \omega, \theta_\mathbf{k}, \phi_\mathbf{k}; \Theta_\mathrm{i}) \left|\lambda\, \hat{\mathbf{k}}\, \omega\right\rangle \tag{4.19}$$

with transformation coefficients

$$\begin{aligned}\mathcal{R}_{\lambda^\parallel,\lambda}(\omega^\parallel, \theta_\mathbf{k}^\parallel, \phi_\mathbf{k}^\parallel, \omega, \theta_\mathbf{k}, \phi_\mathbf{k}; \Theta_\mathrm{i}) &= \mathcal{P}(\theta_\mathbf{k}^\parallel, \phi_\mathbf{k}^\parallel, \Theta_\mathrm{i}) \delta(\omega - \omega^\parallel) \\ &\quad \cdot \delta\left[\theta_\mathbf{k}^\parallel - \arccos(\hat{k}_z)\right] \delta\left[\phi_\mathbf{k}^\parallel - \mathrm{atan2}(\hat{k}_y, \hat{k}_x)\right].\end{aligned} \tag{4.20}$$

In Eq. (4.20), the Cartesian components $(\hat{k}_x, \hat{k}_y, \hat{k}_z)$ of the unit vector $\hat{\mathbf{k}}$ in F are related to those in $F^\parallel$ via a three-dimensional rotation matrix, where

$$\begin{aligned}\begin{pmatrix}\hat{k}_x \\ \hat{k}_y \\ \hat{k}_z\end{pmatrix} &= \begin{pmatrix}\cos\Theta_\mathrm{i} & 0 & \sin\Theta_\mathrm{i} \\ 0 & 1 & 0 \\ -\sin\Theta_\mathrm{i} & 0 & \cos\Theta_\mathrm{i}\end{pmatrix} \begin{pmatrix}\hat{k}_x^\parallel \\ \hat{k}_y^\parallel \\ \hat{k}_z^\parallel\end{pmatrix} \\ &= \begin{pmatrix}\sin\theta_\mathbf{k}^\parallel \cos\phi_\mathbf{k}^\parallel \cos\Theta_\mathrm{i} + \cos\theta_\mathbf{k}^\parallel \sin\Theta_\mathrm{i} \\ \sin\theta_\mathbf{k}^\parallel \sin\phi_\mathbf{k}^\parallel \\ -\sin\theta_\mathbf{k}^\parallel \cos\phi_\mathbf{k}^\parallel \sin\Theta_\mathrm{i} + \cos\theta_\mathbf{k}^\parallel \cos\Theta_\mathrm{i}\end{pmatrix}.\end{aligned} \tag{4.21}$$

In Eq. (4.20) is the phase term $\mathcal{P}(\theta_{\mathbf{k}}^{\parallel}, \phi_{\mathbf{k}}^{\parallel}, \Theta_{\mathrm{i}})$ that appears when rotating helical plane waves is included. This phase term is discussed in Ref. [113] and is given by

$$\mathcal{P}(\theta_{\mathbf{k}}^{\parallel}, \phi_{\mathbf{k}}^{\parallel}, \Theta_{\mathrm{i}}) = \exp\Big[\mathrm{i}p(\theta_{\mathbf{k}}^{\parallel}, \phi_{\mathbf{k}}^{\parallel}, \Theta_{\mathrm{i}})\Big], \tag{4.22}$$

with

$$p(\theta_{\mathbf{k}}^{\parallel}, \phi_{\mathbf{k}}^{\parallel}, \Theta_{\mathrm{i}}) = \mathrm{atan2}\Big[-\lambda \sin(\Theta_{\mathrm{i}}) \sin\Big(\phi_{\mathbf{k}}^{\parallel}\Big), \cos\Big(\theta_{\mathbf{k}}^{\parallel}\Big) \sin(\Theta_{\mathrm{i}}) \cos\Big(\phi_{\mathbf{k}}^{\parallel}\Big) + \sin\Big(\theta_{\mathbf{k}}^{\parallel}\Big) \cos(\Theta_{\mathrm{i}})\Big]. \tag{4.23}$$

The function $\mathrm{atan2}(x, y)$ in Eq. (4.23) refers to the two-argument inverse tangent function that ensures the output lies in the correct Cartesian quadrant.

With the rotated field $|\mathbf{E}_{\mathrm{i}}\rangle$ in F at hand, one can now implement step 1 of the FHM. To do this, another operator is required to boost the incident electric field from F to F'. Since Dirac notation is used, the boosting operator must be expressed using a compatible representation. However, the operation is the same as that described by Eq. (3.1), so the symbol $\hat{\mathbf{L}}_z(\beta)$ will be retained. For this chapter, $\hat{\mathbf{L}}_z(\beta)$ is written as

$$\hat{\mathbf{L}}_z(\beta) \left|\lambda\, \hat{\mathbf{k}}\, \omega\right\rangle = \sum_{\lambda'} \int_0^{2\pi} \mathrm{d}\phi'_{\mathbf{k}} \int_0^{\pi} \mathrm{d}\theta'_{\mathbf{k}} \int_0^{\infty} \mathrm{d}\omega' \mathcal{L}_{\lambda\lambda'}(\omega, \theta_{\mathbf{k}}, \phi_{\mathbf{k}}, \omega', \theta'_{\mathbf{k}}, \phi'_{\mathbf{k}}; \beta) \left|\lambda'\, \hat{\mathbf{k}}'\, \omega'\right\rangle, \tag{4.24}$$

where

$$\begin{aligned} \mathcal{L}_{\lambda\lambda'}(\omega, \theta_{\mathbf{k}}, \phi_{\mathbf{k}}, \omega', \theta'_{\mathbf{k}}, \phi'_{\mathbf{k}}; \beta) = \Delta(\beta, \theta_{\mathbf{k}}) \cdot \delta_{\lambda'\lambda} \cdot \delta\left[\omega' - \Delta\left(\beta, \theta_{\mathbf{k}}\right) \omega\right] \\ \cdot \delta\left[\theta'_{\mathbf{k}} - \arccos\left(\frac{\cos\theta_{\mathbf{k}} - \beta}{1 - \beta\cos\theta_{\mathbf{k}}}\right)\right] \\ \cdot \delta\left(\phi'_{\mathbf{k}} - \phi_{\mathbf{k}}\right), \end{aligned} \tag{4.25}$$

and $\Delta(\beta, \theta_{\mathbf{k}})$ is the angle-dependent Doppler factor defined in Eq. (3.6). Note that the arguments in each δ–distribution are drawn from Eq. (3.4) representing the Lorentz boost of the four-wavevector $\mathbf{K}(\omega, \mathbf{k})$. Explicitly, the boosted polar angle $\theta'_{\mathbf{k}}$ and azimuthal angle $\phi'_{\mathbf{k}}$ are obtained via

$$\begin{aligned} \theta'_{\mathbf{k}} &= \arccos\left(\frac{k'_z}{k'}\right) \\ &= \arccos\left(\frac{k_z - \beta k}{k - \beta k_z}\right) \\ &= \arccos\left(\frac{\cos\theta_{\mathbf{k}} - \beta}{1 - \beta\cos\theta_{\mathbf{k}}}\right) \end{aligned} \tag{4.26}$$

and

$$\begin{aligned} \phi'_{\mathbf{k}} &= \arctan\left(\frac{k'_y}{k'_x}\right) \\ &= \arctan\left(\frac{k_y}{k_x}\right) \\ &= \phi_{\mathbf{k}}. \end{aligned} \tag{4.27}$$

The Lorentz invariance of the azimuthal angle $\phi_{\mathbf{k}}$ comes at no surprise. As mentioned in Chapter 3, k_x and k_y are invariant under boosts in the z–direction, so the same must apply to $\phi_{\mathbf{k}}$. Also included in Eq. (4.25) is the boosted frequency ω', which is likewise obtained from Eq. (3.4) and is given by

$$\omega' = \Delta(\beta, \theta_{\mathbf{k}})\omega. \tag{4.28}$$

To help conceptualise the boosted angle $\theta'_{\mathbf{k}}$ and normalised frequency ω', colour plots of their dependence on $\theta_{\mathbf{k}}$ are given in Figs 4.4 (a) and (b), respectively. The boosted frequency ω' is normalised with respect to $\gamma\omega$ to avoid saturation of the data as $\beta \to 1$ and $\theta_{\mathbf{k}} \to \pi$. Note that it is only necessary to consider $\beta > 0$, since the $\beta < 0$ values are accounted for by the $\pi/2 < \theta_{\mathbf{k}} \leq \pi$ values. In this range for $\theta_{\mathbf{k}}$, the wave propagates into the $-z$ half-plane when $\beta > 0$. This would be equivalent to considering the ranges $0 \leq \theta_{\mathbf{k}} < \pi/2$ and $\beta < 0$. Figure 4.4 offers an extension to Chapter 3 since an arbitrary wave propagation direction is now considered instead of just along the z–axis.

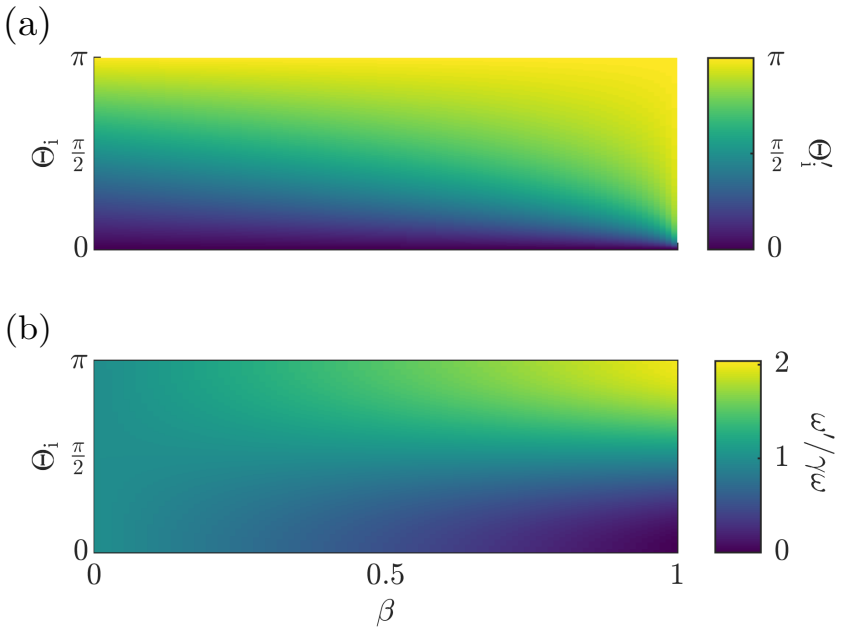

Figure 4.4: In (a), the incident field angle Θ'_{i} as viewed in frame F' is plotted as a function of the sphere's speed β and incident field angle Θ_{i} in frame F. The analogous plot is given in (b) for the normalised boosted frequency of the incident field $\omega'/\gamma\omega$ for a fixed ω. This normalisation ensures that the data as $\beta \to 1$ and $\Theta_{\mathrm{i}} \to \pi$ doesn't overpower that for lower speeds and incident field angles. Adapted from [P1]. Copyright © 2023 American Physical Society.

Noteworthy features can be observed by considering the behaviour of $\theta'_{\mathbf{k}}$ and ω' at limiting values of β and $\theta_{\mathbf{k}}$. Beginning with $\theta'_{\mathbf{k}}$, one sees that it is invariant for $\theta_{\mathbf{k}} \in \{0, \pi\}$. The reason for this is that waves moving in the $\pm z$–direction simply experience a Doppler shift along the same axis without a change in propagation direction. For this specific case, the Doppler

shift can be seen by considering Eq. (3.5) for the Doppler–shifted wavelength L', where

$$\begin{aligned} k'_z &= \frac{2\pi}{L'} \\ &= k_z \Delta(\beta). \end{aligned} \tag{4.29}$$

Recall that $\Delta(\beta) = \Delta(\beta, 0)$.

Perhaps the most obvious quality of Fig. 4.4 (a), however, is that an increasing speed causes non-zero values of $\theta_{\mathbf{k}}$ to have boosted propagation directions $\theta'_{\mathbf{k}}$ that approach $\theta'_{\mathbf{k}} = \pi$ more rapidly. This is comprehensible upon consideration of the k'_z component of Eq. (4.16)

$$k'_z = \gamma(k_z - \beta k) \tag{4.30}$$

and the fact that k_x and k_y are Lorentz invariant. One sees in Eq. (4.30) that every k'_z value (except when $k = k_z$) becomes infinitely negative as $\beta \to 1$, which corresponds to $\theta_{\mathbf{k}} \to \pi$. Such a behaviour is depicted in Fig. 4.5 for the range $k_z \in [4.19\mu\mathrm{m}^{-1}, 6.28\mu\mathrm{m}^{-1}]$.

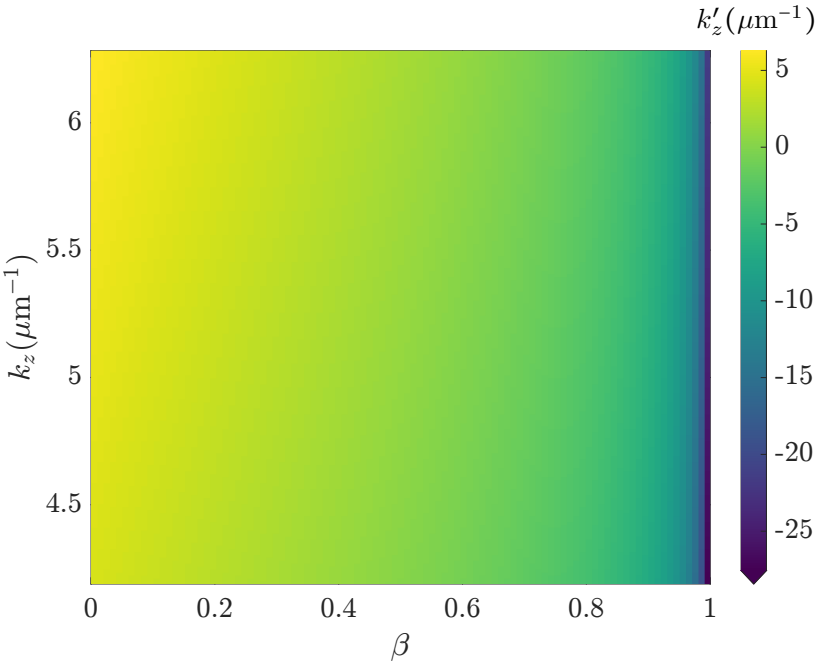

Figure 4.5: The boosted z-component k'_z of the wave vector $\mathbf{k}'$ in F' as a function of the sphere's speed β and the z-component k_z of the wave vector $\mathbf{k}$ in F. As $\beta \to 1$, all k'_z values (except when $k_z = k$) approach $k'_z = -\infty$.

Concerning the boosted frequency ω' shown in Fig. 4.4, the induced red- and blue-shifting is evident as $\beta \to 1$. When $\theta_{\mathbf{k}} = 0$, the object is moving directly away from the incident field, thus observing an ever-increasing red-shift as $\beta \to 1$ where the frequency perceived in F' virtually disappears. Conversely, an infinitely increasing frequency is observed in F' when $\theta_{\mathbf{k}} = \pi$ as this corresponds to the object moving directly towards the incident field source. In this case, a complete blue-shift occurs. Also notable is the case where $\theta_{\mathbf{k}} = \frac{\pi}{2}$, where $\omega' = \omega$. Here, the sphere moves perpendicularly to the direction of propagation of the incident field, where the incident field has no k_z component. As k_x and k_y are Lorentz invariant, k and therefore ω must also be invariant.

A final element of Eq. (4.25) to mention is the Kronecker delta $\delta_{\lambda\lambda'}$, which takes into account the helicity preservation under Lorentz boosts by ensuring non-zero values for the boosting coefficients only when $\lambda = \lambda'$.

At this point one can form a comprehensive description of the boosted incident field $|\mathbf{E}'_{\mathrm{i}}\rangle$ in F' for an arbitrary angle of incidence Θ_{i}. Combining the rotation and the boost, $|\mathbf{E}'_{\mathrm{i}}\rangle$ can now be related to the unrotated beam's electric field $\left|\mathbf{E}^{\parallel}_{\mathrm{i}}\right\rangle$ in $F^{\parallel}$ as follows:

$$\begin{aligned}\left|\mathbf{E}'_{\mathrm{i}}\right\rangle &= \hat{\mathbf{L}}_z(\beta)\hat{\mathbf{R}}_y(\Theta_{\mathrm{i}})\left|\mathbf{E}^{\parallel}_{\mathrm{i}}\right\rangle \\ &= \sum_{\lambda'}\int_0^{2\pi}\mathrm{d}\phi'_{\mathbf{k}}\int_0^{\pi}\mathrm{d}\theta'_{\mathbf{k}}\int_{0^+}^{\infty}\mathrm{d}\omega'\mathcal{G}'_{\lambda',\mathrm{i}}(\omega',\theta'_{\mathbf{k}},\phi'_{\mathbf{k}})\left|\lambda'\;\hat{\mathbf{k}}'\;\omega'\right\rangle + \mathrm{c.c.},\end{aligned} \tag{4.31}$$

where $\hat{\mathbf{k}}'$ is obtained using Eq. (3.4) and is given by

$$\hat{\mathbf{k}}' = \frac{\hat{\mathbf{k}} + [(\gamma-1)\cos\theta_{\mathbf{k}} - \gamma\beta]\,\hat{\mathbf{z}}}{\Delta(\beta,\theta_{\mathbf{k}})}. \tag{4.32}$$

Furthermore, the coefficient describing the Gaussian profile $\mathcal{G}'_{\lambda',\mathrm{i}}(\omega',\theta'_{\mathbf{k}},\phi'_{\mathbf{k}})$ in F' is given by

$$\mathcal{G}'_{\lambda',\mathrm{i}}(\omega',\theta'_{\mathbf{k}},\phi'_{\mathbf{k}}) = \mathcal{J}(\theta'_{\mathbf{k}},\phi'_{\mathbf{k}},\Theta_{\mathrm{i}})\mathcal{G}^{\parallel}_{\lambda',\mathrm{i}}\left\{\frac{\omega'}{\Delta\left[\beta,\theta^{\parallel}_{\mathbf{k}}(\theta'_{\mathbf{k}},\phi'_{\mathbf{k}})\right]},\theta^{\parallel}_{\mathbf{k}}(\theta'_{\mathbf{k}},\phi'_{\mathbf{k}}),\phi^{\parallel}_{\mathbf{k}}(\theta'_{\mathbf{k}},\phi'_{\mathbf{k}})\right\}, \tag{4.33}$$

where

$$\theta^{\parallel}_{\mathbf{k}}(\theta'_{\mathbf{k}},\phi'_{\mathbf{k}}) = \arccos\left\{\frac{1}{\Delta(-\beta,\theta'_{\mathbf{k}})}\left[\sin\theta'_{\mathbf{k}}\cos\phi'_{\mathbf{k}}\sin\Theta + \gamma(\cos\theta'_{\mathbf{k}}+\beta)\cos\Theta\right]\right\}, \tag{4.34}$$

and

$$\phi^{\parallel}_{\mathbf{k}}(\theta'_{\mathbf{k}},\phi'_{\mathbf{k}}) = \mathrm{atan2}[\sin\theta'_{\mathbf{k}}\sin\phi'_{\mathbf{k}}, \sin\theta'_{\mathbf{k}}\cos\phi'_{\mathbf{k}}\cos\Theta - \gamma(\cos\theta'_{\mathbf{k}}+\beta)\sin\Theta] \tag{4.35}$$

represent $\theta^{\parallel}_{\mathbf{k}}$ and $\phi^{\parallel}_{\mathbf{k}}$ as viewed from F'.

Finally, the Jacobian $\mathcal{J}(\theta'_{\mathbf{k}},\phi'_{\mathbf{k}},\Theta_{\mathrm{i}})$ in Eq. (4.33) converts the differential element $\mathrm{d}\theta^{\parallel}_{\mathbf{k}}\mathrm{d}\phi^{\parallel}_{\mathbf{k}}$ to that needed in F' given by $\mathrm{d}\theta'_{\mathbf{k}}\mathrm{d}\phi'_{\mathbf{k}}$, where

$$\begin{aligned}\mathcal{J}(\theta'_{\mathbf{k}},\phi'_{\mathbf{k}},\Theta_{\mathrm{i}}) &= \begin{vmatrix} \frac{\partial\theta^{\parallel}_{\mathbf{k}}}{\partial\theta'_{\mathbf{k}}} & \frac{\partial\theta^{\parallel}_{\mathbf{k}}}{\partial\phi'_{\mathbf{k}}} & \frac{\partial\theta^{\parallel}_{\mathbf{k}}}{\partial\omega'} \\ \frac{\partial\phi^{\parallel}_{\mathbf{k}}}{\partial\theta'_{\mathbf{k}}} & \frac{\partial\phi^{\parallel}_{\mathbf{k}}}{\partial\phi'_{\mathbf{k}}} & \frac{\partial\phi^{\parallel}_{\mathbf{k}}}{\partial\omega'} \\ \frac{\partial\omega^{\parallel}}{\partial\theta'_{\mathbf{k}}} & \frac{\partial\omega^{\parallel}}{\partial\phi'_{\mathbf{k}}} & \frac{\partial\omega^{\parallel}}{\partial\omega'} \end{vmatrix} \\ &= \frac{1}{\Delta[\beta,\theta(\theta'_{\mathbf{k}})]}\begin{vmatrix} \frac{\partial\theta^{\parallel}_{\mathbf{k}}}{\partial\theta'_{\mathbf{k}}} & \frac{\partial\theta^{\parallel}_{\mathbf{k}}}{\partial\phi'_{\mathbf{k}}} \\ \frac{\partial\phi^{\parallel}_{\mathbf{k}}}{\partial\theta'_{\mathbf{k}}} & \frac{\partial\phi^{\parallel}_{\mathbf{k}}}{\partial\phi'_{\mathbf{k}}} \end{vmatrix}\end{aligned} \tag{4.36}$$

and $\theta(\theta'_{\mathbf{k}})$ expresses θ from frame F in terms of frame F' coordinates. Specifically, $\theta(\theta'_{\mathbf{k}})$ is obtained by taking the inverse of Eq. (4.26), which is achieved upon substitution of $\beta \to -\beta$.

In this section, the first step of the FHM was completed, where the incident field was boosted to frame F'. Moreover, the effects of Lorentz boosting on the angle of incidence and frequency of the incident field were discussed and visualised. In the next section, step 2 of the FHM will be carried out, where the scattering problem will be solved using Mie theory in the sphere's frame F'.

4.4 Solving the scattering problem in the sphere's reference frame

To start obtaining the scattered field in F', a spherical basis formulation will now be employed for $|\mathbf{E}'_{\mathrm{i}}\rangle$. This basis change allows one to implement the T–matrix method from Mie theory, which is used here since the scattering object is a sphere. The reason why the plane-wave basis was used until now is because one retains all information about the incident field this way. When converting to spherical waves, the incident field is expressed as a sum of its multipolar components represented by ℓ and m (c.f. Section 2.2). This multipolar sum is infinitely long and must be truncated at some point, thus leading to information loss. For the scattered field, this truncation isn't a problem if the scatterer is small enough. In this case, one can often find a multipolar order ℓ at which the scattered field converges. Of course, the truncation order also depends on the material from which the scatterer is made.

A further reason why the plane-wave basis was important for the incident field is due to the behaviour of multipoles under Lorentz boosts. As shown in [119], a boosted multipole generates infinitely many higher order terms, meaning a dipole in F is not a dipole in F', for example. A more in-depth comparison of boosting plane waves and multipoles will be presented in the following chapter.

Returning to the task at hand, the spherical-basis representation of the incident field $|\mathbf{E}'_{\mathrm{i}}\rangle$ in F' takes the form

$$\left|\mathbf{E}'_{\mathrm{i}}\right\rangle = \sum_{\lambda'\ell'm'} \int_{0^+}^{\infty} \mathrm{d}\omega' \mathcal{A}'_{\lambda'\ell'm'}(\omega') \left|\omega'\,\lambda'\,\ell'\,m'\right\rangle^{(1)} + \mathrm{c.c.}, \tag{4.37}$$

where the ket $|\omega'\,\lambda'\,\ell'\,m'\rangle^{(1)}$ represents the helical VSH $\mathbf{\Lambda}^{(1)}_{\lambda',\ell'\,m'}(k'\mathbf{r}')$ given in Eq. (2.38) in Dirac notation. Recall that the '(1)' superscript in Eq. (4.37) denotes that the VSH is described by the first-order spherical Bessel function $j_{\ell'}(k'r')$.

Moreover, the spherical expansion coefficients $\mathcal{A}'_{\lambda'\ell'm'}(\omega')$ are related to the plane-wave expansion coefficients $\mathcal{G}'_{\lambda'}(\omega', \theta'_{\mathbf{k}}, \phi'_{\mathbf{k}})$ via a transformation function $\mathcal{S}_{\lambda'\,\ell'\,m'}(\theta'_{\mathbf{k}}, \phi'_{\mathbf{k}})$ given by [120, Eq. (9)]

$$\mathcal{S}_{\lambda'\,\ell'\,m'}(\theta'_{\mathbf{k}}, \phi'_{\mathbf{k}}) = 4\pi \mathrm{i}^{\ell'+2m'-1}\, \tilde{\Omega}_{\ell'm'} \tau^{(\lambda')}_{\ell'm'}(\theta'_{\mathbf{k}})\, \mathrm{e}^{-\mathrm{i}m'\phi'_{\mathbf{k}}}, \tag{4.38}$$

such that

$$\mathcal{A}'_{\lambda'\ell'm'}(\omega') = \int_0^{2\pi} \mathrm{d}\phi'_{\mathbf{k}} \int_0^{\pi} \mathrm{d}\theta'_{\mathbf{k}}\, \mathcal{G}'_{\lambda',\mathrm{i}}(\omega', \theta'_{\mathbf{k}}, \phi'_{\mathbf{k}}) \mathcal{S}_{\lambda'\ell'm'}(\theta'_{\mathbf{k}}, \phi'_{\mathbf{k}}). \tag{4.39}$$

The quantity $\tilde{\Omega}_{\ell'm'}$ is the adjusted normalisation defined in Eq. (4.1), and $\tau^{(\lambda')}_{\ell'm'}(\theta'_{\mathbf{k}})$ is defined as

$$\tau^{(\lambda')}_{\ell'm'}(\theta'_{\mathbf{k}}) = -\tau_{\ell'm'}(\theta'_{\mathbf{k}}) - \lambda\pi_{\ell'm'}(\theta'_{\mathbf{k}}), \tag{4.40}$$

where $\tau_{\ell' m'}(\theta'_{\mathbf{k}})$ and $\pi_{\ell' m'}(\theta'_{\mathbf{k}})$ are defined in Eqs (2.37) and (2.36), respectively.

Fully simplified, the coefficients $\mathcal{A}'_{\lambda' \ell' m'}(\omega')$ take the form

$$\begin{aligned}\mathcal{A}'_{\lambda' \ell' m'}(\omega') = 4\pi \mathrm{i}^{\ell'+2m'-1} \tilde{\Omega}_{\ell' m'} \tau^{(\lambda')}_{\ell' m'}(\theta'_0) \frac{\Delta[\beta, \theta(\theta'_0)]}{\beta\gamma\omega' \Delta(-\beta, \theta'_0) \sin\theta'_0} \xi(\omega') \\ \cdot \int_0^{2\pi} \mathrm{d}\phi'_{\mathbf{k}} \Big\{ \mathrm{e}^{-\mathrm{i}m'\phi'_{\mathbf{k}}} \mathcal{P}\left[\theta^{\parallel}_{\mathbf{k}}(\theta'_0, \phi'_{\mathbf{k}}), \phi^{\parallel}_{\mathbf{k}}(\theta'_0, \phi'_{\mathbf{k}}), \Theta_{\mathrm{i}}\right] \mathcal{J}(\theta'_0, \phi'_{\mathbf{k}}, \Theta_{\mathrm{i}}) \\ \cdot \mathcal{G}^{\parallel,0}_{\lambda',\mathrm{i}}[\theta^{\parallel}_{\mathbf{k}}(\theta'_0, \phi'_{\mathbf{k}}), \phi^{\parallel}_{\mathbf{k}}(\theta'_0, \phi'_{\mathbf{k}})] \Big\},\end{aligned} \tag{4.41}$$

where the term

$$\xi(\omega') = \delta\left\{\omega' \in \left[\frac{\omega_{\mathrm{i}}}{\gamma(1+\beta)}, \frac{\omega_{\mathrm{i}}}{\gamma(1-\beta)}\right]\right\} \tag{4.42}$$

ensures the correct range of values for the boosted frequency ω'. This range is found by considering Eq. (4.28) when $\theta_{\mathbf{k}} = \Theta_{\mathrm{i}}$. Specifically, the minimum value of ω' corresponds to $\Theta_{\mathrm{i}} = 0$ since this corresponds to the object moving directly away from the incident field, thus maximising the red-shift for a given β. Conversely, the maximum value of ω' corresponds to $\Theta_{\mathrm{i}} = \pi$. Here, the object moves directly towards the incident field, which maximises the blue-shift.

Also present in Eq. (4.41) is $\mathcal{G}^{\parallel,0}_{\lambda',\mathrm{i}}$ obtained from the equation for the Gaussian profile as viewed in $F^{\parallel}$

$$\mathcal{G}^{\parallel}_{\lambda^{\parallel},\mathrm{i}}(\omega^{\parallel}, \theta^{\parallel}_{\mathbf{k}}, \phi^{\parallel}_{\mathbf{k}}) = \mathcal{G}^{\parallel,0}_{\lambda^{\parallel},\mathrm{i}}(\theta^{\parallel}_{\mathbf{k}}, \phi^{\parallel}_{\mathbf{k}}) \delta(\omega^{\parallel} - \omega_{\mathrm{i}}) \tag{4.43}$$

in terms of the F' quantities.

Worth noting in Eq. (4.41) is the parameter θ'_0 given by

$$\theta'_0(\beta, \omega') = \arccos\left(\frac{\omega_{\mathrm{i}} - \gamma\omega'}{\beta\gamma\omega'}\right) \quad . \tag{4.44}$$

The behaviour of $\theta'_0(\beta, \omega')$ in the limit of $\beta \to 0$ demonstrates the validity of the derivations so far. As $\beta \to 0$, the expansion coefficients of the incident field $\mathcal{A}'_{\lambda' \ell' m'}(\omega')$ tend to resemble a δ–distribution. This is to be expected, since the corresponding unboosted Gaussian beam has a very large waist and is approximately a monochromatic plane wave. Due to the fact that such a plane wave only has incident field coefficients at one frequency, the appearance of the δ–distribution provides a useful sanity check.

A plot of a dipolar coefficient $|\mathcal{A}'_{\lambda' 10}(\omega')|$ is provided in Fig. 4.6 for $\beta \in \{0.1, 0.2, 0.5, 0.9\}$ and $\Theta_{\mathrm{i}} = \pi/4$ as a function of the normalised frequency $(\omega_{\mathrm{i}} - \omega')/\omega_{\mathrm{i}}$. Here, the δ–distribution behaviour is evident. Also expected is the decrease in $|\mathcal{A}'_{\lambda' 10}(\omega')|$ as the speed increases. The reason for this decrease is, as shown in Eq. (3.32) in Chapter 3, the amplitude of an electric field is perceived to decrease by an object moving away from it. Armed with the incident field coefficients, the scattered field $|\mathbf{E}_{\mathrm{s}}\rangle$ can now be determined, where the 's' subscript stands for 'scattered'. As was the case with the incident field, the scattered field can be expressed as a sum of its multipolar contributions as follows:

$$\left|\mathbf{E}'_{\mathrm{s}}\right\rangle = \sum_{\lambda' \ell' m'} \int_{0^+}^{\infty} \mathrm{d}\omega' \mathcal{B}'_{\lambda'_{\mathrm{s}} \ell' m'}(\omega') \left|\omega'\ \lambda'_{\mathrm{s}}\ \ell'\ m'\right\rangle^{(3)} + \mathrm{c.c.}, \tag{4.45}$$

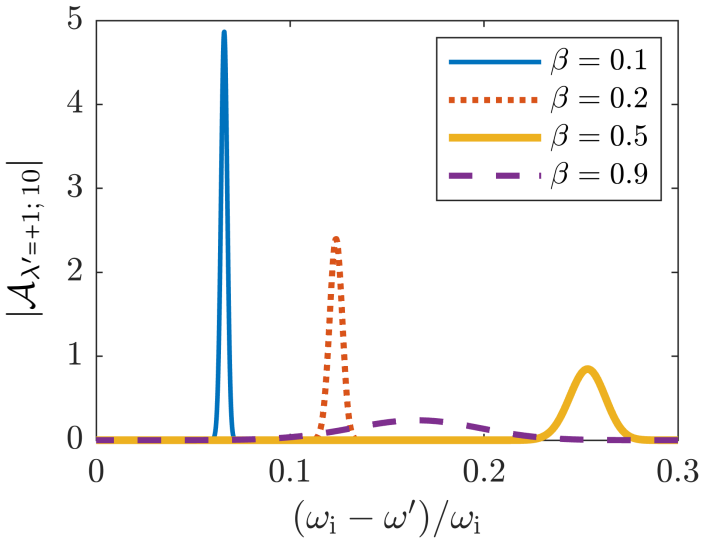

Figure 4.6: The magnitude of a dipolar incident field expansion coefficient $|\mathcal{A}'_{\lambda'10}(\omega')|$ as a function of the normalised boosted frequency $(\omega_\mathrm{i} - \omega')/\omega_\mathrm{i}$, where ω_i is the unboosted frequency and $\lambda' = +1$. Four speeds $\beta \in \{0.1, 0.2, 0.5, 0.9\}$ are considered. As $\beta \to 0$, $|\mathcal{A}'_{\lambda'10}(\omega')|$ approaches a δ-function-like peak, characteristic of a beam with a very large waist. Adapted from [P1]. Copyright © 2023 American Physical Society.

where the '(3)' superscript denotes that the corresponding VSH is described by the third-order spherical Bessel function (also referred to as the first-order spherical Hankel function) $h_{\ell'}(k'r')$.

At this point, the T–matrix formalism can now be implemented. Since the incident and scattered fields are expressed in the helicity basis, one requires the helicity T–matrix $\mathbf{T}^\mathrm{H}$ defined in Eq. (2.64). In matrix notation, the scattered field coefficients $\mathcal{B}'_{\lambda'_\mathrm{s}\ell'm'}(\omega')$ are related to those of the incident field $\mathcal{A}'_{\lambda'_\mathrm{s}\ell'm'}(\omega')$ as

$$\mathbf{B}' = \mathbf{T}^\mathrm{H}\mathbf{A}'\,, \tag{4.46}$$

where

$$\mathbf{A}' = \begin{pmatrix} \mathbf{A}'^{+} \\ \mathbf{A}'^{-} \end{pmatrix}, \quad \mathbf{B}' = \begin{pmatrix} \mathbf{B}'^{+} \\ \mathbf{B}'^{-} \end{pmatrix} \tag{4.47}$$

are $2\ell_\mathrm{max}(\ell_\mathrm{max}+2) \times 1$ vectors and ℓ_max is the maximum considered multipolar order. The $\ell_\mathrm{max}(\ell_\mathrm{max}+2) \times 1$ vectors $\mathbf{A}'^{+}$ and $\mathbf{A}'^{-}$ contain the positive and negative helicity incident field expansion coefficients, respectively. The vectors $\mathbf{B}'^{+}$ and $\mathbf{B}'^{-}$ contain the analogous information but for the scattered field. For example, an incident and scattered field expressed up to quadrupolar order ($\ell_\mathrm{max} = 2$) is described by 16×1 vectors with the following expan-

sion coefficients:

$$\mathbf{A}'^{\pm} = \begin{pmatrix} \mathcal{A}'_{\lambda'_\mathrm{i}=\pm1,\,\ell'=1,\,m'=-1} \\ \mathcal{A}'_{\lambda'_\mathrm{i}=\pm1,\,\ell'=1,\,m'=0} \\ \mathcal{A}'_{\lambda'_\mathrm{i}=\pm1,\,\ell'=1,\,m'=1} \\ \mathcal{A}'_{\lambda'_\mathrm{i}=\pm1,\,\ell'=2,\,m'=-2} \\ \mathcal{A}'_{\lambda'_\mathrm{i}=\pm1,\,\ell'=2,\,m'=-1} \\ \mathcal{A}'_{\lambda'_\mathrm{i}=\pm1,\,\ell'=2,\,m'=0} \\ \mathcal{A}'_{\lambda'_\mathrm{i}=\pm1,\,\ell'=2,\,m'=1} \\ \mathcal{A}'_{\lambda'_\mathrm{i}=\pm1,\,\ell'=2,\,m'=2} \end{pmatrix}, \quad \mathbf{B}'^{\pm} = \begin{pmatrix} \mathcal{B}'_{\lambda'_\mathrm{s}=\pm1,\,\ell'=1,\,m'=-1} \\ \mathcal{B}'_{\lambda'_\mathrm{s}=\pm1,\,\ell'=1,\,m'=0} \\ \mathcal{B}'_{\lambda'_\mathrm{s}=\pm1,\,\ell'=1,\,m'=1} \\ \mathcal{B}'_{\lambda'_\mathrm{s}=\pm1,\,\ell'=2,\,m'=-2} \\ \mathcal{B}'_{\lambda'_\mathrm{s}=\pm1,\,\ell'=2,\,m'=-1} \\ \mathcal{B}'_{\lambda'_\mathrm{s}=\pm1,\,\ell'=2,\,m'=0} \\ \mathcal{B}'_{\lambda'_\mathrm{s}=\pm1,\,\ell'=2,\,m'=1} \\ \mathcal{B}'_{\lambda'_\mathrm{s}=\pm1,\,\ell'=2,\,m'=2} \end{pmatrix}. \tag{4.48}$$

Recall that the incident field only contains positive helicity components ($\lambda_\mathrm{i} = +1$) such that $\mathbf{A}'^{-} = \mathbf{0}_{\ell_{\max}(\ell_{\max}+2)}$ and

$$\mathbf{A}' = \begin{pmatrix} \mathbf{A}'^{+} \\ \mathbf{0}_{\ell_{\max}(\ell_{\max}+2)} \end{pmatrix}, \tag{4.49}$$

where $\mathbf{0}_{\ell_{\max}(\ell_{\max}+2)}$ is the $\ell_{\max}(\ell_{\max}+2) \times 1$ zero vector. Important to note is that, although the incident field only has positive helicity components, the same does not necessarily apply to the scattered field. In general, the scattered field can contain components of both positive and negative helicity. In special cases, the scattered and incident field helicities can indeed be equal, where the scatterer is said to be 'dual' [121]. A dual scatterer is characterised by equal electric and magnetic Mie coefficients, where $a_\ell = b_\ell$. Recall that the expressions for a_ℓ and b_ℓ are given by Eqs (2.58) and (2.59), respectively.

In this chapter, it is assumed that $\mathbf{T}^\mathrm{H}$ is frequency-independent (non-dispersive). One can make this assumption due to the large waist of the incident Gaussian beam. A large waist implies a narrow angular spectrum. In other words, the angles of orientation of the constituent plane waves are approximately equal to each other. Consequently, the Doppler shifts of each plane wave are very similar, which especially holds if β is not too large. As seen in Fig. 4.6, a speed corresponding to $\beta = 0.2$ still gives rise to a small range of Doppler-shifted frequencies, making a non-dispersive T–matrix a fair approximation. As the speed increases, the assumption of a non-dispersive T–matrix becomes less favourable. For example, one also sees in Fig. 4.6 that the range of boosted frequencies becomes quite broad when $\beta = 0.9$. For large speeds, dispersion effects should ideally be taken into account. A frequency dependent T–matrix will be considered in all future chapters.

Upon obtaining the scattered field $|\mathbf{E}'_\mathrm{s}\rangle$, a further assumption is made that the sphere is far away from the observer in frame F. Accordingly, only the far field needs to be considered. To obtain the far field, one takes the limit of $r' \to \infty$, where $r' = |\mathbf{r}'|$ is distance from the sphere perceived in F' at which the scattered field signal is recorded. Recall that $\mathbf{r}'$ is defined in Eq. (3.19).

In the far field limit, the ket $|\omega'\, \lambda'_\mathrm{s}\, \ell'\, m'\rangle^{(3)}$ describing the scattered field takes the form of Eq. (2.45), where

$$\lim_{r'\to\infty} \left|\omega'\, \lambda'\, m'\, \ell'\right\rangle^{(3)} \equiv (-\mathrm{i})^{\ell'}\, \mathbf{f}_{\lambda',\ell'm'}(\hat{\mathbf{r}}')\, \frac{\mathrm{e}^{\mathrm{i}\omega'(r'/c-t')}}{\omega' r'/c}, \tag{4.50}$$

and the expressions for $\mathbf{f}_{\lambda',\ell'm'}(\hat{\mathbf{r}}')$ and t' are given in Eq. (2.40) and Eq. (3.20), respectively.

Upon substitution of Eq. (4.50) into Eq. (4.45), one readily obtains the final required form of the scattered electric field $\mathbf{E}_{\mathrm{s}}^{\prime\mathrm{ff}}(\mathbf{r}',t')$:

$$\mathbf{E}_{\mathrm{s}}^{\prime\mathrm{ff}}(\mathbf{r}',t') = \sum_{\lambda'\ell'm'} \int_0^\infty \mathrm{d}\omega' \mathcal{B}'_{\lambda'\ell'm'}(\omega')(-\mathrm{i})^{\ell'} \mathbf{f}_{\lambda',\ell'm'}(\hat{\mathbf{r}}') \, \frac{\mathrm{e}^{\mathrm{i}\omega'(r'/c-t')}}{\omega' r'/c} + \mathrm{c.c.}, \tag{4.51}$$

where the superscript 'ff' stands for 'far field'.

With the far field scattered electric field at hand, one is now able to form an expression for the scattered energy density $U'(\theta',\phi')$ in frame F' in a direction defined by the polar and azimuthal angles θ' and ϕ', respectively. Explicitly, one has

$$U'(\theta',\phi') = \int_{-\infty}^{\infty} (r')^2 \frac{|\mathbf{E}_{\mathrm{s}}^{\prime\mathrm{ff}}(\mathbf{r}',t')|^2}{\eta_0} \mathrm{d}t', \tag{4.52}$$

where η_0 denotes the impedance of free space.

To summarise this section, the second step of the FHM was carried out, where the scattered energy density $U'(\theta',\phi')$ in a particular direction θ' and ϕ' was determined in frame F'. In the following section, the final step of the FHM will be executed, and the directivity will be determined and minimised in frame F. In other words, a relativistic Kerker condition will be devised.

4.5 Obtaining the backscattered energy in the lab frame

In this section, the third and final step of the FHM will be carried out, where the angular scattered energy density will be inverse Lorentz boosted from frame F' to frame F. It is in frame F where the directivity will be observed.

4.5.1 Defining the directivity

As mentioned, the quantity that will be explored is the directivity $D(\theta,\phi,\beta)$ in frame F, which is defined as [115]

$$D(\theta,\phi,\beta) = \frac{U(\theta,\phi,\beta)}{W_{\mathrm{tot}}/4\pi}, \tag{4.53}$$

where θ and ϕ denote the polar and azimuthal angles at which the directivity is observed in frame F, respectively. The total angular scattered energy density $U(\theta,\phi,\beta)$ in frame F is the sum of its $\lambda_{\mathrm{s}}=+1$ and $\lambda_{\mathrm{s}}=-1$ components $U_{\lambda_{\mathrm{s}}}(\theta,\phi,\beta)$, such that

$$U(\theta,\phi,\beta) = \sum_{\lambda_{\mathrm{s}}} U_{\lambda_{\mathrm{s}}}(\theta,\phi,\beta). \tag{4.54}$$

The quantity W_{tot} in Eq. (4.53) is the total scattered energy and is determined by integrating $U(\theta,\phi,\beta)$ over all scattering directions:

$$W_{\mathrm{tot}} = \int_0^{2\pi} \int_0^{\pi} U(\theta,\phi,\beta) \sin\theta \mathrm{d}\theta \mathrm{d}\phi. \tag{4.55}$$

Important to mention is the 4π that appears in the denominator of Eq. (4.53), which serves as a normalisation factor for W_{tot}. Physically speaking, the normalised quantity $W_{\text{tot}}/4\pi$ resembles the average scattered energy per unit solid angle by the sphere. The advantage of considering the directivity is that it allows one to easily conceptualise how much of the scattered energy is concentrated in a particular direction. For example, when $D(\theta, \phi) > 1$, scattering in the (θ, ϕ) direction dominates scattering in other directions. On the other hand, a directivity of $D(\theta, \phi) < 1$ means that the scattered signal is more strongly concentrated in directions away from that described by θ and ϕ. Since backscattering is considered in this chapter, the corresponding polar and azimuthal scattering angles are

$$\Theta_{\text{BS}} = \pi - \Theta_{\text{i}} \quad \text{and} \quad \Phi_{\text{BS}} = \pi, \tag{4.56}$$

respectively, where the subscript 'BS' stands for 'backscattered'.

To carry out the final step of the FHM, one needs to inverse Lorentz boost the angular scattered energy density $U'(\theta', \phi')$ in frame F' to the corresponding quantity $U(\theta, \phi)$ in frame F. The equation to do this is given in [30, Eq. (21)] and reads

$$U(\theta, \phi, \beta) = [\Delta(-\beta, \theta')]^3 \, U'(\theta', \phi'), \tag{4.57}$$

where $\Delta(-\beta, \theta')$ is obtained using Eq. (3.6), and θ and ϕ are related to θ' and ϕ' via Eqs (4.26) and (4.27), respectively.

Since this chapter is concerned with minimising the backscattered signal, it makes sense to separately define the backscattered directivity D_{BS}, where

$$D_{\text{BS}}(\beta) = D(\Theta_{\text{BS}}, \Phi_{\text{BS}}, \beta). \tag{4.58}$$

The backscattered directivity $D_{\text{BS}}(\beta)$ in Eq. (4.58) is the quantity to be investigated later in this chapter. At this point, the final step of the FHM is complete.

To explore how the directivity changes depending on the geometric nature of the sphere, one can consider the variation of the Mie coefficients a_ℓ and b_ℓ defined in Eqs. (2.58) and (2.59), respectively. Although one could correspondingly vary the radius of the sphere, a more abstract approach is possible in the form of Mie angles. Mie angles represent all possible Mie coefficients an object could have and allow for a comprehensive visualisation of the directivity for different spherical objects. Mie angles will be discussed in depth in the next subsection.

4.5.2 Mie angles

Although the Mie coefficients a_ℓ and b_ℓ can be expressed explicitly in terms of the frequency of the incoming light and the radius of the sphere, it can also be useful to form a more abstract picture using what are known as Mie angles [122]. Mie angles allow one to visualise via a parametrisation the scattering response for every possible combination of Mie coefficients up to any multipolar order. This paremetrisation can be derived from the scattering, extinction and absorption cross sections C_{sca}, C_{ext} and C_{abs}, respectively, which are given

as [123]:

$$C_{\mathrm{sca}} = \frac{L^2}{2\pi}\sum_{\ell=1}^{\infty}(2\ell+1)(|a_\ell|^2+|b_\ell|^2), \tag{4.59}$$

$$C_{\mathrm{ext}} = \frac{L^2}{2\pi}\sum_{\ell=1}^{\infty}(2\ell+1)\mathrm{Re}(a_\ell+b_\ell), \tag{4.60}$$

$$C_{\mathrm{abs}} = \frac{L^2}{2\pi}\sum_{\ell=1}^{\infty}(2\ell+1)\left[\mathrm{Re}(a_\ell+b_\ell)-(|a_\ell|^2+|b_\ell|^2)\right], \tag{4.61}$$

where L is the wavelength of the incident field. To derive Mie angle parametrisation, one only needs to consider either the electric or magnetic components of Eqs. (4.59, 4.60, 4.61) since both yield the same parametrisation. Considering only the electric part, one obtains for a given multipolar order ℓ

$$C_{\mathrm{sca,E}\ell} = \frac{L^2}{2\pi}(2\ell+1)|a_\ell|^2, \tag{4.62}$$

$$C_{\mathrm{ext,E}\ell} = \frac{L^2}{2\pi}(2\ell+1)\mathrm{Re}(a_\ell), \tag{4.63}$$

$$C_{\mathrm{abs,E}\ell} = \frac{L^2}{2\pi}(2\ell+1)[\mathrm{Re}(a_\ell)-|a_\ell|^2], \tag{4.64}$$

where

$$C_{\mathrm{ext,E}\ell} = C_{\mathrm{abs,E}\ell} + C_{\mathrm{sca,E}\ell}. \tag{4.65}$$

Armed with Eq. (4.65), one can now determine the Mie angle parametrisation. In this chapter, only Mie angles for a non-absorbing sphere are implemented. Accordingly, one has that $C_{\mathrm{abs,E}\ell} = 0$ such that $C_{\mathrm{ext,E}\ell} = C_{\mathrm{sca,E}\ell}$. From Eqs.(4.62, 4.63), one therefore finds that

$$\mathrm{Re}(a_\ell) = |a_\ell|^2, \tag{4.66}$$

which means that [122, Eq. (8)]

$$a_\ell = \cos(\theta_{\mathrm{E}\ell})\exp(\mathrm{i}\theta_{\mathrm{E}\ell}), \tag{4.67}$$

where $-\pi/2 \leq \theta_{\mathrm{E}\ell} \leq \pi/2$ is the electric Mie angle. Recall that the equation for the magnetic Mie coefficients b_ℓ with Mie angles $\theta_{\mathrm{M}\ell}$ takes the same form as Eq. (4.67).

Particular values for the Mie angles represent noteworthy features. For example, when $\theta_{\mathrm{X}\ell} = 0$ (where $\mathrm{X} \in \{\mathrm{E}, \mathrm{M}\}$) the corresponding Mie coefficient has a resonance. When $\theta_{\mathrm{X}\ell} = \pm\pi/2$, the corresponding Mie coefficient becomes zero. Physically speaking, all Mie angles having a value of $\pm\pi/2$ is equivalent to a vanishing scatterer.

4.5.3 Visualising the directivity - varying Mie angles

After having introduced Mie angles as a means to investigate the directivity of a wide range of possible spheres, one is now in a position to visualise the resulting scattering responses. Various directivity patterns will now be explored to aid physical understanding.

One is now free to choose Mie angles up to any multipolar order as the independent variables of the directivity. In this subsection, the electric θ_{ED} and magnetic θ_{MD} dipolar Mie angles will be held constant, where $\theta_{\mathrm{ED}} = \theta_{\mathrm{E1}}$ and $\theta_{\mathrm{MD}} = \theta_{\mathrm{M1}}$, respectively. The parameters to be varied are the quadrupolar Mie angles $\theta_{\mathrm{EQ}} = \theta_{\mathrm{E2}}$ and $\theta_{\mathrm{MQ}} = \theta_{\mathrm{M2}}$.

Colour plots of the $\lambda_{\mathrm{s}} = +1$ and $\lambda_{\mathrm{s}} = -1$ of $\log_{10}(D_{\mathrm{BS}})$ are shown in Figs. 4.7 (a) and (b), respectively, where $\beta = 0.2$, $\Theta_{\mathrm{i}} = \pi/4$ and $\theta_{\mathrm{ED}} = \theta_{\mathrm{MD}} = \pi/3$. In Fig. 4.7 (c), the corresponding plot for the total directivity is given.

In Fig. 4.7 (b) where $\lambda_{\mathrm{s}} = -\lambda_{\mathrm{i}} = -1$, one sees an example of the previously mentioned duality. Recall that duality occurs when the electric and magnetic Mie angles are equal for each multipolar order ℓ. In Fig. 4.7 (b), duality manifests itself as the dark blue diagonal line where $\theta_{\mathrm{EQ}} = \theta_{\mathrm{MQ}}$ and $\log_{10}(D_{\mathrm{BS}}) = -\infty$. In other words, the $\lambda_{\mathrm{s}} = -1$ component of D_{BS} expectedly vanishes. Such a feature serves as a useful sanity check that D_{BS} was correctly derived. Correspondingly, only the $\lambda_{\mathrm{s}} = +1$ components of D_{BS} survive in the dual case, as shown in Fig. 4.7 (a).

For completion, a non-trivial backscattered directivity pattern is given in Fig. 4.7 (d), where $\theta_{\mathrm{ED}} = \pi/9$ and $\theta_{\mathrm{MD}} = -\pi/4$. The appearance of local minima indicate exotic combinations of Mie angles that yield little backscattering, serving as a motivation to devise a relativistic Kerker condition in the following section. However, the directivity will firstly be investigated for a varying object speed and incident field angle. Afterwards, one will have obtained a comprehensive understanding of how the directivity behaves in many settings.

4.5.4 Visualising the directivity – varying speed and angle of incidence

As well as employing Mie angles as independent variables for the backscattered directivity, one is also able to vary the speed parameter β and angle of incidence Θ_{i}. For a fixed set of Mie angles $\theta_{\mathrm{ED}} = \pi/4$, $\theta_{\mathrm{EQ}} = -\pi/9$, $\theta_{\mathrm{MD}} = \pi/3$ and $\theta_{\mathrm{MQ}} = \pi/7$, the corresponding colour plot of $\log_{10}(D_{\mathrm{BS}})$ is presented in Fig. 4.8. Here, another sanity check is evident for the case of a stationary sphere ($\beta = 0$), where D_{BS} is invariant with respect to Θ_{i}. Such an invariance is expected since the scatterer is viewed as a sphere in frame F in the stationary case as opposed to an ellipsoid when moving (c.f. Fig. 3.3). Owing to the spherical symmetry, the directivity should not and does not depend on the angle of incidence.

The other extreme of $\beta \to 1$ is also worth commenting on, where the exact same behaviour is observed as in Fig. 3.6 showing the boosted energy density $u'(\beta, z')$ of a plane wave. This is expected, since the incident Gaussian beam comprises many plane waves whose energy densities vary in accordance with Eq. (3.34) for $u'(\beta, z')$. Specifically, when $\Theta_{\mathrm{i}} = 0$, the sphere moves away from the incident field. As a result, the sphere observes an incident field with vanishing amplitude, leading to a vanishing backscattered energy density and directivity. Conversely, the sphere observes an infinitely large field amplitude when it moves directly towards from the incident field ($\Theta_{\mathrm{i}} = \pi$), thus giving rise to an ever-increasing backscattered energy density and directivity.

Although Mie angles allow one to explore the directivity relating to all possible spherical scatterers, the method used in this chapter can also be applied to known materials. In the following subsection, the backscattered directivity of a silicon carbide sphere will be investigated as a function of its radius.

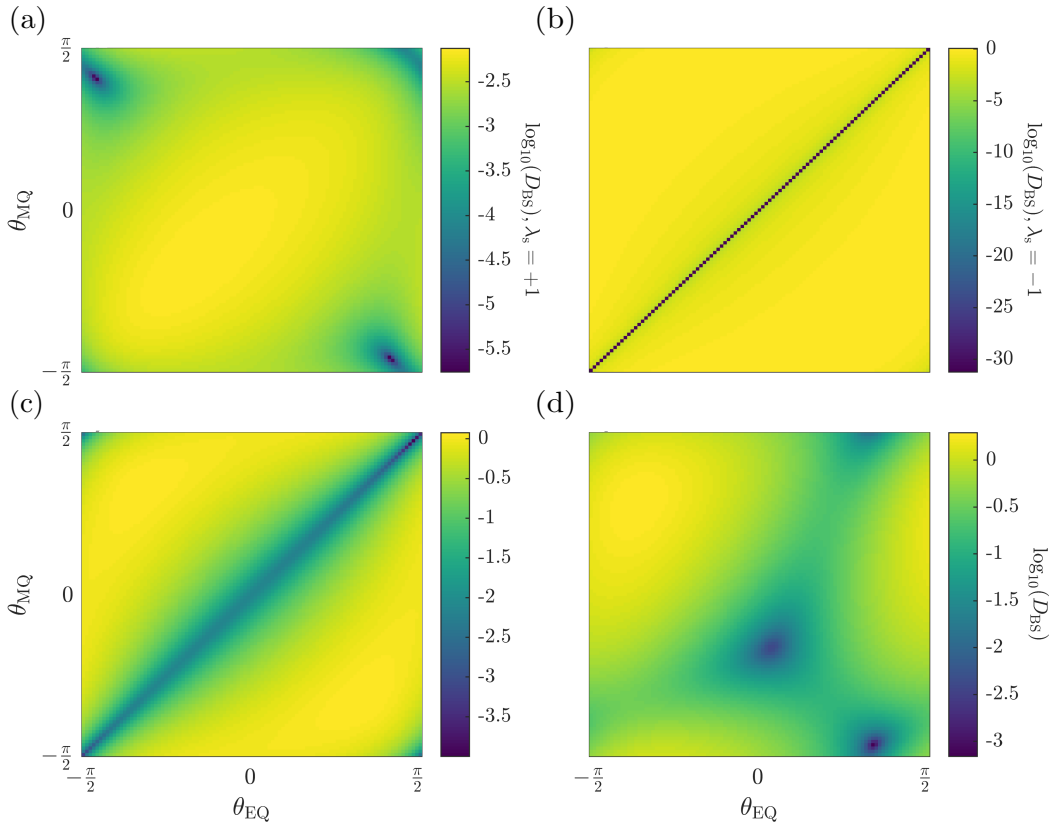

Figure 4.7: In (a) and (b) are the $\lambda_{\mathrm{s}} = +1$ and $\lambda_{\mathrm{s}} = -1$ components of the backscattered directivity D_{BS} (in $\log_{10}$ scale) as a function of the quadrupolar Mie angles θ_{EQ} and θ_{MQ}. The speed of the sphere and incident field angle are fixed at $\beta = 0.2$ and $\Theta_{\mathrm{i}} = \pi/4$, respectively. The sum of both components of D_{BS} is given in (c). In (a), (b) and (c), the dipolar Mie angles are fixed at $\theta_{\mathrm{ED}} = \theta_{\mathrm{MD}} = \pi/3$. In (d), $\log_{10}(D_{\mathrm{BS}})$ is plotted for fixed dipolar Mie angles $\theta_{\mathrm{ED}} = \pi/9$ and $\theta_{\mathrm{MD}} = -\pi/4$. Adapted from [P1]. Copyright © 2023 American Physical Society.

4.5.5 The directivity of a silicon carbide (SiC) sphere

Although Mie angles have been implemented until now, the method in this chapter also has practical applications. Here, the backscattered directivity of a sphere made out of silicon-carbide (SiC) with refractive index $n_{\mathrm{SiC}} = 2.59$ is considered. This value for n_{SiC} was obtained from the high-frequency-limit permittivity $\epsilon_\infty = 6.7$ [100]. Accordingly, the wavelength of the incident beam in frame F is taken to be $L = 1\mu\mathrm{m}$. Furthermore, the angle of incidence has a value $\Theta_{\mathrm{i}} = \pi/4$. Plots of D_{BS} are given in Fig. 4.9 as a function of the sphere radius R for three speeds $\beta \in \{1 \times 10^{-6}, 0.2, 0.5\}$. Just like before, D_{BS} decreases as $\beta \to 1$ due to the induced red-shift and corresponding decreasing backscattered energy density. Note that the corresponding Mie coefficients were obtained using Eqs (2.58) and (2.59). Moreover, Mie coefficients up to octupolar order were considered to ensure convergence of the results in the given range for R. If one were to consider even larger radii, higher

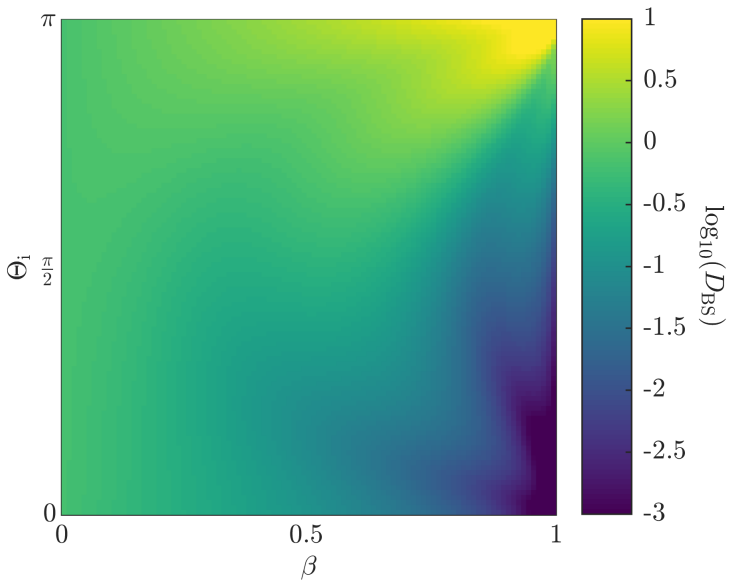

Figure 4.8: The backscattered directivity D_{BS} (in $\log_{10}$ scale) as a function of the speed β of the sphere and the incident field angle Θ_{i}. The Mie angles describing the sphere are fixed at $\theta_{\mathrm{ED}} = \pi/4$, $\theta_{\mathrm{EQ}} = -\pi/9$, $\theta_{\mathrm{MD}} = \pi/3$ and $\theta_{\mathrm{MQ}} = \pi/7$. Reprinted from [P1]. Copyright © 2023 American Physical Society.

multipolar orders would be required as the radius becomes more and more comparable to the wavelength L.

In this section, the final step of the FHM was carried out, and an expression for the backscattered directivity of a sphere was obtained in frame F. The backscattered directivity was also investigated by varying many different parameters. These parameters included the incident field angle, the sphere's speed and its Mie coefficients. Now that a physical intuition for the directivity has been developed, its minimisation can commence and a relativistic Kerker condition can be found.

4.6 Minimising the backscattering - relativistic Kerker condition

4.6.1 Fixed speed and angle of incidence

To begin, the Kerker condition will be formulated for a fixed speed $\beta = 0.2$ and angle of incidence $\Theta_{\mathrm{i}} = \pi/4$. The corresponding directivity minimisation was carried out using the Julia programming language owing to its efficient numerical integration functions. Specifically, the minimisation was done using automatic differentiation, a gradient descent method provided in the toolkit JuMP [124]. The power of automatic differentiation allows one to minimise the backscattered directivity D_{BS} up to any multipolar order. For demonstration purposes, the minimisations in this chapter were carried out up to octupolar order.

To set up the optimisation problem, it was important to avoid finding trivial solutions. Accordingly, the optimisation algorithm excluded the Mie angles $-\pi/2$ and $\pi/2$. The reason for this is that the optimiser would automatically allocate $-\pi/2$ or $\pi/2$ to all Mie angles,

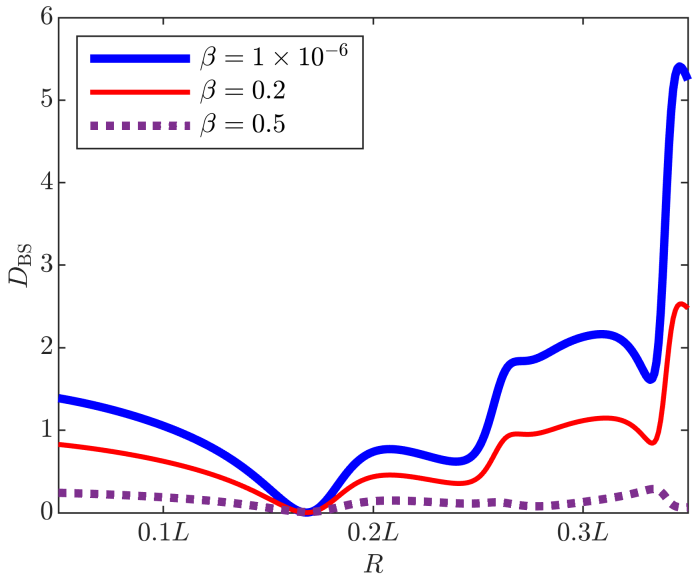

Figure 4.9: The backscattered directivity D_{BS} of a silicon carbide sphere as a function of its radius R for three different speeds $\beta \in \{1 \times 10^{-6}, 0.2, 0.5\}$. The incident field wavelength in frame F is $L = 1\mu\mathrm{m}$, and convergence of D_{BS} occurs with a scattered field expanded up to octupolar order. Reprinted from [P1]. Copyright © 2023 American Physical Society.

which corresponds to a vanishing scatterer. Of course, the backscattered energy density would always be zero if no scatterer were present.

Due to the complex nature of the equation defining the directivity, it would be impossible to find a conventional Kerker condition where the backscattered signal completely disappears. A near-zero solution is possible, however, and the considered directivity cut-off D_{C} in this chapter is $D_{\mathrm{C}} = 10^{-3}$. In other words, a backscattered energy density that comprises 0.1% or less of the average scattered energy per unit solid angle satisfies the relativistic Kerker condition. A set of Mie angles corresponding to the minimised backscattered directivity are given in Table 4.1. In Table 4.1, one sees that the optimiser was able to find Mie angles that yield a value of $D_{\mathrm{BS}} = 1.09 \times 10^{-8}$, way below the cut-off D_{C}. Moreover, the Mie angles describe an approximately dual scatterer. However, duality is not necessary to devise a relativistic Kerker condition and there exist many suitable non-dual systems.

The suitability of the optimised Mie angles in Table. 4.1 will now be tested for different speeds and angles of incidence.

4.6.2 Varying speed and angle of incidence

To build on the results from the previous sub-section, it will now be seen how the optimised Mie angles from Table 4.1 vary with respect to β and Θ_{i}. The reason for this is to check if the optimised Mie angles always lead to a Kerker condition, or if new Mie angles would need to be found. In Figs 4.10 (a) and (b), the angle of incidence has a value $\Theta_{\mathrm{i}} = \pi/4$ while β is varied incrementally to ensure continuous curves for each Mie angle. Large step sizes for β

Table 4.1: The optimised electric and magnetic Mie angles that lead to a minimised backscattered directivity D_{BS}. In other words, the backscattered energy density comprises only $1.09 \times 10^{-6}\%$ of the average scattered energy per unit solid angle. Such a low D_{BS} satisfies the relativistic Kerker condition. Adapted from [P1]. Copyright © 2023 American Physical Society.

θ_{ED}	θ_{MD}	θ_{EQ}	θ_{MQ}	θ_{EO}	θ_{MO}	$10^8 \times D_{\mathrm{BS}}$
0.33	0.32	1.07	1.06	1.44	1.43	1.09

would not reveal much information about the influence of the Mie angles in Table 4.1 since the optimiser would erratically jump between unrelated Mie angle combinations.

One sees in Fig. 4.10 (a) that the Mie angles show a non-negligible variation as β increases. Moreover, the optimised Mie angles from Table 4.1 become unfavourable at $\beta \approx 0.8$, as can be seen in Fig. 4.10 (b). For lower values of β, a Kerker condition is obtained as $D_{\mathrm{BS}} < D_{\mathrm{C}}$ ($\log_{10}(D_{\mathrm{BS}}) \leq -3$ in Fig. 4.10 (b)). However, at $\beta \approx 0.8$, the cut-off D_{C} is surpassed, where $\log_{10}(D_{\mathrm{BS}}) \approx -2$. In this case, a new optimisation should be done to find more suitable Mie angles. Also notable in Fig. 4.10 (b) is the suddenly decreasing backscattered directivity as $\beta \to 1$. This decrease is again due the strong red-shift of the scattered field, which leads to a reduced backscattered energy density.

In Figs 4.10 (c) and (d), the speed is fixed at $\beta = 0.2$ and the angle of incidence Θ_{i} is varied. One notices in Fig. 4.10 (c) that the optimised Mie angles remain almost unchanged as Θ_{i} increases, implying that a varying incident field angle has less impact on the optimised Mie angles than a varying object speed. Furthermore, the Kerker condition is retained for all Θ_{i}, where $\log_{10}(D_{\mathrm{BS}}) \leq -3$. Note that values of $\beta < 0.2$ and $\Theta_{\mathrm{i}} < \pi/4$ were not considered, as the optimiser would trivially locate Mie angles corresponding to a dual object. In any case, all necessary conclusions can be drawn from the considered ranges for β and Θ_{i} in Fig. 4.10.

4.7 Summary

To summarise, the backscattered signal from a relativistically moving sphere was visualised and minimised using gradient descent methods to find a relativistic Kerker condition. The parameters varied for the optimisation included the Mie angles that describe the geometry of the sphere, the speed of the sphere and the incident field angle. The scattered energy was a result of the sphere interacting with an incident Gaussian beam described using the angular spectrum representation. The backscattered energy density was normalised with respect to the average scattered energy by the sphere per unit solid angle, where the resulting figure of merit is known as the backscattered directivity D_{BS}. To obtain D_{BS}, the frame-hopping method (FHM) outlined in the previous chapter was relied upon. The FHM method was easily implemented due to the finite interaction between the sphere and the beam, allowing one to Lorentz-boost the scattered energy directly from frame F' to frame F. It was in frame F where the minimised directivity was observed and a relativistic Kerker condition was devised. Specifically, a sphere was devised that leads to a minimised backscattered energy density that makes up just $1.09 \times 10^{-6}\%$ of the average scattered energy per unit solid angle.

The work done in this chapter serves as a vital prerequisite to more complex systems, such as scattering by a relativistically moving, periodic structure as considered in the following chapter.

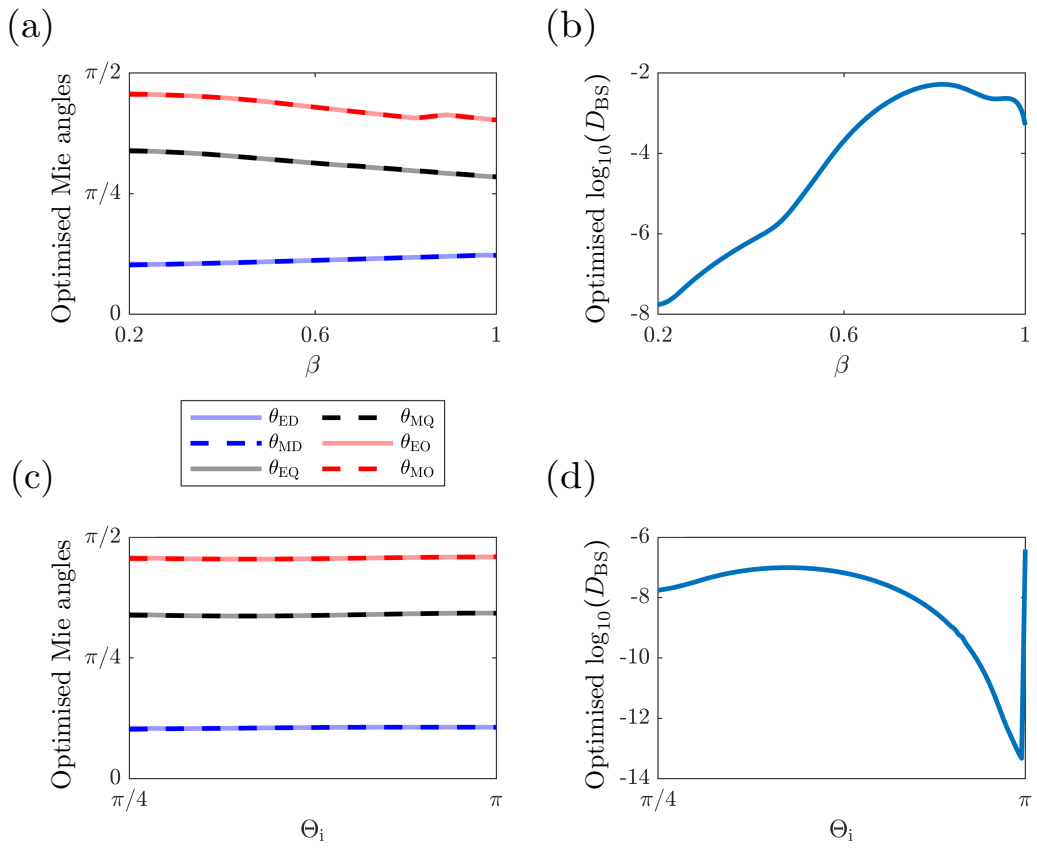

Figure 4.10: In (a), the variation of the optimised Mie angles from Table 4.1 is shown as a function of speed β for a fixed incident field angle $\Theta_{\mathrm{i}} = \pi/4$. The corresponding backscattered directivity variation (in $\log_{10}$ scale) is given in (b). In (c) and (d) are the analogous plots but for varying incident field angle Θ_{i} and fixed speed $\beta = 0.2$. Adapted from [P1]. Copyright © 2023 American Physical Society.

5 | Analysing the Acceleration Time and Reflectance of Spherical-Array Light Sails

This chapter is based on work done in Ref. [P2] with Lukas Rebholz and Benedikt Zerulla and serves as an extension to the previous chapter. Specifically, scattering by relativistically moving lattices of homogenous or core-(multi-)shell spheres will be considered instead of a single sphere. The consideration of a lattice serves as a more direct comparison to light sails proposed in the Breakthrough Starshot Initiative (BSI). With the BSI in mind, the lattice is illuminated by a plane wave with constant intensity. This incident field resembles the lasers that will be used in the BSI to propel the light sail.

When designing a light sail, there are three important aspects to consider.

1. The resulting reflectance from the sail should be as high as possible. A high reflectance corresponds to a large momentum transfer to the sail, thus increasing its acceleration.

2. The corresponding absorptance should be as low as possible to avoid unwanted temperature increases in the sail. A large increase in temperature would lead to thermal damage.

3. The time taken to accelerate the light sail to its target speed should be as small as possible. Accordingly, materials should be chosen that minimise the sail mass while also considering the previous two constraints.

The time taken to accelerate the light sail is known as the acceleration time and will be the figure of merit to be optimised. Two methods of optimisation will be carried out. Firstly, the acceleration time will be minimised without any prior constraints on the reflectance and absorptance. Secondly, the acceleration time will be optimised while ensuring a high reflectance and low absorptance. In a later section, it will be argued why the second method may be more favourable.

The structure of this chapter is as follows. In Section 5.1, the scattering setup will be outlined and all necessary parameters will be defined. in Section 5.2, the acceleration times of three light sail configurations will be investigated. Each light sail consists of periodically arranged homogeneous spheres made from either silicon (Si), silicon dioxide (SiO_2) or aluminium (Al). These three materials have low densities, which is conducive to a reduced acceleration time. In Section 5.3, the same analysis is done for light sails made from core-(multi-)shell spheres. A promising combination of Si and SiO_2 is found that fulfils the three conditions above. In Section 5.4, the multipolar contributions of the scattered field by the light sail made from core-shell Si/SiO_2 spheres are explored. Specifically, the resulting lattice interactions create a high reflectance. Finally, the effects of adding an embedding to the sail are investigated in Section 5.5.

5.1 Description of the scattering scenario

To begin, the scattering scenario will now be outlined. The considered scatterer is a metasurface made up of periodically arranged homogeneous or core-(multi-)shell spheres. The spheres form an infinitely large square lattice that spans the x-y plane. Accordingly, the lattice is characterised by a single lattice constant Λ. Moreover, the light sail is propelled by a linearly-polarised plane-wave electromagnetic field with wavelength L in frame F. Moreover, the light sail moves with velocity $v\hat{\mathbf{z}}$, where $0 \leq v < c$. Unlike in the previous chapter, the incident field only propagates in the $+z$-direction, such that it is always at normal incidence to the light sail. Consequently, the light sail always observes a Doppler-shifted wavelength L' that satisfies Eq. (3.5). Of course, different angles of incidence would be possible but would require considerations of stability. Stability is not considered in this chapter, however, as the focus is on investigating the motion solely due to the effects of lattice interactions. To this end, the sail is firstly assumed to be suspended in a vacuum. Once investigated, the effects of a supporting embedding will be considered in a later section.

The setup described above is depicted in Fig. 5.1. Note that only the subwavelength regime is considered, where $\Lambda < L$. As a result, only zeroth-order reflection occurs, where all reflected light propagates in the $-z$-direction. Furthermore, one can be certain that the lattice always observes an incident wavelength greater than its lattice constant. This condition is justified in two ways: firstly, Λ remains invariant as per Eqs (3.9) and (3.10), which show that no length contraction occurs in the x-y plane for motion purely in the z-direction. Secondly, the Doppler-shifted wavelength observed by the sail in frame F' is always longer than in frame F ($L' > L$), meaning $L' > \Lambda$. The value for the initial propulsion wavelength is $L = 1.0\mu\mathrm{m}$ to conform with the range $L = 1.0\mu\mathrm{m} - 1.5\mu\mathrm{m}$ proposed in the literature [53, 61]. Additionally, the target speed of the sail is given by $v_\mathrm{f} = \beta_\mathrm{f} c$, where $\beta_\mathrm{f} = 0.2$. This value for β_f corresponds to 20% of the speed of light, which is the proposed maximum speed in the BSI [45, 46]. Consequently, the Doppler-shifted wavelengths observed by the sail fall within the range $L' \in [1.0L, 1.225L]$.

In this chapter, three important quantities will be investigated: the reflectance $R(\beta)$, absorptance $A(\beta)$ and acceleration time τ defined as the time required to accelerate the light sail to the target speed v_f. Quantitatively, the acceleration time is related to $R(\beta)$ and $A(\beta)$ as [62, Eq. (1)]

$$\tau = \frac{c^2}{I\Lambda^2} \int_0^{\beta_\mathrm{f}} \frac{\mu_\mathrm{p} + \sum_j^{j_\mathrm{max}} \rho_j V_j}{A(\beta) + 2R(\beta)} \frac{\gamma^3(1+\beta)}{(1-\beta)} \mathrm{d}\beta \,, \tag{5.1}$$

where I is the intensity of the incident field, $\mu_\mathrm{p} = m_\mathrm{p}\Lambda^2/a$ is the mass of the payload m_p per unit cell for a given reference sail area a, and ρ_j and V_j are the density and volume of the j'th section of each sphere, respectively. For example, homogeneous spheres would correspond to a maximum j value of $j_\mathrm{max} = 1$, while core-double shell spheres correspond to $j_\mathrm{max} = 3$. As evident by the Λ^2 term in Eq. (5.1), the acceleration time τ is based on a unit cell, which is depicted in Fig. 5.2 for spheres of radius r. For core-(multi-)shell spheres, r corresponds to the radius of the outermost shell. A unit cell is considered since the metasurface is infinitely extended, so one must consider a portion of it. Furthermore, the $\sum_j^{j_\mathrm{max}} \rho_j V_j$ term in Eq. (5.1) is the mass of one sphere, which is equal to the mass of the unit cell (cf. Fig. 5.2).

The acceleration time τ is the figure of merit to be minimised. Furthermore, the reflectance and absorptance are obtained via *treams* [92] using the renormalised T-matrix defined in Eq. (2.68) and methods outlined in Section 2.3.

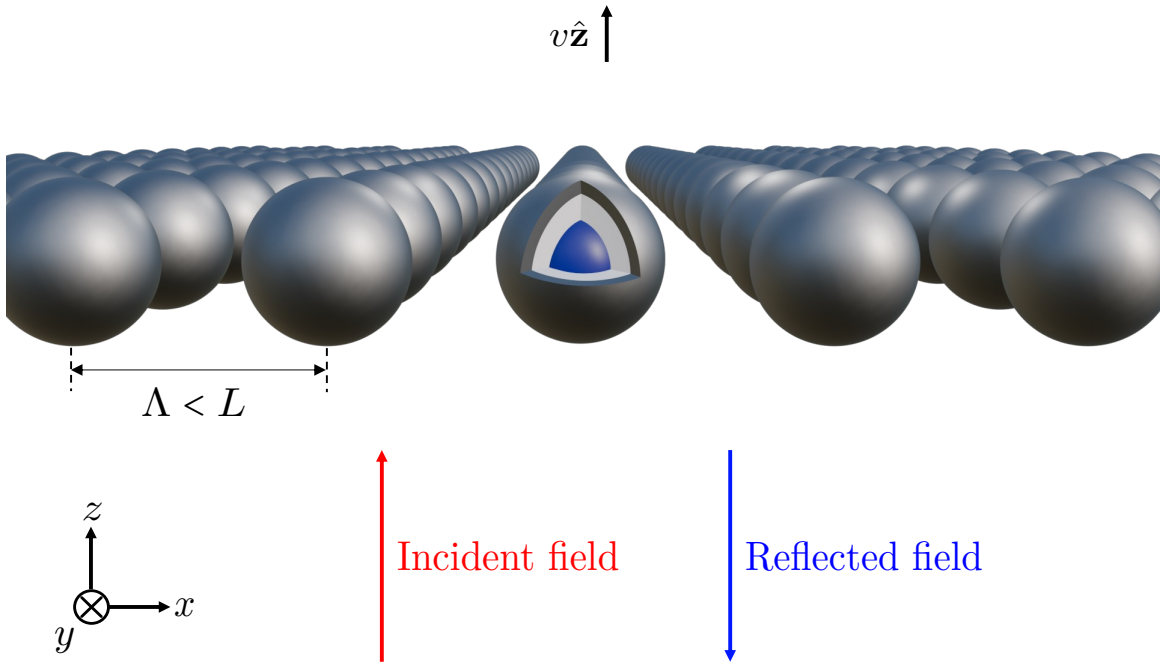

Figure 5.1: A light sail, infinitely extended in the x-y plane and travelling along the $+z$-axis at a velocity v. The sail is illuminated by an incident, linearly polarised plane wave propagating in the $+z$ direction and reflected along the $-z$ direction. The sail consists of spheres, modelled here as having a core surrounded by two concentric shells. The spheres are arranged periodically in a square lattice with a lattice constant Λ. The lattice constant is always smaller than the wavelength L of the incident wave as measured in the Earth's reference frame. Adapted from [P2] under the CC BY 4.0 license.

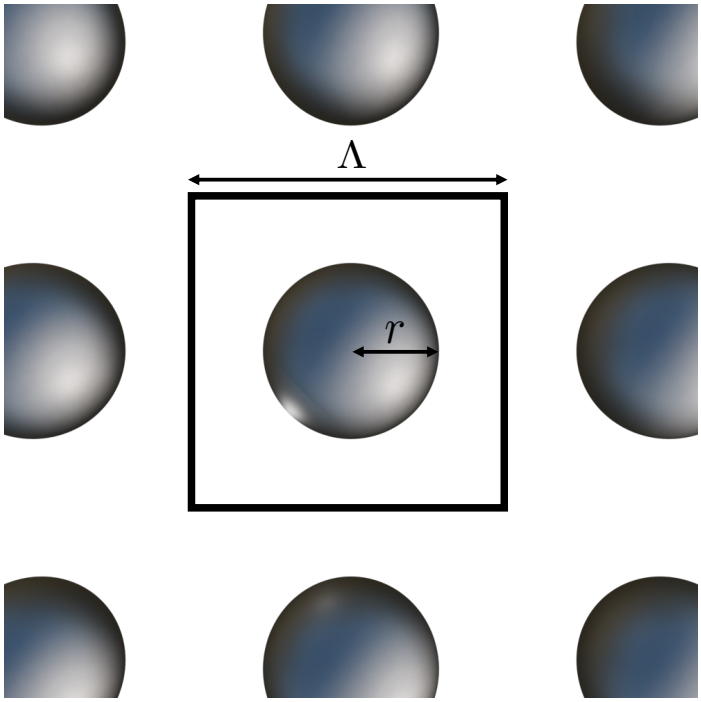

Figure 5.2: A square unit cell (black box) corresponding to light sails made of periodically arranged spheres of radius r. The associated lattice constant is denoted by Λ. For core-(multi-)shell spheres, r denotes the radius of the outermost shell.

Important to note is the dependence of the reflectance and absorptance on β. This is expected since these quantities both depend on L', which is dependent on β. Moreover, τ is not dependent on the temperature of the sail, and all material properties in Eq. (5.1) correspond to room temperature. In reality, the temperature would be different due to the coldness of outer space. However, the temperature independence of the acceleration time does not present any problems, as the methods used in this chapter could just as easily be applied with temperature-dependent quantities. Of course, one would need to re-optimise τ.

In this chapter, the methods of optimising the acceleration time are twofold. Firstly, τ is numerically minimised without any restrictions placed on the reflectance or absorptance. Secondly, τ is optimised by ensuring high reflectance and low absorptance for every β and hence L' value. There are a couple of reasons why one may want to apply the latter method. Crucially, a high reflectance would correspond to a large momentum transfer from the incident field to the sail. Also, a low absorptance would minimise any potential thermal damage to the sail. As mentioned above, τ has no dependence on the sail's temperature, providing yet another reason why the first optimisation may be unfavourable. Specifically, a numerically minimised acceleration time could be low for spheres with little mass, but the absorptance could still be very high. Consequently, an acceleration time minimised in this way could correspond to an unfavourable scenario. An example of such a configuration will be seen in Section 5.3 for a sail comprising spheres with an SiO_2 core, Si central shell and Al outer shell. For all considered light sail configurations, the acceleration time using both optimisation methods will be given.

Table 5.1: The densities of SiO_2, Si and Al [126]. Reprinted from [P2] under the CC BY 4.0 license.

Material	SiO_2	Si	Al
Density (kg m^{-2})	2196	2330	2700

In this section, the scattering setup was outlined, and all relevant parameters that optimise the acceleration time τ were defined. These parameters include the intensity of the incident light, the mass of each constituent sphere, the reflectance $R(\beta)$ and absorptance $A(\beta)$. In the following section, $R(\beta)$, $A(\beta)$ and τ will be explored for light sails comprising homogeneous spheres made from Si, SiO_2 and Al.

5.2 Light sails made from homogeneous spheres

After having outlined the system in the previous section, one can now begin to optimise the acceleration times of various light sails. In this section, light sails made up of homogeneous Si, SiO_2 and Al spheres will be examined. The consideration of these three materials is based on their inclusion in works already done relating to the BSI [62, 125]. An important quality of SiO_2 is that it is virtually non-absorbing at the considered wavelengths L', while Al is highly reflective due to it being a metal. As mentioned, a high reflectance is important to maximise momentum transfer to the sail, and a low absorptance minimises thermal damage. While Si also has a near-vanishing absorptance in the desired wavelength range, one would in reality have to be careful. A property of Si is that its absorptance is highly temperature dependent [52]. To account for this, it was suggested to add a layer of SiO_2, which has a much more temperature-resistant absorptance. The addition of SiO_2 to Si will be considered in a later section, which will serve as the most optimal structure. It should be reiterated that the purpose of this chapter is to develop a method to optimise the acceleration time of light sails, which can be applied in the same way with temperature-dependent quantities.

A favourable quality shared among all three materials is that they have low densities (cf. Table 5.1). A low density is crucial since it corresponds to a lower sail mass and a resulting higher acceleration. The reflectivity $R(\beta)$ and absorptance $A(\beta)$ values for each material were determined in accordance with Section 2.3 using *treams* [92]. For the optimisation process, $R(\beta)$ and $A(\beta)$ were discretised with respect to the lattice constant Λ, sphere radius r and speed factor β. The chosen number of values for each parameter were $N_\Lambda = 120$, $N_r = 110$ and $N_\beta = 50$, respectively. The optimisation method used was a parameter sweep over each Λ, r and β value. Due to the speed and efficiency of *treams* [92], a parameter sweep was chosen in preference to a more complicated algorithm like in the previous chapter.

An important condition is that neighbouring spheres do not touch, so the radii obey the constraint $r < \Lambda/2$. Also note that, since a conversion to the spherical basis is required to use the renormalised T-matrix, the incident field must be truncated. A truncation order of $\ell_{\max} = 4$ was considered to ensure convergence of $R(\beta)$, $A(\beta)$ and τ. In some cases, a lower value for $\ell_{\max}$ is suitable. This will be seen later for $\ell_{\max} = 2$ when considering the optimal light sails made from Si/SiO_2 core-shell spheres.

As pointed out in the previous section, two methods of optimisation will be implemented. Firstly, the numerically minimised acceleration time $\tau_{\min}$ will be determined without any prior constraints on the reflectance or absorptance. Afterwards, the acceleration time τ_{bb} corresponding to a high broadband reflectance will be obtained, where the subscript 'bb' stands for 'broadband'. To ensure a high broadband reflectance, the average reflectance $\overline{R}$ is firstly maximised, where

$$\overline{R} = \frac{1}{N_\beta} \sum_{j=1}^{N_\beta} R(\beta_j)\,. \tag{5.2}$$

By maximising $\overline{R}$, one is conveniently able to locate where the reflectance is high and absorptance is low across all wavelengths L'. It should be emphasised that the maximum average reflectance $\overline{R}_{\max}$ serves as a starting point and is not necessarily the value on which τ_{bb} should be based. This is because lattice resonances can still arise at particular wavelengths, where the reflectance suddenly becomes very low. This will be seen later when considering an embedding. When later examining the optimal Si/SiO_2 structure, however, $\overline{R}_{\max}$ can be used. This is because no lattice resonances appear in the desired wavelength range.

Colour plots of the average reflectance $\overline{R}$, average absorptance $\overline{A}$ and acceleration time τ are given in Figs (5.3) (a), (b) and (c), respectively, as a function of r/Λ and Λ for each material. The required refractive indices were taken from experimental data in Refs [127–129] available on `refractiveindex.info`. Moreover, the numerical values of the parameters used in Eq. (5.1) to determine τ were taken from Ref. [60]. These are given by $I = 10\ \mathrm{GWm}^{-2}$, $m_{\mathrm{p}} = 0.1$ g and $a = 10\ \mathrm{m}^2$. The considered ranges for r and Λ were

$$\text{Homogeneous spheres:} \quad \begin{cases} 0.01 \leq \dfrac{r}{\Lambda} \leq 0.49, & (5.3) \\ 0.01 \leq \dfrac{\Lambda}{L} \leq 0.99. & (5.4) \end{cases}$$

One should again bear in mind that the radius of each sphere must be less than half of the lattice constant to avoid neighbouring spheres touching. Moreover, the lattice constant must always be less than the wavelength L to obtain pure zeroth-order reflection.

In Fig. 5.3, it is clear that Si yields the most favourable combination of values for $\overline{R}$, $\overline{A}$ and τ. For Si, the maximum average reflectance is given by $\overline{R}_{\max} = 0.989$. This high reflectance implies a light sail made of pure Si spheres would experience a high gain in momentum, contributing to the low broadband acceleration time of $\tau_{\mathrm{bb}} = 326.7$ s. Furthermore, the corresponding average absorptance $\overline{A}$ is very low at $\overline{A} = 4.7 \times 10^{-4}$. Note that a periodic array of Si spheres was examined in Ref. [130].

Recall that the absorptance of Si is highly temperature-dependent in reality. To remedy this, it has been suggested to add a layer of SiO_2 [52, 131]. Such a configuration will be considered in the next section.

The data for each material is given in Table 5.2. One sees that light sails made from pure SiO_2 have a low maximum average reflectance of $\overline{R}_{\max} = 0.136$. The corresponding acceleration time is $\tau_{\mathrm{bb}} = 5.0 \times 10^4$ s, about $153\times$ longer than for the sail made from Si spheres. Additionally, an aluminium light sail exhibits a high maximum reflectance of $\overline{R}_{\max} = 0.810$, but also a high average absorptance of $\overline{A}_{\max} = 0.058$ due to its large extinction coefficient. Such a high absorptance may cause a pure Al light sail to fall foul to thermal damage.

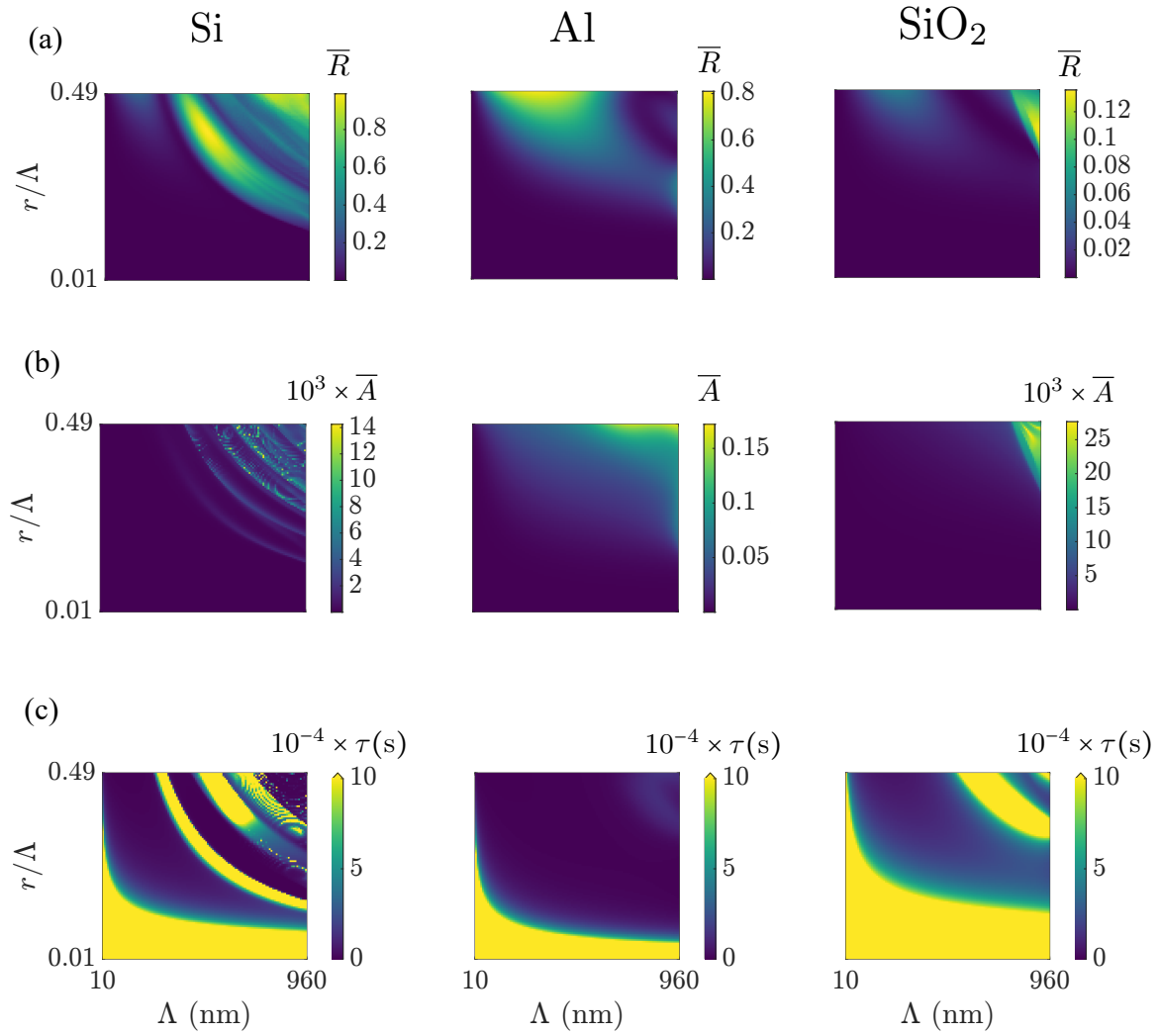

Figure 5.3: In (a), the average reflectance $\overline{R}$ is shown for lattices comprising spheres made of silicon (Si), aluminium (Al) and silicon dioxide (SiO_2) as functions of the sphere radius r and lattice constant Λ. In (b), the equivalent plots are presented for the average absorptance $\overline{A}$, whereas (c) illustrates the corresponding acceleration times τ for each lattice configuration. Reprinted from [P2] under the CC BY 4.0 license.

In this section, the reflectance, absorptance and acceleration time of light sails comprising homogeneous Si, SiO_2 and Al spheres were investigated. In the next section, the work done until now will be extended to light sails made from core-(multi-)shell spheres.

Table 5.2: The numerically minimised acceleration times $\tau_{\min}$, obtained without any prior assumptions about reflectance or absorptance, are presented alongside the values of τ_{bb}, which correspond to maximum broadband reflectance. The corresponding values for the average reflectance $\overline{R}$, average absorptance $\overline{A}$, sphere radii r and lattice constants Λ are also provided for each material. Reprinted from [P2] under the CC BY 4.0 license.

Material	r (nm)	Λ (nm)	τ (s)	$\overline{R}$	$\overline{A}$
Si	164.6	952.0	$\tau_{\min} = 212.7$	0.419	4.2×10^{-4}
	187.0	481.0	$\tau_{\mathrm{bb}} = 326.7$	0.989	4.7×10^{-4}
Al	40.1	81.8	$\tau_{\min} = 275.8$	0.480	0.031
	153.6	313.4	$\tau_{\mathrm{bb}} = 575.9$	0.810	0.058
SiO_2	106.6	217.6	$\tau_{\min} = 6.6 \times 10^3$	0.051	0.001
	368.9	960.0	$\tau_{\mathrm{bb}} = 5.0 \times 10^4$	0.136	0.020

5.3 Light sails made from core-(multi-)shell spheres

After having analysed light sails made from homogeneous spheres, one can go a step further and consider core-(multi-)shell spheres. In this section, the effects of combining the three abovementioned materials (Si, SiO_2 and Al) to create core-shell and core-double-shell spheres are explored. As a result, extra degrees of freedom are introduced in the form of the radius (radii) of the added shell(s). For a core-shell system, each sphere has a core radius r_1 and shell radius r_2, both of which are measured from the centre of the core. The same applies for core-double-shell spheres but with an additional radius r_3. A core-shell and core-double-shell sphere are depicted in Fig. 5.4.

With additional radii come additional constraints. Of course, an inner radius must be smaller than an outer radius. Accordingly, the radii satisfy the inequalities

$$\text{Core-shell:} \quad \begin{cases} 0.01 \leq \dfrac{r_2}{\Lambda} \leq 0.49\,, & (5.5) \\ 0.01 \leq \dfrac{r_1}{r_2} \leq 0.99\,, & (5.6) \end{cases}$$

$$\text{Core-double-shell:} \quad \begin{cases} 0.01 \leq \dfrac{r_3}{\Lambda} \leq 0.49\,, & (5.7) \\ 0.01 \leq \dfrac{r_2}{r_3} \leq 0.99\,, & (5.8) \\ 0.01 \leq \dfrac{r_1}{r_2} \leq 0.99\,, & (5.9) \end{cases}$$

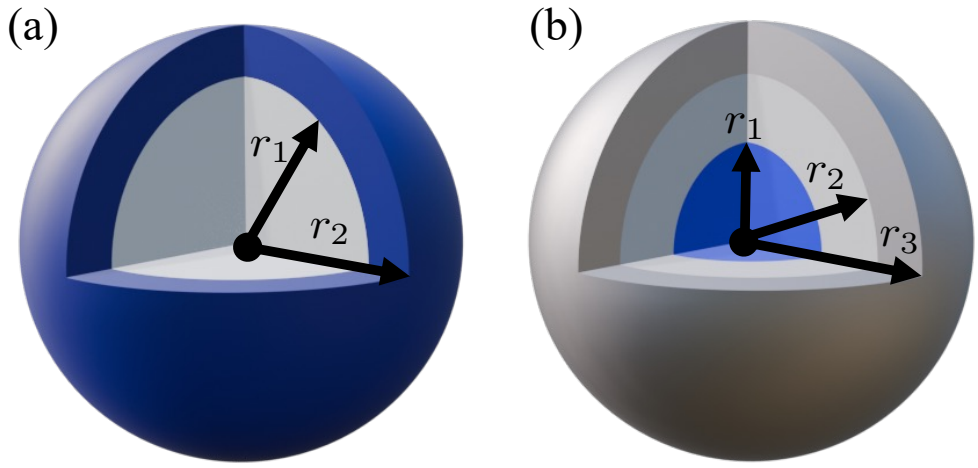

Figure 5.4: A schematic of (a) a constituent core-shell sphere characterised by inner and outer radii r_1 and r_2, respectively. In (b), a similar representation is provided for a core-double-shell sphere, defined by inner, central and outer radii r_1, r_2 and r_3, respectively. Reprinted from [P2] under the CC BY 4.0 license.

where inequalities (5.5) and (5.7) ensure separation of neighbouring spheres. Moreover, the sub-wavelength constraint on the lattice constant Λ still applies, where $\Lambda < L$.

The same optimisation procedure used in the previous section was applied to the core-(multi-)shell light sails. As a reminder, the average reflectance $\overline{R}$ is first maximised as a reference to determine material parameters that lead to high broadband reflectance and low broadband absorptance. The corresponding broadband acceleration time τ_{bb} is then determined, along with the numerically minimised acceleration time τ_{min}. The data for $\overline{R}$, $\overline{A}$, τ_{bb} and τ_{min} is given in Table 5.3 for five combinations of some or all of the considered materials. The highlight is the Si/SiO_2 combination, which exhibits a maximum average reflectance $\overline{R}_{\mathrm{max}} = 0.988$, corresponding average absorptance $\overline{A} = 9.2 \times 10^{-4}$ and broadband acceleration time $\tau_{\mathrm{bb}} = 395.3$. The low τ_{bb} value is also attributed to the low densities of Si and SiO_2 (cf. Table 5.1) and consequent low masses. Compared to the light sail made from pure Si considered in the previous section, the broadband acceleration time of the Si/SiO_2 sail is only 68.6 s slower. The high performance of the Si/SiO_2 structure serves as a prime example of how two dielectrics with distinct permittivities can be combined to yield a higher reflectance than a metal. Such a scenario has also been observed in works relating to Bragg reflectors [65–70].

For the Si/SiO_2 light sail, $\overline{R}$, $\overline{A}$ and τ are plotted with respect to r_1/r_2 and Λ/r_2 in Figs 5.5 (a), (b) and (c), respectively, where the outer radius is fixed at the optimised value $r_2 = 204.3$ nm. A red cross marks the location of the radii and lattice constant given in Table 5.3 that produce the optimised broadband acceleration time $\tau_{\mathrm{bb}} = 395.3$ s. In Fig. 5.5 (d), the spectra for R and A are shown that produce the optimised broadband acceleration time. The region of interest is marked in white, while data relating to other wavelengths are marked in grey.

In other works, the acceleration distance d was considered instead of the acceleration time τ [60, 132–134]. Choosing between these two figures of merit is a matter of preference, but can be nicely linked for the Si/SiO_2 light sail. Since the reflectance is almost perfect,

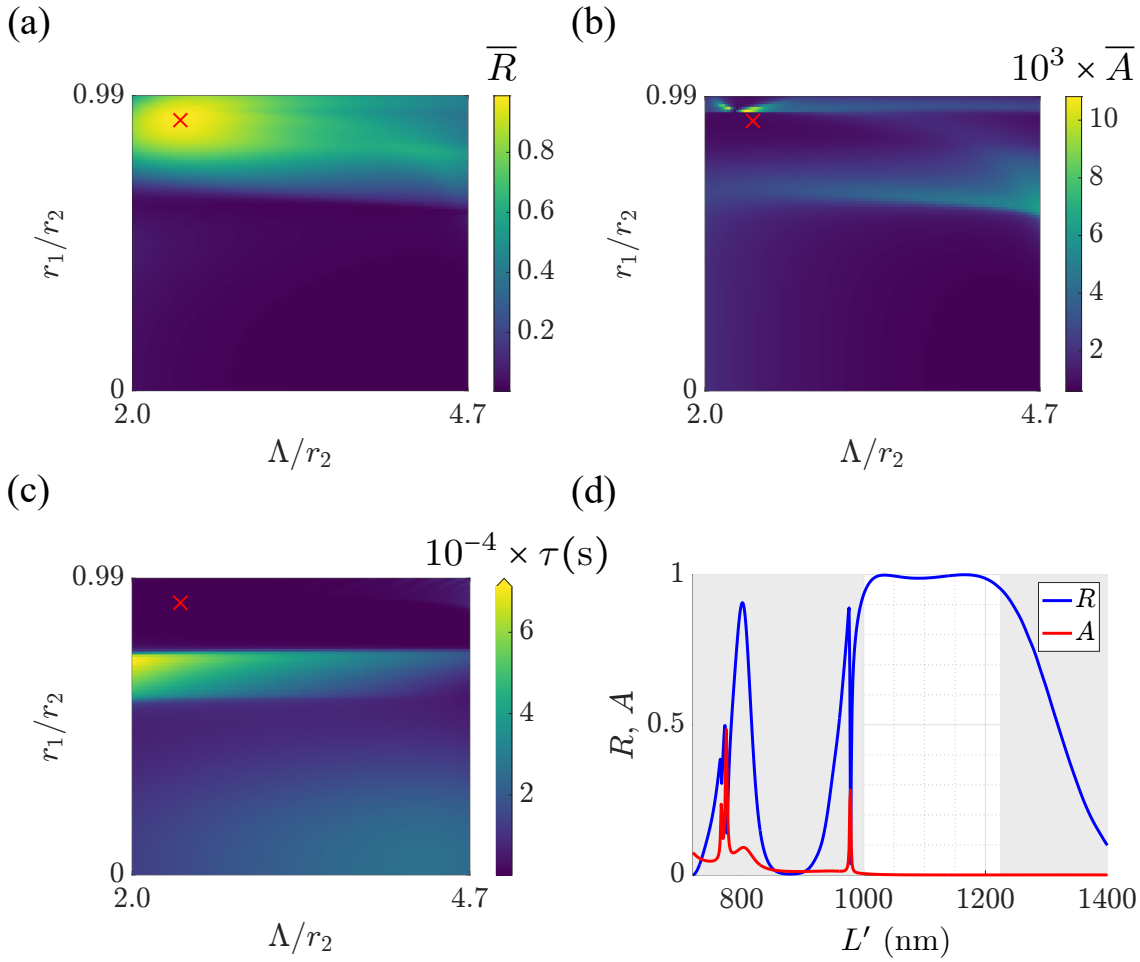

Figure 5.5: In (a), (b) and (c), the plots depict the average reflectance $\overline{R}$, average absorptance $\overline{A}$ and acceleration time τ, respectively, as functions of r_1/r_2 and Λ/r_2, where $r_2 = 204.3$ nm for a light sail composed of Si/SiO_2 spheres. The red cross in all three plots marks the position of the maximum average reflectance $\overline{R}_{\mathrm{max}} = 0.988$, $\overline{A} = 9.2 \times 10^{-4}$ and $\tau_{\mathrm{bb}} = 395.3$ s, as listed in Table 5.3. Tile (d) shows the reflectance $\overline{R}$ and absorptance $\overline{A}$ corresponding to $\overline{R}_{\mathrm{max}}$. The region of interest $L' \in [1.0L, 1.225L]$ is highlighted between the two grey areas. Adapted from [P2] under the CC BY 4.0 license.

Table 5.3: The numerically minimised acceleration times τ_{min} and those corresponding to maximum broadband reflectance (τ_{bb}), alongside the average reflectance $\overline{R}$, average absorptance $\overline{A}$, radii r_1, r_2 and r_3 (for spheres with two shells) and lattice constants Λ. These results are presented for lattices of spheres comprising Si and SiO_2, as well as for four combinations containing some or all of the materials Al, Si and SiO_2. Reprinted from [P2] under the CC BY 4.0 license.

Materials	r_1 (nm)	r_2 (nm)	r_3 (nm)	Λ (nm)	τ (s)	$\overline{R}$	$\overline{A}$
Si/SiO_2	163.6	172.1	–	941.4	$\tau_{\mathrm{min}} = 211.9$	0.455	9.6×10^{-4}
	186.2	204.3	–	494.3	$\tau_{\mathrm{bb}} = 395.3$	0.988	9.2×10^{-4}
$SiO_2/Si/SiO_2$	122.8	176.4	253.4	941.4	$\tau_{\mathrm{min}} = 400.5$	0.575	0.005
	147.4	206.0	287.9	587.5	$\tau_{\mathrm{bb}} = 791.4$	0.938	0.005
$Al/SiO_2/Si$	89.3	132.1	195.3	922.7	$\tau_{\mathrm{min}} = 213.8$	0.494	0.120
	4.1	27.6	187.4	475.7	$\tau_{\mathrm{bb}} = 335.8$	0.991	4.4×10^{-4}
$Si/Al/SiO_2$	11.7	12.8	14.0	28.6	$\tau_{\mathrm{min}} = 210.1$	0.077	0.329
	200.2	202.2	204.3	494.3	$\tau_{\mathrm{bb}} = 435.0$	0.848	0.131
$SiO_2/Si/Al$	12.4	13.1	13.8	28.6	$\tau_{\mathrm{min}} = 102.2$	0.224	0.449
	0.02	1.5	150.9	308.0	$\tau_{\mathrm{bb}} = 566.6$	0.810	0.057

and a constant incident field intensity I is assumed, one can use the fact that the force on an approximately perfect reflector is almost constant [95, Eq. (9.64)]. As a result, the corresponding acceleration is also almost constant. The broadband acceleration distance d_{bb}, therefore, is simply the area under a triangular speed-time graph (cf. Fig. 5.6). Explicitly, d_{bb} is given by

$$\begin{aligned} d_{\mathrm{bb}} &\approx \frac{1}{2} v_{\mathrm{f}} \tau_{\mathrm{bb}} \\ &= 5.9 \times 10^{10}\ \mathrm{m}. \end{aligned} \tag{5.10}$$

An example of a light sail with a low acceleration time τ_{min} but low average reflectance and high average absorptance obtained upon numerical minimisation is that made from $SiO_2/Si/Al$ spheres. For this combination, $\tau_{\mathrm{min}} = 102.2$ s with corresponding values of $\overline{R} = 0.224$ and $\overline{A} = 0.449$. In reality, such a low reflectance may not transfer enough momentum to the sail, and such a high absorptance could lead to thermal damage. The $SiO_2/Si/Al$ light sail therefore serves as a good example of why one may wish to first ensure a high broadband reflectance and low broadband absorptance. The low τ_{min} value for the $SiO_2/Si/Al$ light sail is attributed to the small total radius of each sphere ($r_3 = 13.8$ nm). Correspondingly, the mass of each sphere is small, thus leading to a faster acceleration. Interestingly, the maximum average reflectance $\overline{R}_{\mathrm{max}} = 0.810$ for the $SiO_2/Si/Al$ combination is the same as that for a light sail made from homogeneous Al spheres. Moreover, the radii of the SiO_2 core and Si inner shell are virtually negligible, implying they are ineffective and shielded by the outer Al layer.

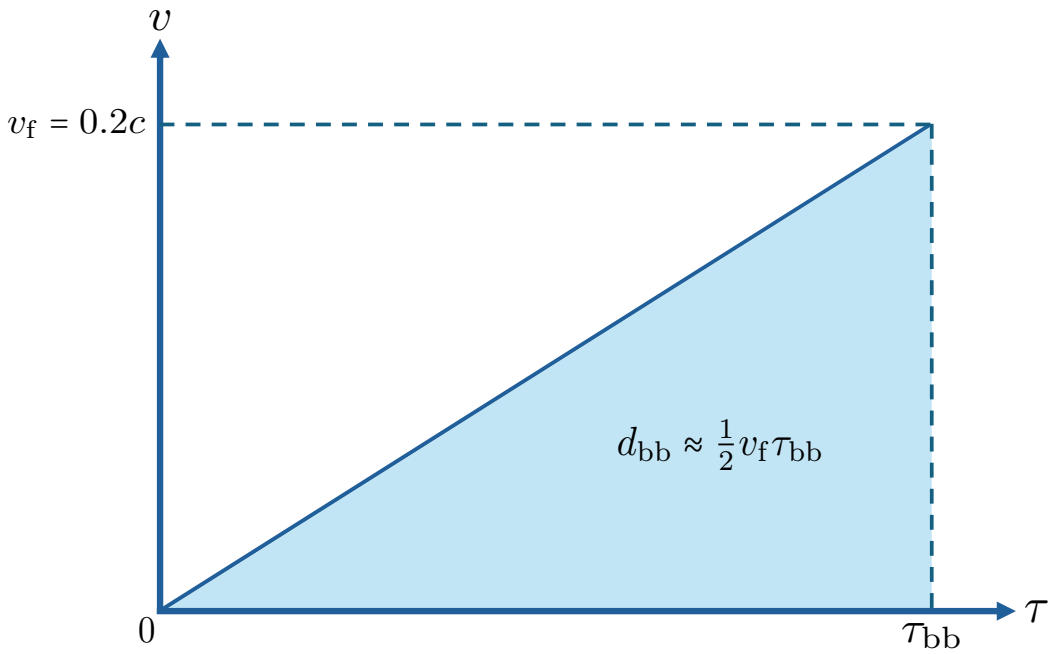

Figure 5.6: A speed time graph for a light sail moving with constant acceleration to a target speed of $v_\mathrm{f} = 0.2c$ in time $\tau = \tau_\mathrm{bb}$. The blue triangle is the area under the graph in the interval $\tau \in [0, \tau_\mathrm{bb}]$. This area represents the broadband acceleration distance d_bb.

In summary, the reflectance, absorptance and acceleration time of light sails made from core-(multi-)shell spheres were determined and optimised. A promising Si/SiO_2 core-shell configuration was found, which exhibits high broadband reflectance, low broadband absorptance and a low corresponding acceleration time. In the next section, the high reflectance of the Si/SiO_2 light sail will be explained by considering the multipolar contributions of the outgoing field.

5.4 Analysing the high broadband reflectance of a core-shell Si/SiO_2 light sail

To see why a light sail made of Si/SiO_2 core-shell spheres yields a high broadband reflectance, one can examine the effects of lattice interactions on the Mie coefficients linking the incoming and outgoing fields. Just like how a single sphere can be described by Mie coefficients, one can extend this to a lattice comprising of spheres by defining effective Mie coefficients [135]. Upon determining the effective Mie coefficients, one gains clarity on the effects of lattice interactions.

As previously mentioned, only a zeroth diffraction order exists. In other words, the incident wavelength of the light is always greater than the lattice spacing. Moreover, coefficients up to quadrupolar order are considered as the relevant data converges with this approximation. This section therefore provides an extension to work done in Ref. [130], where only the dipolar order was considered.

The relevant effective Mie coefficients up to quadrupolar order are given by [135, Eqs (19a-19d)]

$$\frac{1}{a_{1,\text{eff}}} = \frac{1 + C_{\text{dQ}}^2 a_{1,\text{mod}} b_{2,\text{mod}}}{a_{1,\text{mod}}(1 + \text{i}\sqrt{5/3} C_{\text{dQ}} b_{2,\text{mod}})} \tag{5.11}$$

$$\frac{1}{b_{1,\text{eff}}} = \frac{1 + C_{\text{dQ}}^2 b_{1,\text{mod}} a_{2,\text{mod}}}{b_{1,\text{mod}}(1 + \text{i}\sqrt{5/3} C_{\text{dQ}} a_{2,\text{mod}})} \tag{5.12}$$

$$\frac{1}{a_{2,\text{eff}}} = \frac{1 + C_{\text{dQ}}^2 b_{1,\text{mod}} a_{2,\text{mod}}}{a_{2,\text{mod}}(1 + \text{i}\sqrt{3/5} C_{\text{dQ}} b_{1,\text{mod}})} \tag{5.13}$$

$$\frac{1}{b_{2,\text{eff}}} = \frac{1 + C_{\text{dQ}}^2 a_{1,\text{mod}} b_{2,\text{mod}}}{b_{2,\text{mod}}(1 + \text{i}\sqrt{3/5} C_{\text{dQ}} a_{1,\text{mod}})}\,, \tag{5.14}$$

where [135, Eqs (20a-20b)]

$$\frac{1}{a_{1,\text{mod}}} = -\left(\frac{1}{a_1} + \text{i} C_{\text{dd}}\right) \tag{5.15}$$

$$\frac{1}{b_{1,\text{mod}}} = -\left(\frac{1}{b_1} + \text{i} C_{\text{dd}}\right) \tag{5.16}$$

$$\frac{1}{a_{2,\text{mod}}} = -\left(\frac{1}{a_2} + \text{i} C_{\text{QQ}}\right) \tag{5.17}$$

$$\frac{1}{b_{2,\text{mod}}} = -\left(\frac{1}{b_2} + \text{i} C_{\text{QQ}}\right) \tag{5.18}$$

are the modified Mie coefficients and $C_{\text{dd}}, C_{\text{QQ}}$ and C_{dQ} are the Cartesian dipole-dipole, quadrupole-quadrupole and dipole-quadrupole coupling coefficients, respectively. Note that Eqs. (5.15-5.18) differ from the original equations (20a-20b) in [135] by a minus sign in front of the spherical Mie coefficients a_1, b_1, a_2 and b_2. This is due to Ref. [135] and *treams* [92] using different conventions. Since *treams* [92] is implemented in this thesis, its convention is used.

The coupling coefficients can be determined by transforming the 16×16 spherical coupling matrix $\mathbf{C}_\text{s}$ present in Eq. (2.68) to the Cartesian basis using the transformation

$$\mathbf{C} = \text{i}\mathbf{F}_\ell \mathbf{C}_\text{s} \mathbf{F}_\ell^{-1}, \quad \ell \in \{1, 2\}\,, \tag{5.19}$$

where $\mathbf{C}$ is the 16×16 Cartesian coupling matrix and $\mathbf{F}_\ell$ are transformation matrices given by [135]

$$\mathbf{F}_1 = \frac{1}{\sqrt{2}} \begin{pmatrix} 1 & 0 & -1 \\ -\text{i} & 0 & -\text{i} \\ 0 & \sqrt{2} & 0 \end{pmatrix} \tag{5.20}$$

and

$$\mathbf{F}_2 = \frac{1}{\sqrt{2}} \begin{pmatrix} -\text{i} & 0 & 0 & 0 & \text{i} \\ 0 & -\text{i} & 0 & -\text{i} & 0 \\ 0 & 0 & \sqrt{2} & 0 & 0 \\ 0 & 1 & 0 & -1 & 0 \\ 1 & 0 & 0 & 0 & 1 \end{pmatrix}. \tag{5.21}$$

In Fig. 5.7, it is demonstrated how $\mathbf{F}_1$ and $\mathbf{F}_2$ are implemented. The locations of C_{dd}, C_{dQ} and C_{QQ} in $\mathbf{C}$ are shown in Fig. 5.8.

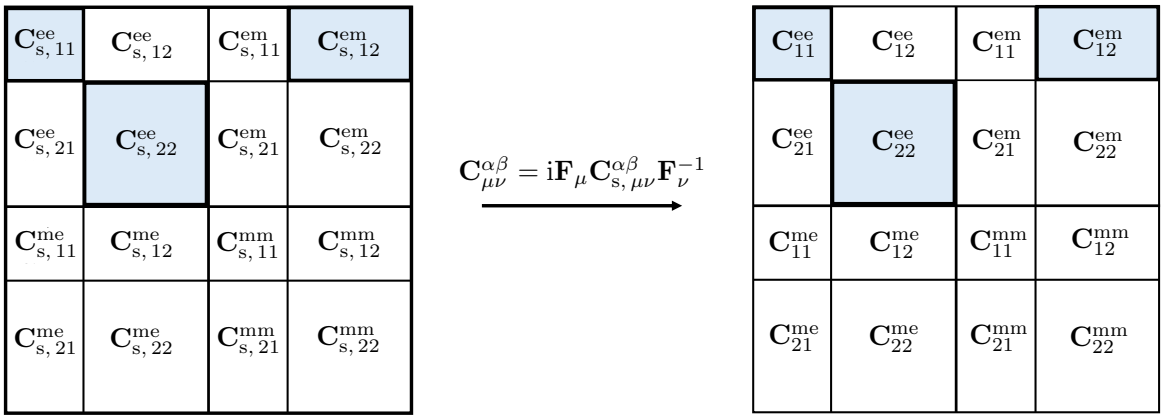

Figure 5.7: A diagram showing the transformation of the spherical coupling matrix $\mathbf{C}_{\mathrm{s}}$ (left) to the Cartesian coupling matrix $\mathbf{C}$ (right) via the matrices $\mathbf{F}_1$ and $\mathbf{F}_2$ defined in Eqs. (5.20) and (5.21), respectively. Both matrices are of quadrupolar order and contain 16×16 elements. Highlighted in blue are the matrix blocks important for this chapter, from which one obtains the coupling coefficients C_{dd}, C_{QQ} and C_{dQ}.

The effects of lattice interactions are visible upon consideration of the transmission $\mathscr{T}$, where [135, Eq. (23a)]

$$\mathscr{T} = 1 - (3\widetilde{a_{1,\mathrm{eff}}} + 3\widetilde{b_{1,\mathrm{eff}}} + 5\widetilde{a_{2,\mathrm{eff}}} + 5\widetilde{b_{2,\mathrm{eff}}})\,, \tag{5.22}$$

and $\widetilde{a_{1,\mathrm{eff}}}$, $\widetilde{b_{1,\mathrm{eff}}}$, $\widetilde{a_{2,\mathrm{eff}}}$ and $\widetilde{b_{2,\mathrm{eff}}}$ are the normalised effective electric dipole, magnetic dipole, electric quadrupole and magnetic quadrupole Mie coefficients, respectively. The normalisation is with respect to the normalised lattice constant $\widetilde{\Lambda} = \Lambda/L'$, where

$$\widetilde{a_{1,\mathrm{eff}}} = \frac{a_{1,\mathrm{eff}}}{4\pi\widetilde{\Lambda}^2}, \quad \text{etc.} \tag{5.23}$$

For brevity, Eq. (5.22) can be rewritten as

$$\mathscr{T} = 1 - \widetilde{\Sigma}\,, \tag{5.24}$$

where

$$\widetilde{\Sigma} = 3\widetilde{a_{1,\mathrm{eff}}} + 3\widetilde{b_{1,\mathrm{eff}}} + 5\widetilde{a_{2,\mathrm{eff}}} + 5\widetilde{b_{2,\mathrm{eff}}}\,. \tag{5.25}$$

From the previous equation, one can now appreciate the usefulness of considering the transmission $\mathscr{T}$. Since the absorptance of the Si/SiO_2 light sail is almost vanishing, one sees that a perfect broadband reflectance corresponds to $\widetilde{\Sigma} = 1$. By seeing how close $\widetilde{\Sigma}$ is to 1, one can readily observe how the effective Mie coefficients combine to produce a high broadband reflectance. The dispersion of each effective Mie coefficient and how they sum together is depicted in Fig. 5.9. In Figs 5.9 (a) and (b), the real and imaginary components of the effective Mie coefficients are plotted with their corresponding prefactors. The analogous plots for $\widetilde{\Sigma}$

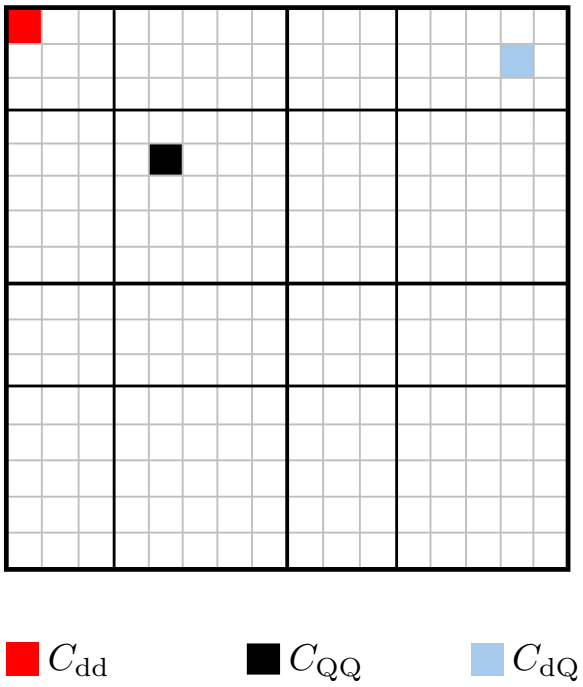

Figure 5.8: The locations of the coupling coefficients C_{dd}, C_{QQ} and C_{dQ} in the Cartesian coupling matrix $\mathbf{C}$.

are given in Fig. 5.9 (c), where the intersecting red lines show the points of maximum reflectance. The corresponding reflectance $R = |\mathscr{R}|^2$ and transmittance $T = |\mathscr{T}|^2 = 1 - R - A$ spectra are given in Fig. 5.9 (d), where the vertical red lines mark the points of maximum reflectance.

Note that the transmission $\mathscr{T}$ was considered instead of the reflection $\mathscr{R}$ [135, Eq. (23b)]

$$\mathscr{R} = 3\widetilde{a_{1,\mathrm{eff}}} - 3\widetilde{b_{1,\mathrm{eff}}} - 5\widetilde{a_{2,\mathrm{eff}}} + 5\widetilde{b_{2,\mathrm{eff}}}. \tag{5.26}$$

In Eq. (5.26), one sees that many combinations of the real and imaginary parts of $\mathscr{R}$ could yield a perfect reflectance $R = |\mathscr{R}|^2 = 1$. For $\mathscr{T}$, however, one requires strictly that $\mathrm{Re}(\widetilde{\Sigma}) = 1$. Considering the transmission, therefore, allows one to better distinguish the necessary relationship between the real and imaginary parts of the effective Mie coefficients.

For comparison, the analogous plots to those in Figs 5.9 (a), (b) are given in Figs 5.10 (a) and (b) for the Mie coefficients $\widetilde{a_1}, \widetilde{b_1}, \widetilde{a_2}$ and $\widetilde{b_2}$ of a single sphere. Moreover, the plot for $\widetilde{\Sigma}_{\mathrm{S}}$ is given in Fig. 5.10 (c), where $\widetilde{\Sigma}_{\mathrm{S}}$ is the single-sphere version of $\widetilde{\Sigma}$. Note that the 'S' subscript stands for 'sphere', and the same normalisation factor $4\pi\widetilde{\Lambda}^2$ as before was used for consistency. One sees that the lattice interactions greatly change the spectra compared to a single sphere. Specifically, coupling between different multipolar responses is introduced through the C_{dQ} term in Eqs (5.11)-(5.14) describing the effective Mie coefficients.

In this section, the dispersion of the multipoles describing the outgoing field was examined. Moreover, the multipolar interactions for an Si/SiO$_2$ light sail were compared to those of a single sphere. In doing this, a high broadband reflectance arising from an Si/SiO$_2$ light sail was explained with reference to lattice interactions and the resulting coupling of differ-

ent multipole moments. In the following section, the effects of adding an embedding to the Si/SiO_2 light sail will be discussed.

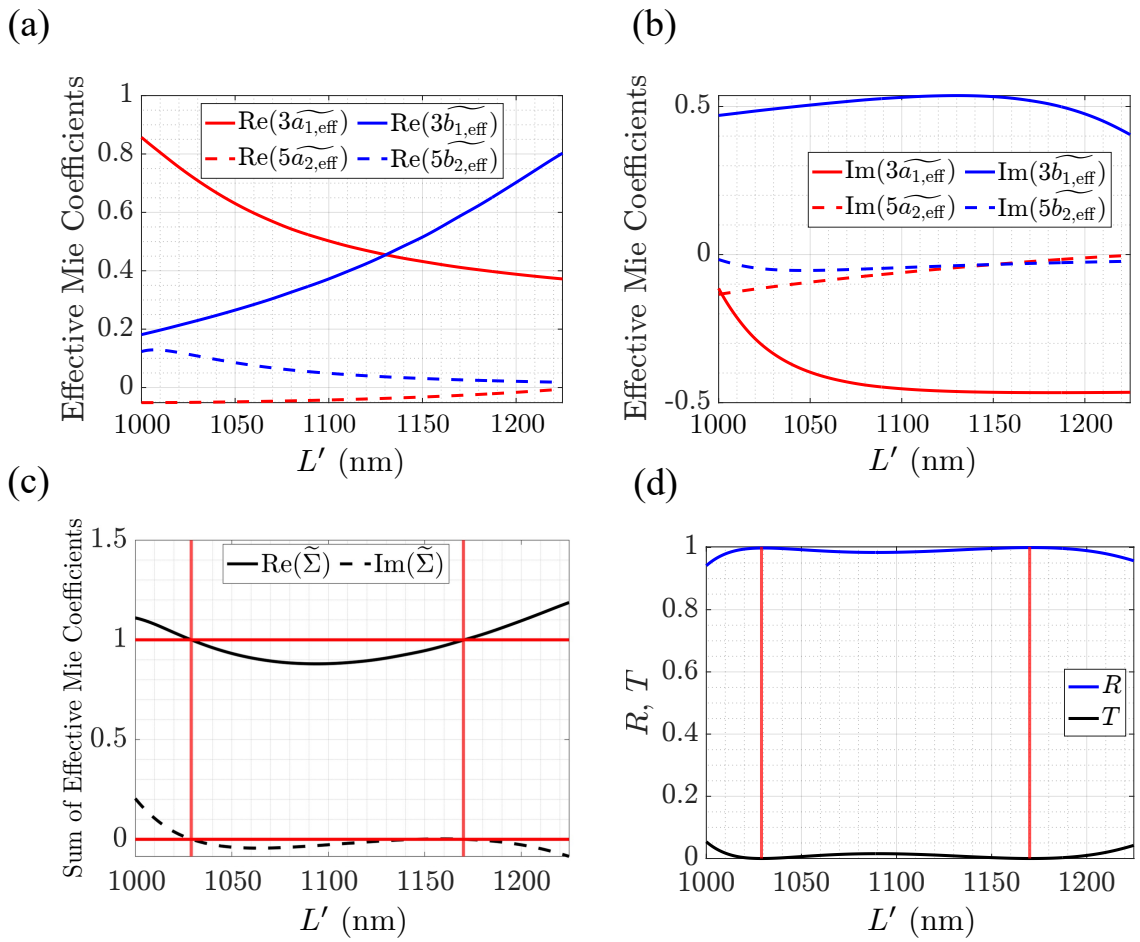

Figure 5.9: Tiles (a) and (b) illustrate the real and imaginary parts of the normalised effective Mie coefficients up to quadrupolar order, incorporating the prefactors described in Eq. (5.25), as functions of the Doppler-shifted wavelength L'. Tile (c) displays the summed contributions of the coefficients from (a) and (b), with red vertical and horizontal lines marking the intersection points that correspond to the multipole combinations yielding maximum reflectance. Tile (d) presents the reflectance R and transmittance T spectra, with red vertical lines indicating the wavelengths associated with maximum reflectance. Adapted from [P2] under the CC BY 4.0 license.

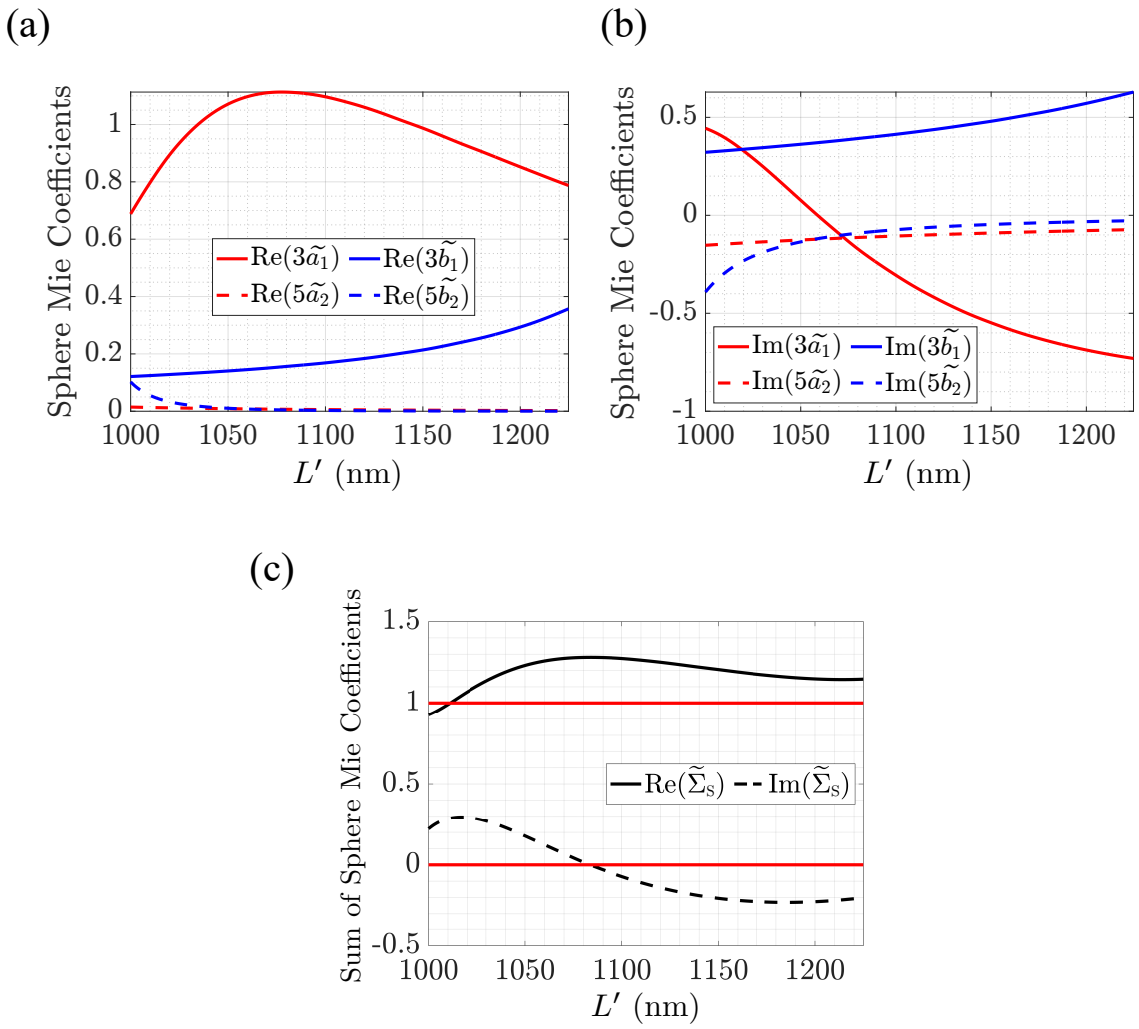

Figure 5.10: Similar plots to those shown in Figs. 5.9 (a), (b) and (c) are provided for an individual sphere. In (c), the subscript 'S' stands for 'sphere'. Adapted from [P2] under the CC BY 4.0 license.

5.5 The effects of an embedding surrounding the Si/SiO$_2$ lattice

Up until now, the light sails were square lattices containing spheres suspended in a vacuum. This was done to examine purely the effects of lattice interactions on the reflectance, absorptance and acceleration time. In reality, a light sail would need structural support. By leveraging the capabilities of *treams* [92], one can add an embedding (cf. Fig. 5.11 (a), where the embedding has a thickness of $d_{\mathrm{emb}} = 3r_2$). At the same time, one is still able to use the methods described in this chapter. Considering again the Si/SiO$_2$ configuration, one can observe the effects of embeddings with varying refractive indices n_{emb} on the reflectance R. In doing this, one finds that the embedding can have a refractive index up to $n_{\mathrm{emb}} \approx 1.13$ before the average reflectance drops below 90% (cf. Fig. 5.11). To apply an embedding with a higher refractive index, a re-optimisation of the light sail would be required. Of course, one would also have to be careful that the embedding is not too dense. A high density would correspond to a high mass, thus increasing acceleration time (cf. Eq. (5.1)). Specifically, Eq. (5.1) for the acceleration time τ would acquire an extra term representing the mass m_{emb} of the unit cell embedding, where

$$m_{\mathrm{emb}} = \rho_{\mathrm{emb}}(d_{\mathrm{emb}}\Lambda^2 - V_{\mathrm{S}})\,. \tag{5.27}$$

In the above equation, $V_{\mathrm{S}} = \sum_j^{j_{\max}} V_j$ is the total volume of the sphere occupying the unit cell embedding. Accordingly, the modified acceleration time τ_{emb} is given by

$$\tau_{\mathrm{emb}} = \frac{c^2}{I\Lambda^2}\int_0^{\beta_{\mathrm{f}}} \frac{\mu_{\mathrm{p}} + \sum_j^{j_{\max}} \rho_j V_j + m_{\mathrm{emb}}}{A(\beta) + 2R(\beta)} \frac{\gamma^3(1+\beta)}{(1-\beta)} \mathrm{d}\beta\,. \tag{5.28}$$

As considered in Refs [130, 136], an example of a light embedding would be polydimethylsiloxane (PDMS). PDMS has a refractive index of $n_{\mathrm{PDMS}} = 1.45$ and very low density $\rho_{\mathrm{PDMS}} = 965\,\mathrm{kgm}^{-3}$. For an Si/SiO$_2$ light sail with a PDMS embedding, the analogous plots to those in Fig. 5.5 are given in Fig. 5.12, this time with $r_2 = 221.8$ nm. In Fig. 5.12 (d), it is clear why using the maximum average reflectance to optimise the acceleration time is a starting point as opposed to the only value one should consider. Specifically, a lattice resonance appears at $L' = 1158$ nm, where the reflectance drops to $R = 0.21$. Such a low reflectance, albeit in a very narrow spectral region, may not be conducive to an efficient acceleration. With the lattice resonance, the broadband acceleration time is $\tau_{\mathrm{bb}} = 1.0 \times 10^3$ s. However, one can adjust the parameters corresponding to the maximum average reflectance to shift the resonance outside of the desired wavelength range. This shift can be accomplished by decreasing the outer radius r_2. An example of data corresponding to $r_2 = 180.8$ nm and an average reflectance of $\overline{R} = 0.887$ without resonances in the desired wavelength range is given in Fig. 5.13. Here, the acceleration time has a value of $\tau = 867.1$ s. This is 471.8 s slower than τ_{bb} for the Si/SiO$_2$ sail without an embedding (cf. Table 5.3). Note that the red cross in Figs 5.13 (a)-(c) now corresponds to $\overline{R} = 0.887$ as opposed to the maximum average reflectance.

In this section, the effects of adding an embedding to an Si/SiO$_2$ light sail were discussed. Furthermore, an example PDMS polymer embedding was examined, which introduced a lattice resonance in the reflectance spectrum. To circumvent this, the radii of the constituent spheres were reduced to move the resonance outside the desired wavelength range.

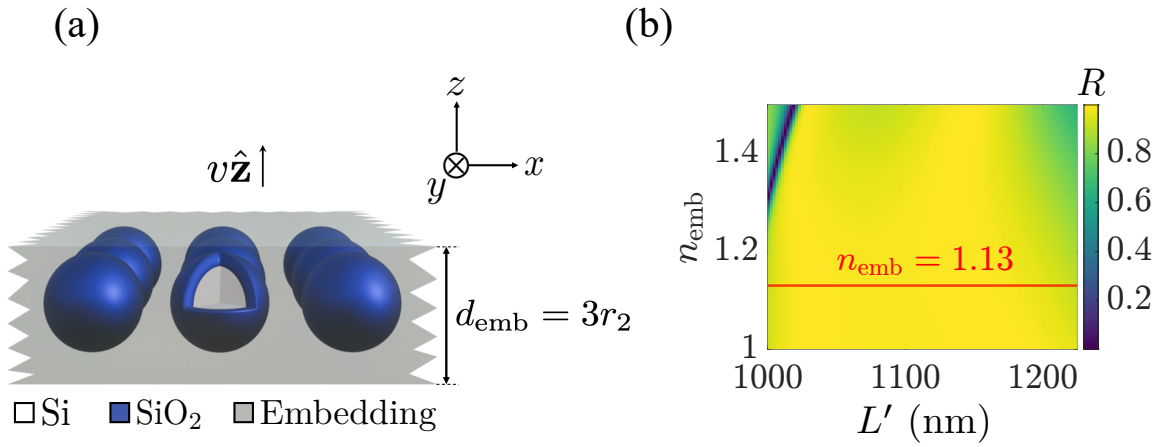

Figure 5.11: Tile (a) illustrates a schematic of a core-shell Si/SiO_2 spherical array travelling at speed v along the $+z$-axis, embedded within a medium of thickness $d_{\text{emb}} = 3r_2$, where r_2 is the radius of each outer shell. In (b), the colour map depicts the reflectance R for the optimised Si/SiO_2 array as a function of the refractive index of the embedding medium n_{emb} and the Doppler-shifted wavelength L'. The red horizontal line indicates the refractive index threshold $n_{\text{emb}} = 1.13$, above which the minimum reflectance falls below 90%. Adapted from [P2] under the CC BY 4.0 license

5.6 Summary

In this chapter, the reflectance R, absorptance A and acceleration time τ of various light sails were explored. The acceleration time is the time required for the sail to reach its final speed $v_{\text{f}} = 0.2c$. The light sails comprised periodically arranged spheres in a square lattice moving in the z-direction at speed v. The incident field was a linearly polarised plane wave and met the light sails at normal incidence. The aim was to observe the effects of relativistic motion on R, A and τ, with the final goal of optimising the acceleration time τ. To begin, the constituent spheres were homogeneous and made from either silicon (Si), silicon dioxide (SiO_2) or aluminium (Al). These three materials are favourable due to their low densities, another aspect that reduces the acceleration time. After analysing each material separately, they were combined to form core-(multi-)shell spheres. A promising combination of an Si core and SiO_2 outer shell was found, which gave rise to a high broadband reflection and low broadband absorptance over the Doppler-shifted wavelengths observed by the sail. A high reflectance allows for high momentum transfer to the sail, while a low absorptance minimises thermal damage. Subsequently, the high broadband reflectance of the Si/SiO_2 sail was explained by examining the relationships between each multipolar contribution of the outgoing field up to quadrupolar order. Finally, the effects of adding an embedding to the Si/SiO_2 sail were investigated. It was emphasised that one should be careful of lattice resonances and shown how they can be avoided.

In the next chapter, more complex, non-symmetric structures will be examined, where the influence of relativistic effects on the circular dichroism of chiral biomolecules will be investigated.

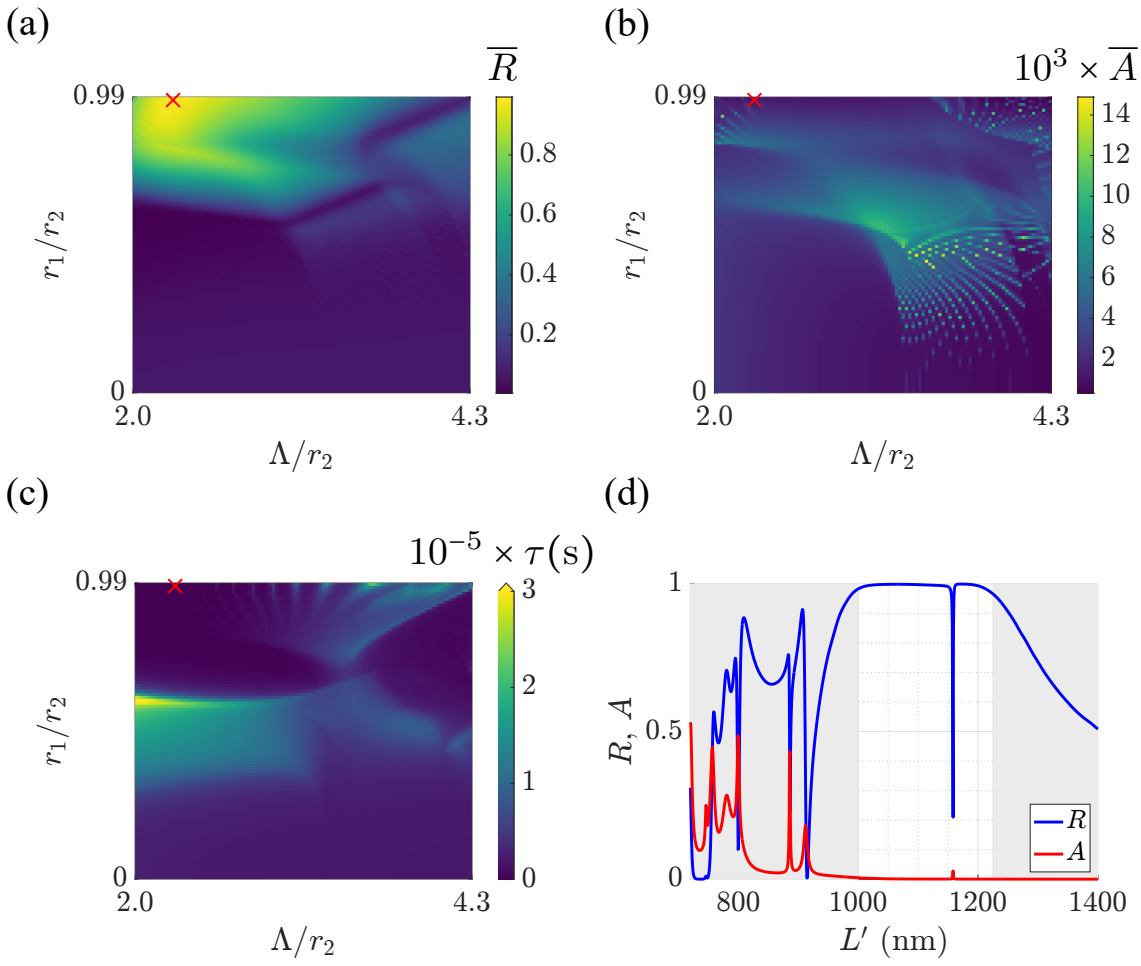

Figure 5.12: The analogous plots to those in Fig. 5.5 for an Si/SiO_2 light sail with a polydimethylsiloxane (PDMS) embedding. In tile (d), the reflectance suddenly drops to $R = 0.21$ at $L' = 1158$ nm owing to a lattice resonance. This time, the radius of each outer shell is $r_2 = 221.8$ nm. Adapted from [P2] under the CC BY 4.0 license.

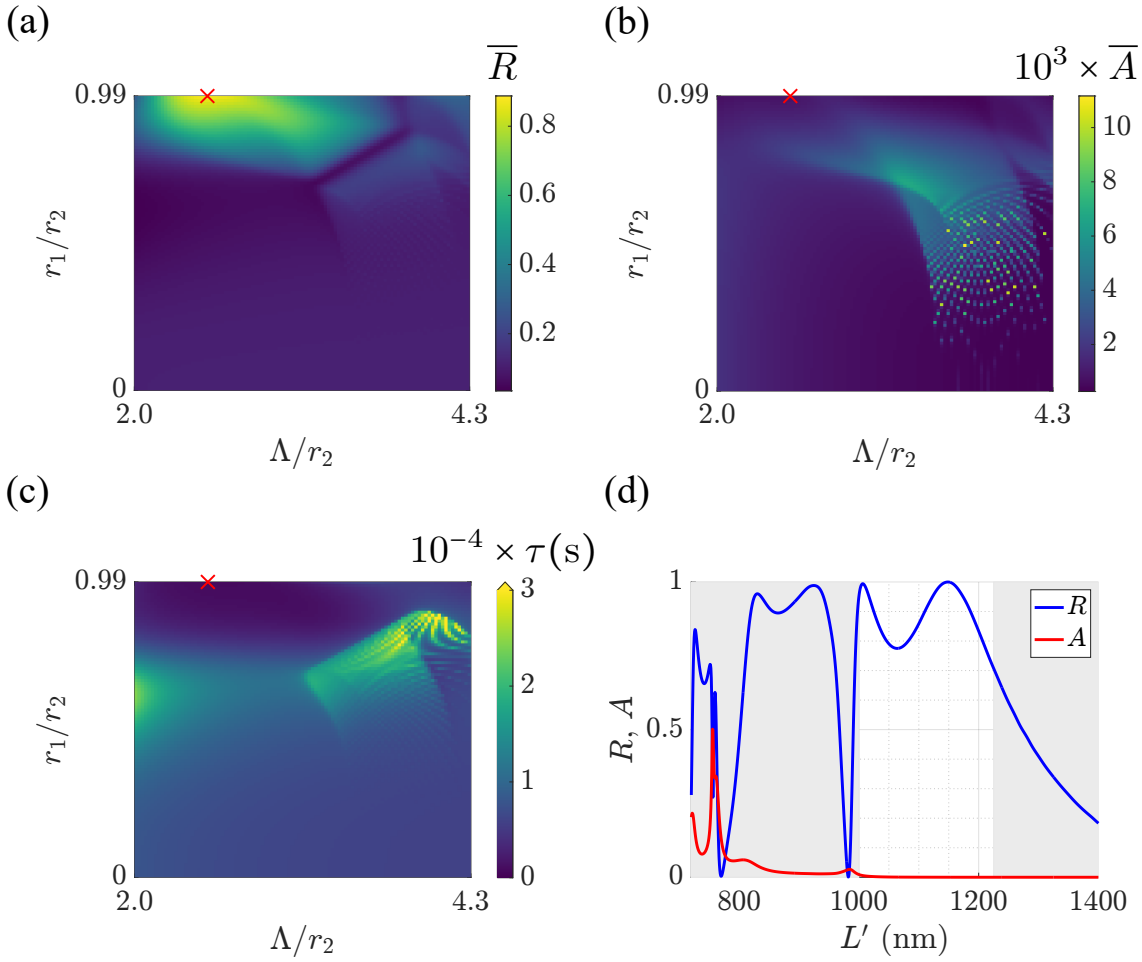

Figure 5.13: The analogous plots to those in Figs 5.5 and 5.12 but for an average reflectance of $\overline{R} = 0.887$. With the lower radii, there is no longer a lattice resonance in the desired wavelength range marked in white. Here, the radius of each outer shell is $r_2 = 180.8$ nm. Adapted from [P2] under the CC BY 4.0 license.

6 | Circular Dichroism of Relativistic Chiral Biomolecules

Introduction

The work discussed in this chapter is based on Ref. [P3], and was carried out with Benedikt Zerulla, Marjan Krstić, Maxim Vavilin, Christof Holzer, Markus Nyman, Lukas Rebholz and Ivan Fernandez-Corbaton. Specifically, the transmission circular dichroism (TCD) of relativistically moving chiral biomolecules will be investigated, and the effect of the molecules' speed on the TCD will be visualised. As a result, this chapter explores the fundamental problem of how non-symmetric, relativistically moving structures scatter light. The findings serve as an extension to the symmetric or periodic structures considered in the previous two chapters.

Recently, the study of interstellar chiral molecules has attracted a great deal of interest in the scientific community [137–146]. Arguably the most notable contribution in this field is that published by McGuire *et al.* in 2016, where the first known chiral molecule in space, propylene oxide (CH_3CHCH_2O), was discovered [71]. In Ref. [71], the propylene oxide molecules were found by studying their absorption towards the Galactic Centre. The source of the incident light was the giant molecular gas cloud Sagittarius B2 (Sgr B2). In this chapter, an analogous setup will be considered, where a backlit molecule moves towards an observer. As mentioned, the quantity to be investigated is the TCD discussed in Section 2.4. Recall that the TCD is the difference between the transmittances due to incident light with positive and negative helicities. Given that molecules are very likely to be found in randomly oriented clusters, the specific quantity of interest is the rotationally averaged TCD (RATCD). The RATCD is a suitable quantity to explore since illuminating molecular clusters corresponds to illuminating one molecule from all angles. To obtain the RATCD, the T-matrix method discussed in Section 2.2 will be applied.

This chapter is structured as follows. Firstly, the scattering setup is outlined in Section 6.1, and the expression used to obtain the required T-matrices is defined. The considered T-matrices were computed by Marjan Krstić and Christof Holzer using quantum chemistry methods as implemented in TURBOMOLE [109]. Furthermore, the method used to rotationally average the molecules will be visualised and explained. Subsequently, the frame-hopping method (FHM) discussed in Chapter 3 will be implemented, beginning with the first step in Section 6.2. Here, the incident field will be boosted from the light source's frame F to the molecules' frame F'. Next, the spherical field expansion coefficients of the scattered field will be obtained in frame F' in line with the second step of the FHM. The third step of the FHM is then carried out in Section 6.3, where the RATCD is determined as seen by an observer in frame F. It is also explained why one should convert the expansion coefficients from the spherical basis to the plane-wave basis. Moreover, the outgoing field will be determined in frame F from the scattered field by incorporating a correction to account for the incoming field. The reason for considering the outgoing field is that it contains the incoming

and scattered fields in the forward direction, which is exactly what is required to determine the RATCD. Finally, the resulting RATCD spectra will be visualised in Section 6.4, where the effects due to Doppler shifts of the incident field become apparent.

6.1 Description of the scattering scenario

In this chapter, an observer in frame F observes molecules moving towards them with velocity $-v\hat{\mathbf{z}}$, where $0 < v < c$. The molecules move in an inertial reference frame F', and the source of the incident field is located behind the molecules on the z-axis (cf. Fig. 6.1).

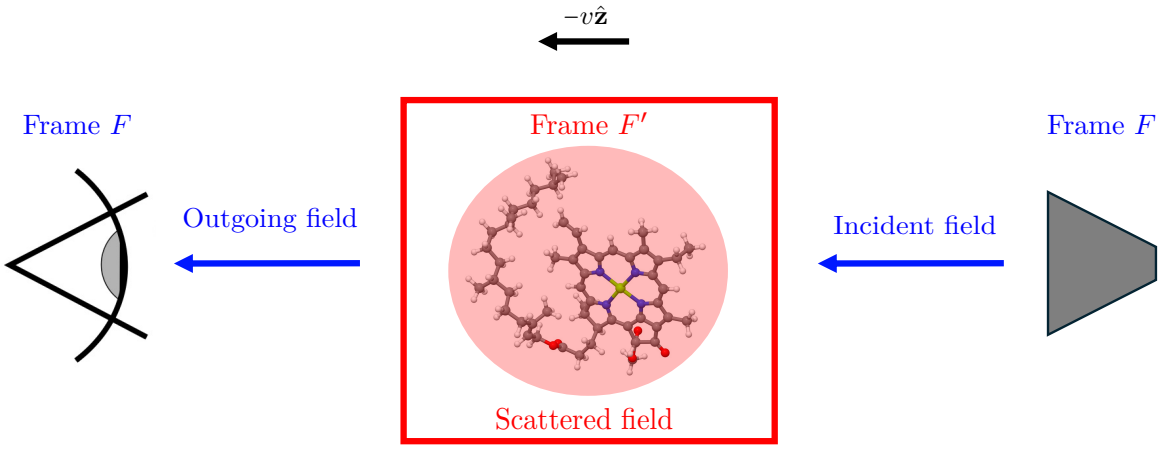

Figure 6.1: A visualisation of the scattering scenario. The molecules (chlorophyll *a* in this case) move in the $-z$-direction at speed v in frame F. The molecules are backlit by an incident field propagating in the $-z$-direction. The scattered field is obtained in frame F' and boosted to frame F. In frame F, the outgoing field is observed by combining the scattered and incoming fields, and the RATCD is determined. The depiction of the chlorophyll *a* molecule was created by Marjan Krstić, and was taken from [P3] under the CC BY 4.0 license.

Just like in Chapter 4, the incident field is expressed in the helicity basis and has a pure helicity. Recall the practicality of using the helicity basis due to the invariance of the helicity of an electromagnetic field under Lorentz boosts. Since the TCD is measured in frame F, the FHM outlined in Chapter 3 will be implemented. Specifically, the TCD will be determined in frame F', and the result is inverse Lorentz boosted back to frame F. It is in frame F where the TCD is observed. To obtain the TCD, the outgoing field will be considered as opposed to the scattered field. The reason for this is that the CD of an object is usually defined with respect to the outgoing field [99]. Also, the TCD is measured in the forward direction, meaning both the incident and scattered fields contribute to it. As a result, it is precisely the outgoing field that is received by the observer.

Typically, one can use the helical S-matrix defined in Eq. (2.72) to determine the outgoing field. However, one would have to either assume an infinitely extended, periodic scatterer (like in the previous chapter) or consider an incident wave truncated at a maximum multipolar order $\ell_{\max}$. Since the incident field is a plane wave, and the scatterer is now finite in space, a modification needs to be made. Specifically, the dipolar T-matrix ($\ell_{\max} = 1$) of a

molecule

$$\mathbf{T}_{\mathrm{mol}} = \frac{\mathrm{i}c_{\mathrm{h}}Z_{\mathrm{h}}k_{\mathrm{h}}^3}{6\pi}\begin{pmatrix} \mathbf{U}\left(\boldsymbol{\alpha}_{\mathrm{ee}}\right)\mathbf{U}^{-1} & \mathbf{U}\left(-\mathrm{i}\boldsymbol{\alpha}_{\mathrm{em}}/Z_{\mathrm{h}}\right)\mathbf{U}^{-1} \\ \mathbf{U}\left(\mathrm{i}\boldsymbol{\alpha}_{\mathrm{me}}/c_{\mathrm{h}}\right)\mathbf{U}^{-1} & \mathbf{U}\left(\boldsymbol{\alpha}_{\mathrm{mm}}/c_{\mathrm{h}}Z_{\mathrm{h}}\right)\mathbf{U}^{-1} \end{pmatrix} \tag{6.1}$$

is used, along with a correction to account for higher-order terms. The exact nature of this correction will be discussed in a later section. In Eq. (6.1), $\boldsymbol{\alpha}_{xy}$ represent the 3×3 complex dynamic polarisability tensors of the molecules. These polarisability tensors were determined via quantum chemistry calculations by Marjan Krstić and Christof Holzer. Moreover, the unitary translation matrix

$$\mathbf{U} = \frac{1}{\sqrt{2}}\begin{pmatrix} 1 & \mathrm{i} & 0 \\ 0 & 0 & \sqrt{2} \\ -1 & \mathrm{i} & 0 \end{pmatrix} \tag{6.2}$$

transforms a T-matrix from the Cartesian basis to the spherical basis. The term $c_{\mathrm{h}} = 1/\sqrt{\varepsilon_{\mathrm{h}}\mu_{\mathrm{h}}}$ generally denotes the speed of light in the medium surrounding the object, and $Z_{\mathrm{h}} = \sqrt{\mu_{\mathrm{h}}/\varepsilon_{\mathrm{h}}}$ is the wave impedance [99]. It is important to note that the quantum chemistry calculations account for the surrounding medium. Therefore, $c_{\mathrm{h}} = c_0$ was used to ensure consistency. In this chapter, the entire surrounding medium is water. This is a good approximation since many water molecules surround each biomolecule in reality.

It is important to emphasise that a T-matrix approximated up to dipolar order is sufficient due to the molecules only being of nanometre scale. In other words, $\mathbf{T}_{\mathrm{mol}}$ has dimensions 6×6. Since a molecule is so small, it does not make sense to consider just one as the scatterer. It is much more likely for molecules to be found in clusters, as is the case with DNA in living beings. In these clusters, the molecules are randomly oriented. To this end, the rotationally averaged TCD (RATCD) will be considered in this chapter. The RATCD can be determined in two ways:

1. The incident light is rotated by n_{rot} angles of orientation around the scatterer and the TCD in these directions is simulated. Then, all TCD signals are summed, and the result is divided by n_{rot}.

2. The same process as in 1., but the incident light propagates in one direction and the molecule itself is rotated. Here, one generally needs to consider the three Euler angles of rotation (Ψ, Θ, Φ) defined in Section 2.2.5. It will later be demonstrated, however, that only Θ and Ψ are needed in this chapter.

Note that both methods are mathematically equivalent, but the second is preferred since, from a conceptual point of view, it is unlikely that the molecules would be illuminated from all directions in outer space. The second method is also favourable, since a molecule rotated many times is essentially the same as the abovementioned cluster. A pictorial representation of the previous two methods for rotations $\Theta \in \{\theta_1, \ldots, \theta_{n_{\mathrm{rot}}}\}$ for a given Ψ and Φ is presented in Fig. 6.2.

To capture the RATCD properly, the molecules need to be rotated such that they are exposed as much as possible to the incident light. Accordingly, a sample of 50 equally spaced rotation angles was used. To ensure this equal spacing, the angles were obtained using a gradient descent optimisation algorithm [147]. For reference, all steps required to determine the rotationally-averaged TCD are depicted in Fig. 6.3.

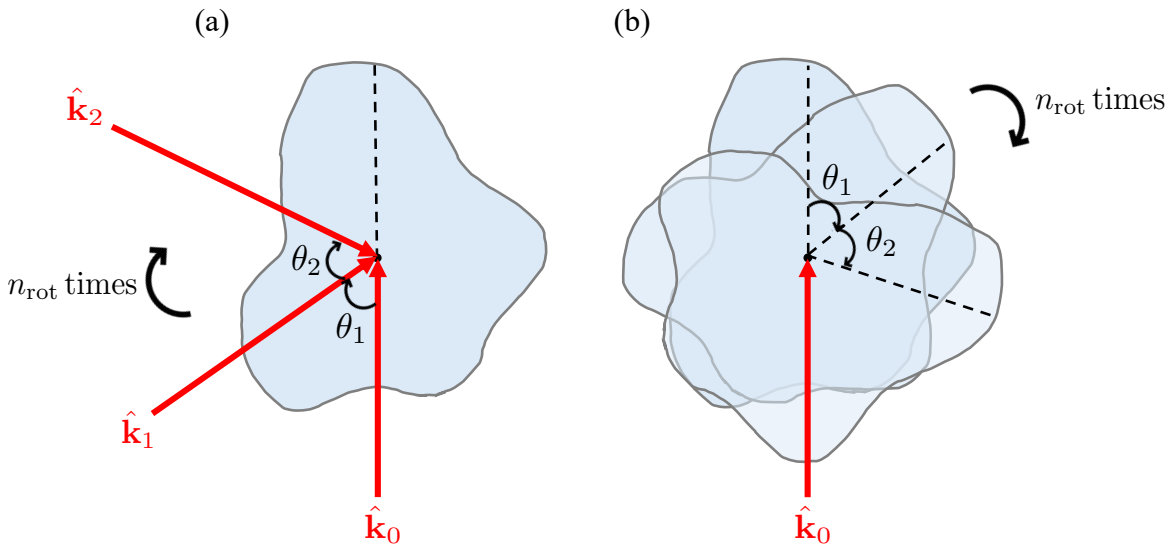

Figure 6.2: A pictorial representation of two methods to determine the rotationally-averaged transmission circular dichroism (RATCD) of an arbitrary object for one of the rotation parameters $\Theta \in \{\theta_1, \ldots, \theta_{n_{\mathrm{rot}}}\}$, where n_{rot} is the number of rotation angles. Firstly, as shown in (a), the incident light can be rotated by n_{rot} angles of orientation around the scatterer, where the TCD in all directions is recorded. Then, all TCD signals are summed, and the result is divided by n_{rot}. The second method is shown in (b). Here, the incident light propagates in one direction $\hat{\mathbf{k}}_0$ and the molecule itself is rotated. Again, the TCD for each rotation angle Θ is recorded. Then, all TCD signals are summed, and the result is divided by n_{rot}. For conceptual reasons, the approach shown in (b) is chosen in this work.

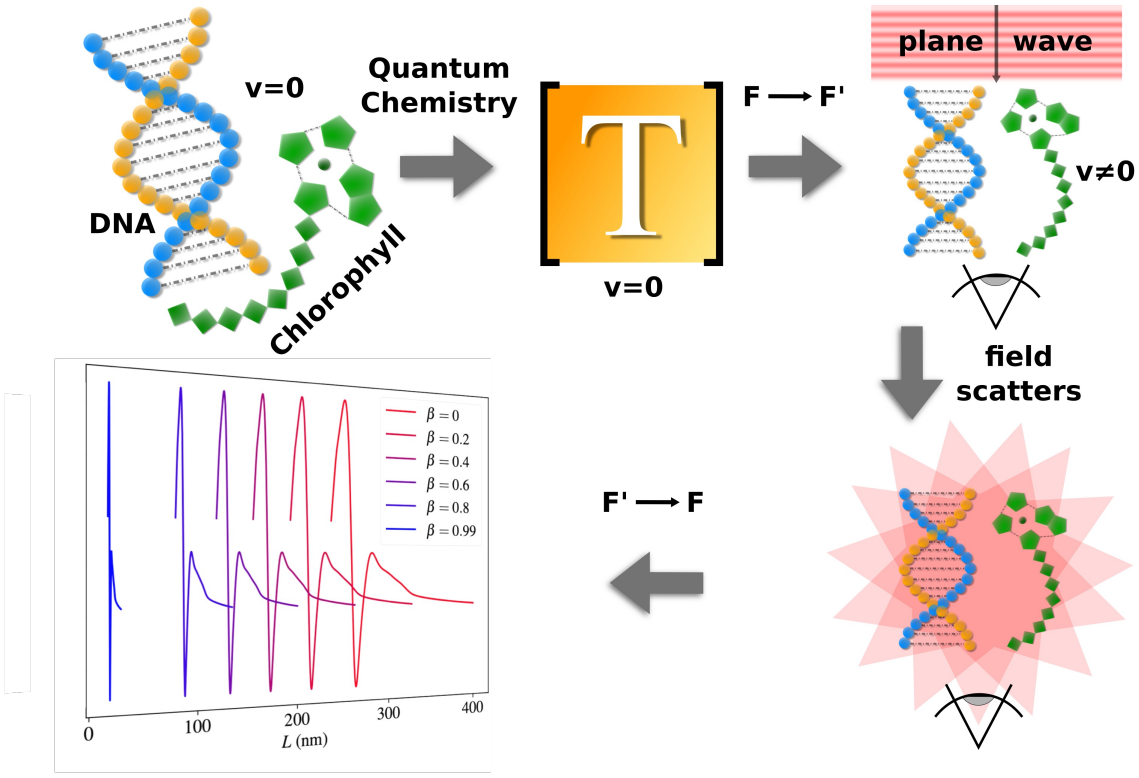

Figure 6.3: The process for determining the RATCD in the reference frame F involves several steps. Firstly, the molecular structures are generated, and their T-matrices are calculated using TURBOMOLE. To describe the scattering process, the incident plane wave propagating in the $-z$-direction is boosted to frame F'. In frame F', the outgoing field is determined by combining the scattered field with the incoming field, as shown in Eqs (6.20) and (6.21). Finally, the outgoing field is boosted back to the original frame F. It is in frame F where the RATCD is measured. Adapted from [P3] under the CC BY 4.0 license.

In this section, the scattering setup was outlined, and the necessary expression for the T-matrices used to determine the outgoing field was defined. It was also explained why a rotational average of the TCD should be done instead of determining the TCD for just one molecule. In the next section, the first step of the FHM described in Chapter 3 will be carried out.

6.2 Boosting the incident field into the molecules' frame

After having outlined the scattering scenario, one can now implement the FHM. To begin, an incident electric field $\mathbf{E}_\mathrm{i}(\mathbf{r},t)$ in frame F must be defined. Note that the 'i' subscript stands for 'incident'. Of course, there will always be an accompanying magnetic field, but explicit reference to it will be omitted. Recall that the incident field takes the form of a plane wave of pure helicity denoted by λ_i. As such, $\mathbf{E}_\mathrm{i}(\mathbf{r},t)$ is given by

$$\begin{aligned}\mathbf{E}_\mathrm{i}(\mathbf{r},t) &= \sum_{\lambda_\mathrm{i}=\pm1} E_{\mathrm{i},\,\lambda_\mathrm{i}}\hat{\mathbf{e}}_{\lambda_\mathrm{i}}(\hat{\mathbf{k}})\mathrm{e}^{-\mathrm{i}(ckt-\mathbf{k}\cdot\mathbf{r})}\\ &= \sum_{\lambda_\mathrm{i}=\pm1}\int_{\mathbb{R}^3}\frac{\mathrm{d}^3\mathbf{k}}{k}\,\hat{\mathbf{e}}_{\lambda_\mathrm{i}}(\hat{\mathbf{k}})f_{\lambda_\mathrm{i}}(\mathbf{k})\,k\mathrm{e}^{-\mathrm{i}(ckt-\mathbf{k}\cdot\mathbf{r})}\\ &\equiv \sum_{\lambda_\mathrm{i}=\pm1}\int_{\mathbb{R}^3}\frac{\mathrm{d}^3\mathbf{k}}{k}f_{\lambda_\mathrm{i}}(\mathbf{k})\,|\lambda_\mathrm{i}\,\mathbf{k}\rangle\\ &= |\mathbf{E}_\mathrm{i}\rangle\ ,\end{aligned} \tag{6.3}$$

where $E_{\mathrm{i},\,\lambda_\mathrm{i}}=1$, and $\hat{\mathbf{e}}_{\lambda_\mathrm{i}}(\hat{\mathbf{k}})$ is defined in Eq. (2.39). For a plane wave with a given orientation described by the angles θ and ϕ, the expansion coefficient $f_{\lambda_\mathrm{i}}(\mathbf{k})$ takes the form

$$f_{\lambda_\mathrm{i}}(\mathbf{k}) = \frac{1}{k^2}\delta(k-k_\mathrm{i})\delta(\cos\theta-\cos\theta_\mathrm{i})\delta(\phi-\phi_\mathrm{i})\,, \tag{6.4}$$

where $\theta_\mathrm{i}=\pi$ and $\phi_\mathrm{i}=0$ for a field propagating in the $-z$-direction. In the previous equation, $\delta(x)$ represents the Dirac delta distribution. Furthermore, the ket

$$|\lambda_\mathrm{i}\,\mathbf{k}\rangle \equiv k\hat{\mathbf{e}}_{\lambda_\mathrm{i}}(\hat{\mathbf{k}})\mathrm{e}^{-\mathrm{i}(ckt-\mathbf{k}\cdot\mathbf{r})} \tag{6.5}$$

represents the plane wave using Dirac notation. Note the appearance of the Lorentz invariant integration measure $\mathrm{d}^3\mathbf{k}/k$ in Eq. 6.3 to conform with the convention used in Ref. [119]. The same convention was used in Ref. [P3] and is also implemented in this chapter. To compensate for the abovementioned integration measure, the unconventional prefactor k is present in (6.5).

To boost the incident field $|\mathbf{E}_\mathrm{i}\rangle$ from frame F to frame F', the Lorentz boost operator $\hat{\mathbf{L}}_z(\beta)$ defined in Eq. (3.1) can be implemented as follows [119]:

$$\begin{aligned}\left|\mathbf{E}'_\mathrm{i}\right\rangle &= \hat{\mathbf{L}}_z(\beta)\,|\mathbf{E}_\mathrm{i}\rangle\\ &= \sum_{\lambda'_\mathrm{i}=\pm1}\delta_{\lambda_\mathrm{i}\lambda'_\mathrm{i}}\int_{\mathbb{R}^3}\frac{\mathrm{d}^3\mathbf{k}}{k}f_{\lambda_\mathrm{i}}(\mathbf{k})\left|\lambda'_\mathrm{i}\;\hat{\mathbf{L}}_z(\beta)\mathbf{k}\right\rangle\\ &= \frac{1}{k_\mathrm{i}}\sum_{\lambda'_\mathrm{i}=\pm1}\delta_{\lambda_\mathrm{i}\lambda'_\mathrm{i}}\left|\lambda'_\mathrm{i}\;\hat{\mathbf{L}}_z(\beta)\mathbf{k}_\mathrm{i}\right\rangle,\end{aligned} \tag{6.6}$$

where the Kronecker delta $\delta_{\lambda_\mathrm{i}\lambda_\mathrm{i}'}$ captures helicity conservation under the Lorentz boost.

The first step of the FHM is now complete, and the incident field has been expressed in the molecules' frame F'. In the next section, the second step of the FHM will be implemented, where the dipolar scattered field is obtained. Recall that the outgoing field will be determined from the scattered field via a correction accounting for higher-order multipoles.

Solving the scattering problem in the molecules' frame

Armed with Eq. (6.6) for the incident field in F', the scattered field can now be determined. As always, the T-matrix method will be implemented, this time using $\mathbf{T}_\mathrm{mol}$ from Eq. (6.1). To this end, $|\mathbf{E}_\mathrm{i}'\rangle$ needs to be expressed in the spherical basis as

$$\left|\mathbf{E}_\mathrm{i}'\right\rangle = \int_0^\infty \mathrm{d}k'\, k' \sum_{\lambda_\mathrm{i}'=\pm1} \sum_{\ell'=1}^{\infty} \sum_{m'=-\ell'}^{\ell} A'_{\ell' m' \lambda_\mathrm{i}'}(k') \delta_{\lambda_\mathrm{i}'\lambda_\mathrm{i}} \left|k'\, \ell'\, m'\, \lambda_\mathrm{i}'\right\rangle \,. \tag{6.7}$$

Note again the unconventional prefactor k'. For a plane wave moving in the $-z$-direction ($\theta' = \pi$ and $\phi' = 0$), the expansion coefficients $A'_{\ell' m' \lambda_\mathrm{i}'}(k')$ are expressed as [119]

$$\begin{aligned} A'_{\ell' m' \lambda_\mathrm{i}'}(k') &= \sqrt{\frac{2\ell'+1}{4\pi}} \int_0^{2\pi} \mathrm{d}\phi' \int_{-1}^{1} \mathrm{d}(\cos\theta') D^{\ell'}_{m'\lambda_\mathrm{i}'}(\phi', \theta', 0) f_{\lambda_\mathrm{i}'}(\mathbf{k}') \\ &= \sqrt{\frac{2\ell'+1}{4\pi}} D^{\ell'}_{m'\lambda_\mathrm{i}'}(0, \pi, 0) \frac{1}{k'^2} \delta(k' - k_\mathrm{i}') \,, \end{aligned} \tag{6.8}$$

where the multipolar indices ℓ' and m' were defined in Section 2.2.

Moreover, for a general helicity λ and Euler angles Ψ, Θ and Φ, $D^{\ell}_{m\lambda}(\Psi, \Theta, \Phi)$ is the Wigner-D matrix element, where [17]

$$D^{\ell}_{m\lambda}(\Psi, \Theta, \Phi) = \mathrm{e}^{-\mathrm{i}m\Psi} d^{\ell}_{m\lambda}(\Theta) \mathrm{e}^{-\mathrm{i}\lambda\Phi} \,, \tag{6.9}$$

and $d^{\ell}_{m\lambda}(\Theta)$ are the Wigner d-functions defined in [148, Section 7.3.].

Finally, the basis ket $|k'\, \ell'\, m'\, \lambda_\mathrm{i}'\rangle$ is related to the boosted plane wave ket $\left|\lambda_\mathrm{i}'\ \hat{\mathbf{L}}_z(\beta)\mathbf{k}_\mathrm{i}\right\rangle$ as [149]

$$\left|k'\, \ell'\, m'\, \lambda_\mathrm{i}'\right\rangle = \sqrt{\frac{2\ell'+1}{4\pi}} \int_0^{2\pi} \mathrm{d}\phi' \int_{-1}^{1} \mathrm{d}(\cos\theta') D^{\ell'}_{m'\lambda_\mathrm{i}'}(\phi', \theta', 0)^* \left|\lambda_\mathrm{i}'\ \hat{\mathbf{L}}_z(\beta)\mathbf{k}_\mathrm{i}\right\rangle \,. \tag{6.10}$$

Recall that only dipolar terms need to be considered as the molecules are only of nanometre scale.

Analogous to the incident field, the scattered field with expansion coefficients $B'_{\ell' m' \lambda_\mathrm{s}'}(k')$ can be written as

$$\left|\mathbf{E}_\mathrm{s}'\right\rangle = \int_0^\infty \mathrm{d}k'\, k' \sum_{\lambda_\mathrm{s}'=\pm1} \sum_{\ell'=1}^{\infty} \sum_{m'=-\ell'}^{\ell} B'_{\ell' m' \lambda_\mathrm{s}'}(k') \left|k'\, \ell'\, m'\, \lambda_\mathrm{s}'\right\rangle \,, \tag{6.11}$$

where the 's' superscript stands for 'scattered'. The scattered and incident expansion coefficients are connected via the helicity T-matrix $\mathbf{T}^\mathrm{H}_\mathrm{mol}$ obtained from $\mathbf{T}_\mathrm{mol}$ using *treams* [92]. In matrix form, the expansion coefficients are related as

$$\mathbf{B}'^{+} = \mathbf{T}^\mathrm{H}_\mathrm{mol} \begin{pmatrix} \mathbf{A}_3'^{+} \\ \mathbf{0}_3 \end{pmatrix} \quad \text{and} \quad \mathbf{B}'^{-} = \mathbf{T}^\mathrm{H}_\mathrm{mol} \begin{pmatrix} \mathbf{0}_3 \\ \mathbf{A}_3'^{-} \end{pmatrix} \,, \tag{6.12}$$

where the '+' and '-' superscripts refer to the terms corresponding to the positive and negative helicity components of the incident field, respectively. The '3' subscript in Eq. (6.12) denotes a vector with dimension 3×1 required for dipoles. Accordingly, $\mathbf{0}_3$ is the 3×1 zero vector. Recall from Chapter 4 that, even though the incident field has either a positive or negative helicity, the scattered field can have a combination of both.

As mentioned above, the goal is to obtain the RATCD. Correspondingly, the matrix $\mathbf{T}^{\mathrm{H}}_{\mathrm{mol}}$ is also rotationally averaged for 50 orientations Θ' and Φ'. Recall the orientation angles need to be equally-spaced to ensure full coverage of the molecules. Specifically, the equal spacing needs to occur in frame F' since it is here where the scattered field is initially determined. Note that 50 orientation angles were deemed sufficient to ensure convergence of the RATCD spectra. This convergence was found by testing increasing numbers of orientation angles.

Using the rotated T-matrix defined in Eq. (2.67), the scattered field expansion coefficients $\mathbf{B}'^{\pm}(\Theta', \Phi'; k')$ for each angle Θ' and Φ' are obtained from

$$\mathbf{B}'^{\pm}(\Theta', \Phi'; k') = \mathbf{T}^{\mathrm{H}}_{\mathrm{mol,\,R}}(\Theta', \Phi')\mathbf{A}'^{\pm}(k')\,, \tag{6.13}$$

where $\mathbf{T}^{\mathrm{H}}_{\mathrm{mol,\,R}}(\Theta', \Phi')$ is the rotated molecule T-matrix. Note that only two Euler angles are considered in the previous equation instead of the usual three. For the case of a circularly polarised plane wave $\left|\lambda\ \hat{\mathbf{k}} = -\hat{\mathbf{z}}\right\rangle$ of well-defined helicity λ propagating along the $-z$-axis, the first rotation about the z-axis by angle Ψ simply gives rise to a phase term that ultimately cancels. When the helicity of the incident and scattered fields are the same ($\lambda_{\mathrm{i}} = \lambda_{\mathrm{s}} = \lambda$), the cancellation can be seen by applying a general T-matrix $\mathbf{T}^{\mathrm{H}}_{\mathrm{R}}(\Theta, \Phi)$ to $\left|\lambda\ \hat{\mathbf{k}} = -\hat{\mathbf{z}}\right\rangle$ in the following way:

$$\begin{aligned}
\left\langle \lambda\ \hat{\mathbf{k}} = -\hat{\mathbf{z}}\right| \mathbf{T}^{\mathrm{H}}_{\mathrm{R}}(\Theta, \Phi) \left|\lambda\ \hat{\mathbf{k}} = -\hat{\mathbf{z}}\right\rangle &= \left\langle \lambda\ \hat{\mathbf{k}} = -\hat{\mathbf{z}}\right| \mathbf{R}(\Psi, \Theta, \Phi)\mathbf{T}^{\mathrm{H}}\mathbf{R}^{-1}(\Psi, \Theta, \Phi) \left|\lambda\ \hat{\mathbf{k}} = -\hat{\mathbf{z}}\right\rangle \\
&= \left\langle \lambda\ \hat{\mathbf{k}} = -\hat{\mathbf{z}}\right| \mathrm{e}^{\mathrm{i}\Psi}\mathbf{R}(\Theta, \Phi)\mathbf{T}^{\mathrm{H}}\mathbf{R}^{-1}(\Theta, \Phi)\mathrm{e}^{-\mathrm{i}\Psi} \left|\lambda\ \hat{\mathbf{k}} = -\hat{\mathbf{z}}\right\rangle \\
&= \left\langle \lambda\ \hat{\mathbf{k}} = -\hat{\mathbf{z}}\right| \mathbf{R}(\Theta, \Phi)\mathbf{T}^{\mathrm{H}}\mathbf{R}^{-1}(\Theta, \Phi) \left|\lambda\ \hat{\mathbf{k}} = -\hat{\mathbf{z}}\right\rangle .
\end{aligned} \tag{6.14}$$

Qualitatively, the phase term $\mathrm{e}^{\mathrm{i}\Psi}$ in Eq. (6.14) cancels upon multiplication with its complex conjugate $\mathrm{e}^{-\mathrm{i}\Psi}$.

On the other hand, when the helicities of the incident and scattered fields are different ($\lambda_{\mathrm{s}} = -\lambda_{\mathrm{i}} = -\lambda$), one has

$$\begin{aligned}
\left\langle -\lambda\ \hat{\mathbf{k}} = -\hat{\mathbf{z}}\right| \mathbf{T}^{\mathrm{H}}_{\mathrm{R}}(\Theta, \Phi) \left|\lambda\ \hat{\mathbf{k}} = -\hat{\mathbf{z}}\right\rangle &= \left\langle -\lambda\ \hat{\mathbf{k}} = -\hat{\mathbf{z}}\right| \mathbf{R}(\Psi, \Theta, \Phi)\mathbf{T}^{\mathrm{H}}\mathbf{R}^{-1}(\Psi, \Theta, \Phi) \left|\lambda\ \hat{\mathbf{k}} = -\hat{\mathbf{z}}\right\rangle \\
&= \mathrm{e}^{2\mathrm{i}\Psi} \left\langle -\lambda\ \hat{\mathbf{k}} = -\hat{\mathbf{z}}\right| \mathbf{R}(\Theta, \Phi)\mathbf{T}^{\mathrm{H}}\mathbf{R}^{-1}(\Theta, \Phi) \left|\lambda\ \hat{\mathbf{k}} = -\hat{\mathbf{z}}\right\rangle .
\end{aligned} \tag{6.15}$$

When determining the TCD in the next section, the magnitude squared of Eq. (6.15) will be required. Since $|\mathrm{e}^{2\mathrm{i}\Psi}|^2 = 1$, the phase term also vanishes for different helicities, demonstrating why the first Euler angle Ψ can be ignored.

In this section, the scattered field was obtained in frame F' using the T-matrix of a molecule. The process of rotationally averaging the T-matrix was also outlined, serving as preparation for determining the RATCD in the next section.

6.3 Obtaining the rotationally averaged TCD (RATCD) in the lab frame

Having obtained an expression for the spherical scattered field coefficients $\mathbf{B}'^{\pm}(\Theta', \Phi'; k')$ in frame F', one can now begin with the TCD calculations. Recall that the goal is to derive an expression for the RATCD in frame F. As a result, the third step of the FHM will now be carried out. The incident field propagates along the $-z$-axis, so only the scattered field component in the same direction should be considered. This is because the TCD is measured in the forward direction.

As will become clear, it is wise to convert the spherical field coefficients $\mathbf{B}'^{\pm}(\Theta', \Phi'; k')$ to those in the plane wave basis. The scattered plane wave coefficients are denoted by $E'^{\pm}_{\mathrm{s},\,\lambda_\mathrm{s}=\pm1}(\Theta', \Phi'; k')$, where

$$E'^{\pm}_{\mathrm{s},\,\lambda_\mathrm{s}=\pm1}(\Theta', \Phi'; k') = -\sqrt{2}E'^{\pm}_{\mathrm{s},\,\lambda_\mathrm{s}=\pm1,\theta'_\mathrm{s}=\pi}(\Theta', \Phi'; k')\,. \tag{6.16}$$

The equation for the coefficients $E'^{\pm}_{\mathrm{s},\,\lambda_\mathrm{s}=\pm1,\theta'_\mathrm{s}=\pi}(\Theta', \Phi'; k')$ was derived in the supplementary information of Ref. [P3], and corresponds to the polar (θ'_s) components of the scattered field. Note that the '$\pm$' superscript has the same meaning as in the previous section.

The next step is to inverse Lorentz boost the coefficients $E'^{\pm}_{\mathrm{s},\,\lambda_\mathrm{s}=\pm1}(\Theta', \Phi'; k')$ from frame F' to frame F, where the RATCD is observed. From [119, Eq. (24)], one finds that

$$\begin{aligned}\hat{\mathbf{L}}_z^{-1}(\beta)E'^{\pm}_{\mathrm{s},\,\lambda_\mathrm{s}=\pm1}(\Theta', \Phi'; k') &= E^{\pm}_{\mathrm{s},\,\lambda_\mathrm{s}=\pm1}(\beta)\left[\Theta', \Phi'; \hat{\mathbf{L}}_z^{-1}(\beta)k'\right] \\ &= E^{\pm}_{\mathrm{s},\,\lambda_\mathrm{s}=\pm1}\left[\Theta', \Phi'; k'\Delta(-\beta)\right]\,, \quad 0 \leq \beta < 1\,,\end{aligned} \tag{6.17}$$

where $\hat{\mathbf{L}}_z^{-1}(\beta)$ is the inverse of the operator $\hat{\mathbf{L}}_z(\beta)$ defined in Eq. (3.1). Moreover, the function $\Delta(\beta)$ is defined in Eq. (3.7) and represents a Doppler shift along the z-axis. Note that $\Delta(-\beta)$ represents the inverse of $\Delta(\beta)$ such that

$$\Delta(-\beta) = \Delta^{-1}(\beta)\,. \tag{6.18}$$

The RATCD will be visualised as a function of the wavelength L in frame F. Accordingly, the coefficients $E^{\pm}_{\mathrm{s},\,\lambda_\mathrm{s}=\pm1}\left[\Theta', \Phi'; k'\Delta(-\beta)\right]$ can be written as

$$\begin{aligned}E^{\pm}_{\mathrm{s},\,\lambda_\mathrm{s}=\pm1}\left[\Theta', \Phi'; k'\Delta(-\beta)\right] &= E^{\pm}_{\mathrm{s},\,\lambda_\mathrm{s}=\pm1}\left[\Theta', \Phi'; L'\Delta(\beta)\right] \\ &= E^{\pm}_{\mathrm{s},\,\lambda_\mathrm{s}=\pm1}\left(\Theta', \Phi'; L\right)\,,\end{aligned} \tag{6.19}$$

where $k' = 2\pi/L'$ was used, and L' is the wavelength in frame F'. Note that the values for L' are always constant, so the wavelengths in frame L must change with speed. Specifically, the wavelengths in frame F simply scale as $L = L'\Delta(\beta)$. Equation (6.19), therefore, shows that a Lorentz boost has no effect on the magnitude of each plane wave expansion coefficient and only makes their spectra more narrow in frame F. Recall that this Doppler shift is depicted in Fig. 3.2 (b). Note that the light source now moves towards the observer as opposed to the other way around as shown in Fig. 3.2 (b). Both scenarios are physically equivalent, however, so the same Doppler shift is observed.

Recall the practicality of boosting plane wave coefficients as opposed to those in the spherical basis described by multipoles. Boosting plane wave coefficients retains all information

about the relevant field, while boosting multipoles gives rise to infinitely many higher-order terms. In this chapter, for example, the dipolar scattered field in frame F' is not dipolar in frame F. As a result, one would have to find where the multipolar expansion converges in frame F, which can be difficult. This acquisition of higher-order multipoles is demonstrated in [149, Fig. (1)] for a boosted quadrupole.

Returning to determining the RATCD in frame F, one must first compute the relevant transmittances $T^{\pm}(\Theta', \Phi'; L)$, where

$$T^{+}(\Theta', \Phi'; L) = \left| E^{+}_{\mathrm{s},\,\lambda_\mathrm{s}=1}(\Theta', \Phi'; L) + E_{\mathrm{in},\,\lambda_\mathrm{i}=1} \right|^2 + \left| E^{+}_{\mathrm{s},\,\lambda_\mathrm{s}=-1}(\Theta', \Phi'; L) \right|^2 , \tag{6.20}$$

$$T^{-}(\Theta', \Phi'; L) = |E^{-}_{\mathrm{s},\,\lambda_\mathrm{s}=1}(\Theta', \Phi'; L)|^2 + |E^{-}_{\mathrm{s},\,\lambda_\mathrm{s}=-1}(\Theta', \Phi'; L) + E_{\mathrm{in},\,\lambda_\mathrm{i}=-1}|^2 , \tag{6.21}$$

and the plane wave coefficients $E_{\mathrm{in},\,\lambda_\mathrm{i}=\pm1} = 1$ belong to the incoming field. The incoming field coefficients serve as the correction terms mentioned in Section 6.1. These correction terms ensure the inclusion of higher-order components of the incoming field in the outgoing field. These higher-order contributions simply pass through the molecules without any interaction.

With the transmittances at hand, one can now define the RATCD $\Delta\mathcal{T}_{\mathrm{avg}}(L)$, where

$$\Delta\mathcal{T}_{\mathrm{avg}}(L) = \frac{1}{n_{\mathrm{rot}}} \sum_{i=1}^{n_{\mathrm{rot}}} [T^{-}(\theta_i, \phi_i; L) - T^{+}(\theta_i, \phi_i; L)] , \tag{6.22}$$

and $n_{\mathrm{rot}} = 50$ is the number of angles used for the rotational average (cf. Fig. 6.2). Since only the sign of the RATCD is of interest, one can normalise the RATCD as:

$$\widetilde{\Delta\mathcal{T}}_{\mathrm{avg}}(L) = \frac{1}{n_{\mathrm{rot}}} \sum_{i=1}^{n_{\mathrm{rot}}} \left[\frac{T^{-}(\theta_i, \phi_i; L) - T^{+}(\theta_i, \phi_i; L)}{T^{-}(\theta_i, \phi_i; L) + T^{+}(\theta_i, \phi_i; L)} \right] , \tag{6.23}$$

where θ_i and ϕ_i correspond to different values of Θ and Φ, respectively. Moreover, the normalisation with respect to $T^{-}(L) + T^{+}(L)$ is represented by the tilde $\widetilde{\ }$. It is this unitless normalised RATCD that will be visualised in the next section.

In this section, the spherical scattered field expansion coefficients were converted to the plane wave basis. The plane wave coefficients were then inverse Lorenz boosted from frame F' to frame F, allowing one to derive an expression for the RATCD in frame F. In the next section, the normalised RATCD spectra in frame F will be analysed as a function of the wavelength L of the incident field and speed parameter β.

6.4 Visualising the boosted RATCD

The normalised RATCD $\widetilde{\Delta\mathcal{T}}_{\mathrm{avg}}(L)$ will now be visualised as a function of the incident field wavelength L in frame F and speed factor β for each molecule. The normalised RATCD spectra for a B-DNA molecule are given in Fig. 6.4, while those for chlorophyll *a* and chlorophyll *b* are given in Fig. 6.5. In Fig. 6.4 (a), the normalised RATCD is shown for every β value and Doppler-shifted wavelength range in F; the data for select speed factors $\beta \in \{0, 0.2, 0.4, 0.6, 0.8, 0.99\}$ are given in Fig. 6.4 (b). The analogous data for chlorophyll *a* and chlorophyll *b* are given in the left and right columns of Fig. 6.5, respectively.

One notices the scaling along the L-axis induced by the Doppler shift as mentioned in the previous section. Specifically, the spectra become infinitely narrow as $\beta \to 1$. This spectral compression makes sense since a constant spectral range is viewed in Frame F'. As a result, the incident field wavelengths in F must be adapted to each speed. The quicker the molecules, the greater the effect of the Doppler shift, and the narrower the spectrum needs to be in frame F.

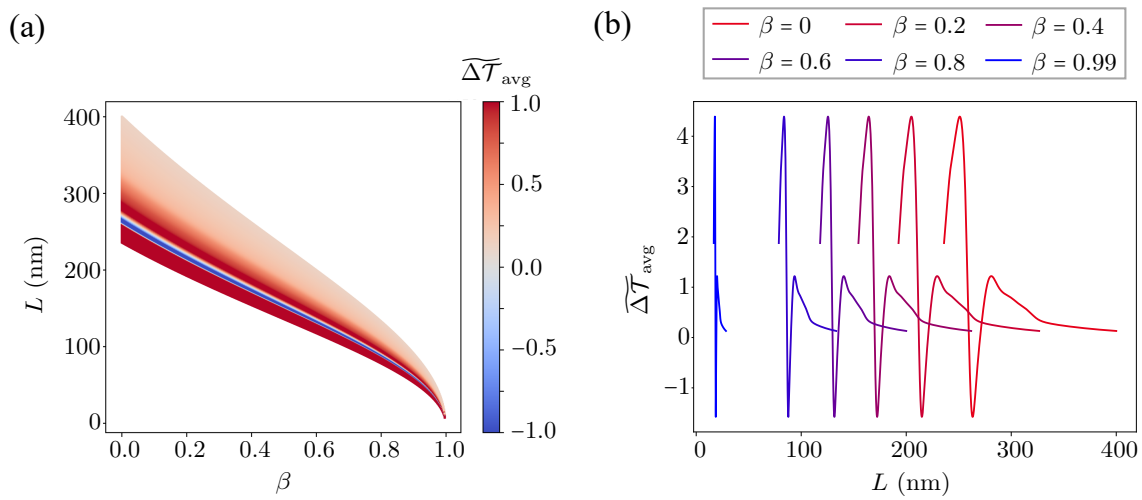

Figure 6.4: (a) The normalised RATCD for the B-DNA molecule as a function of the speed factor β and the incident field wavelengths L in frame F. (b) The TCD at speeds $\beta \in \{0, 0.2, 0.4, 0.6, 0.8, 0.99\}$, highlighting the spectral shift. Adapted from [P3] under the CC BY 4.0 license.

6.5 Summary

To summarise, the rotationally averaged transmission circular dichroism (RATCD) of three relativistically moving chiral biomolecules, B-DNA, chlorophyll *a* and chlorophyll *b* was investigated. The method to obtain the expression for RATCD was reliant on the frame-hopping method (FHM) outlined in Chapter 3. After outlining the scattering setup and the method of rotational averaging, the incident field illuminating the molecules was boosted from its frame F to the molecules' frame F'. In frame F', the scattered field was determined using dipolar T-matrices obtained by Marjan Krstić and Christof Holzer using quantum chemistry methods as implemented in TURBOMOLE [109]. Subsequently, the spherical scattered field coefficients were converted to those in the plane wave basis. Expressing the scattered field in the plane wave basis is very favourable since all information about the scattered field is retained upon boosting. Were one to boost the dipolar scattered field directly, infinitely many multipolar orders would be acquired in frame F [119, 149]. As a result, one would always lose information by truncating the scattered field. Finally, the RATCD spectra were visualised as a function of the incident field wavelength L in frame F and the speed factor β of the molecules. The effects of Doppler shifting were observed, where the RATCD shifts to smaller wavelengths in F as β increases. Interestingly, the signs of the RATCD re-

main unaffected under Lorentz boosts, and the spectra simply compress on the L-axis with increasing speed.

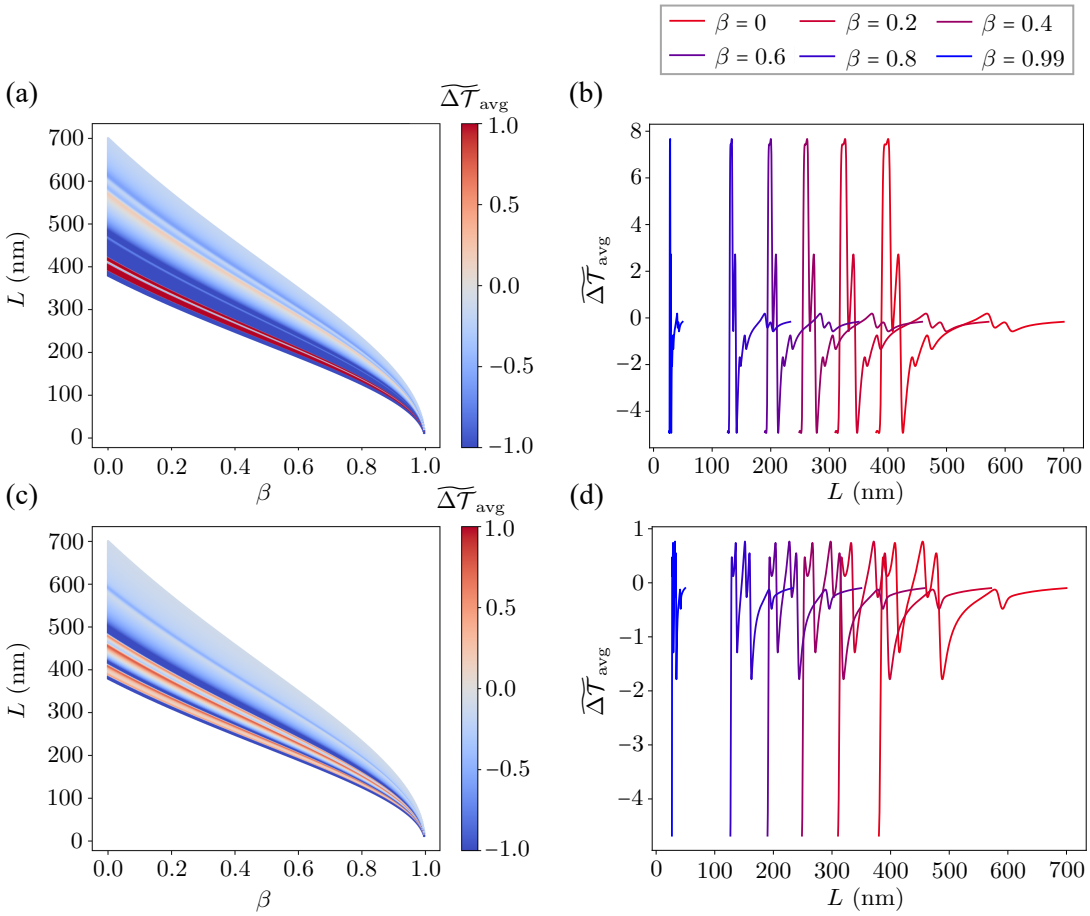

Figure 6.5: The top row shows the analogous plots for chlorophyll *a* to those in Fig. 6.4. The bottom row contains the corresponding information for chlorophyll *b*. Adapted from [P3] under the CC BY 4.0 license.

7 | Conclusions and Outlook

This thesis is concerned with the study of how relativistic motion affects the electromagnetic scattering of light by different objects. The work presented discusses systems of increasing complexity. Firstly, electromagnetic scattering by a single, relativistically moving sphere is explored. Afterwards, the study of a single sphere is extended to that of a periodic array of spheres. Such a system serves as a model for a light sail that could be used to explore neighbouring solar systems. Finally, the circular dichroism of biomolecules is explored under the influence of relativistic effects.

Conclusions

In Chapter 2, the first half of the theoretical groundwork is laid, beginning with Maxwell's equations in their macroscopic form. From Maxwell's equations, the vector Helmholtz equation and vector spherical harmonics (VSHs) are obtained. Importantly, VSHs serve as a foundation for describing electromagnetic fields in the spherical basis. Using VSHs, expressions for incident and scattered spherical electric fields are constructed, and the parity T-matrix, linking these fields, is defined. For a spherical object, the T-matrix contains Mie coefficients, which encode geometric information about the sphere. The conversion of the parity T-matrix to the helicity basis and its rotation, enabling analysis of arbitrarily oriented objects, are detailed. Extending to periodic structures, the formalism for scattering by such systems was described and is utilised in Chapter 5. Finally, the absorption and transmission circular dichroism (CD) of an object was defined. The transmission CD (TCD) was investigated in Chapter 6 for molecular scatterers. Crucially, it was explained at the end of Chapter 2 how the TCD should be modified to account for finite scatterers.

Chapter 3 completes the theoretical background with methods from special relativity. The Lorentz boost, relating stationary lab frame F to the co-moving frame F', was introduced. The frame-hopping method (FHM) was also outlined, which dictates the order in which Lorentz boosts and scattering calculations should take place. Moreover, key effects like the Doppler shift and length contraction are described. Length contraction explains why scattering calculations are carried out in F' for simplicity, as Mie theory only applies to spheres, which appear distorted in F. This principle is applied in Chapter 4. Next the electromagnetic field behaviour under Lorentz boosts was illustrated with examples: the flattening of point charge field lines and the energy density change of a plane wave due to motion relative to an external observer. Finally, the Lorentz boost of helical fields is shown, along with the invariance of their helicity under Lorentz boosts, a crucial aspect in subsequent chapters.

In Chapter 4, the backscattered signal by a relativistically moving, dielectric and lossless sphere moving along the z-axis was investigated. The scattering setup comprised an arbitrarily oriented Gaussian beam finite in space, allowing for a finite interaction between the beam and the sphere. After discussing the nature of the incident field, the necessary

reference frames were outlined. Due to the arbitrary orientation of the beam, an additional reference frame $F^{\parallel}$ was defined. In frame $F^{\parallel}$, the propagation of the beam is always parallel to its local $z^{\parallel}$ axis (cf. Fig. 4.3). As a result, the abovementioned frame F corresponds to where an external observer views the rotated beam. Moreover, it is in frame F where the backscattered signal is observed.

Following the definition of all reference frames, it was explained how the FHM should be applied. In line with the first step of the FHM, the incident Gaussian beam was subsequently rotated and boosted to frame F'. Importantly, the beam was described as a superposition of helical plane waves since the helicity of an electromagnetic field is invariant under Lorentz boosts. Considering helicity invariance decreases the mathematical complexity of the necessary calculations. After obtaining the incident field in frame F', the scattered field and backscattered energy density were obtained in frame F' using Mie theory. Afterwards, the backscattered energy density was inverse Lorentz boosted to frame F, completing the final step of the FHM. From the backscattered energy density in F, the directivity was defined. The directivity is the ratio of the backscattered energy density to the average scattered energy by the sphere per unit solid angle. The directivity was then visualised as a function of Mie angles. Mie angles are an abstract representation of Mie coefficients, which describe all possible configurations a sphere could have.

Subsequently, the directivity was explored for fixed Mie angles and varying sphere speeds and incident field angle. It was found that Doppler shifts cause the directivity to become increasingly large when the incident field propagates antiparallel to the motion of the sphere for increasing speeds. The opposite occurs when the sphere's motion and beam propagation are in the same direction. The directivity was also minimised, leading to a relativistic Kerker condition. Specifically, a combination of Mie angles was found that yield a directivity of 1.09×10^{-8}. In other words, the backscattered energy density comprises only $1.09 \times 10^{-6}\%$ of the average scattered energy per unit solid angle.

Chapter 5 offered an extension to Chapter 4, where arrays of spheres were considered instead of a single sphere. The figure of merit to minimise was the acceleration time τ, which measures how long it takes to accelerate the array to a target speed of 20% of the speed of light. The acceleration time depends on the intensity of the incident light, the area of the light sail, the sail's speed, the mass of each constituent sphere, the payload mass, the reflectance and absorptance of the sail. The spherical arrays serve as models for light sails that could be used to explore neighbouring solar systems. The first type of array consisted of homogeneous Si, SiO_2 and Al spheres. Moreover, the acceleration time was numerically minimised for each material without making any assumptions about their reflectance or absorptance. It was argued why one should, in fact, firstly ensure a high reflectance and low absorptance. A high reflectance corresponds to a high momentum transfer to the sail, while a low absorptance reduces thermal damage. After considering homogeneous spheres, core-shell spheres were investigated. It was found that a sail made from spheres with an Si core and SiO_2 shell produced the most favourable acceleration time of $\tau = 395.3$ s. Afterwards, the effects of lattice interactions were leveraged to explain why an Si/SiO_2 light sail yields a high broadband reflectance. Next, the effects of an embedding surrounding the spheres was investigated. It was shown that the embedding can have a refractive index n_{emb} up to $n_{\mathrm{emb}} = 1.13$ without having to re-optimise the Si/SiO_2 array. Finally, a new optimisation was carried out with a polydimethyl- siloxane (PDMS) embedding with a refractive index $n_{\mathrm{PDMS}} = 1.45$, showing the wide applicability of the methods in this chapter.

In Chapter 6, arguably the most complex system in this thesis was considered - relativistic scattering by non-symmetric, chiral biomolecules. Specifically, the effects of relativistic motion on the molecules' transmission circular dichroism (TCD) was investigated. The considered molecules were B-DNA, chlorophyll *a* and chlorophyll *b*. Since molecules are typically found in clusters, the method of rotational averaging was implemented to obtain the rotationally averaged TCD (RATCD). The RATCD was obtained by rotating the molecules 50 times, determining the TCD for each angle of orientation, summing all TCD signals and dividing by the number of rotation angles. Using the FHM, the RATCD was observed in frame F. Interestingly, it was found that the RATCD simply contracts to shorter wavelengths in frame F as the speeds of the molecules increase. This contraction is due to the Doppler shift of the incident field.

Outlook

Owing to the futuristic nature of the work in this thesis, opportunities for further research are plentiful. Beginning with Chapter 4, a frequency-dependent T-matrix could be used instead of one that is dispersionless. Although the dispersionless T-matrix provided good approximations for lower speeds, the inclusion of dispersion would lead to a more comprehensive treatment for faster spheres. The work in Chapter 5 could be extended to include temperature dependence of the sail's absorptance. As mentioned, Si has a very temperature-dependent absorptance. To account for this, an acceleration time that incorporates temperature could be implemented. Of course, a model for the temperature changes would have to incorporate both heating by the incident laser and cooling due to the frigidity of outer space. A further extension to Chapter 5 would be the implementation of inverse design. Specifically, one could use inverse design to create core-shell spheres that have predefined, desired parameters for the corresponding light sail. Furthermore, the stability of the core-shell light sails could be investigated by implementing techniques from previous work done on other light sail models [56, 150, 151]. It is important to develop models that are as comprehensive as possible to ensure success of the BSI. Finally, the findings in Chapter 6 also provide promising avenues for future research. An example would be the consideration of arbitrary directions of motion of the molecules. This more general approach would involve using angle-dependent expressions for plane wave expansion coefficients given in Refs [119, 149].

Bibliography

[1] P. Barlis, C. Di Mario, H. van Beusekom, N. Gonzalo, and E. Regar, "Novelties in cardiac imaging—optical coherence tomography (OCT)", EuroIntervention **4**, C22–6 (2008).

[2] T. Kubo and T. Akasaka, "Optical coherence tomography imaging: current status and future perspectives: current and future developments in OCT", Cardiovascular Intervention and Therapeutics **25**, 2–10 (2010).

[3] J. Li, X. Li, D. Mohar, A. Raney, J. Jing, J. Zhang, A. Johnston, S. Liang, T. Ma, K. K. Shung, S. Mahon, M. Brenner, J. Narula, Q. Zhou, P. M. Patel, and Z. Chen, "Integrated IVUS–OCT for real-time imaging of coronary atherosclerosis", JACC: Cardiovascular Imaging **7**, 101–103 (2014).

[4] T. Wang, T. Pfeiffer, E. Regar, W. Wieser, H. van Beusekom, C. T. Lancee, G. Springeling, I. Krabbendam-Peters, A. F. van der Steen, R. Huber, and G. van Soest, "Heartbeat OCT and motion-free 3d in vivo coronary artery microscopy", JACC: Cardiovascular Imaging **9**, 622–623 (2016).

[5] J. G. Fujimoto, J. M. Schmitt, E. A. Swanson, and I.-K. Jang, "The development of OCT", Cardiovascular OCT Imaging, 1–21 (2015).

[6] D. Park, J. Hwang, K. Jang, D. Han, K. Ahn, and B. Baik, "Use of laser Doppler flowmetry for estimation of the depth of burns", Plastic and Reconstructive Surgery **101**, 1516–1523 (1998).

[7] M. Khatib, S. Jabir, E. Fitzgerald O'Connor, and B. Philp, "A systematic review of the evolution of laser Doppler techniques in burn depth assessment", Plastic Surgery International **2014**, 621792 (2014).

[8] B. Alsbjörn, J. Micheels, and B. Sørensen, "Laser Doppler flowmetry measurements of superficial dermal, deep dermal and subdermal burns", Scandinavian Journal of Plastic and Reconstructive Surgery **18**, 75–79 (1984).

[9] G. Hosoda, G. Holloway, and D. Heimbach, "Laser Doppler flowmetry for the early detection of hypertrophic burn scars", The Journal of Burn Care & Rehabilitation **7**, 496–497 (1986).

[10] L. T. Perelman, "Optical diagnostic technology based on light scattering spectroscopy for early cancer detection", Expert Review of Medical Devices **3**, 787–803 (2006).

[11] J. R. Mourant, I. J. Bigio, J. Boyer, R. L. Conn, T. Johnson, and T. Shimada, "Spectroscopic diagnosis of bladder cancer with elastic light scattering", Lasers in Surgery and Medicine **17**, 350–357 (1995).

[12] Y.-F. Huang, Y.-W. Lin, Z.-H. Lin, and H.-T. Chang, "Aptamer-modified gold nanoparticles for targeting breast cancer cells through light scattering", Journal of Nanoparticle Research **11**, 775–783 (2009).

[13] D. K. Pleskow, M. S. Sawhney, P. K. Upputuri, T. M. Berzin, M. F. Coughlan, U. Khan, M. Glyavina, X. Zhang, L. Chen, C. J. Sheil, J. M. Cohen, E. Vitkin, Y. N. Zakharov, I. Itzkan, L. Zhang, L. Qiu, and L. T. Perelman, "In vivo detection of bile duct precancer with endoscopic light scattering spectroscopy", Nature Communications **14**, 109 (2023).

[14] G. Mie, "Beiträge zur optik trüber medien, speziell kolloidaler metallösungen", Ann. Phys. **330**, 377–445 (1908).

[15] P. C. Waterman, "Matrix formulation of electromagnetic scattering", Proceedings of the IEEE **53**, 805–812 (1965).

[16] C. F. Bohren, "Light scattering by an optically active sphere", Chemical Physics Letters **29**, 458–462 (1974).

[17] M. I. Mishchenko, L. D. Travis, and A. A. Lacis, "Scattering, absorption, and emission of light by small particles", Cambridge University Press (2002).

[18] D. Sinclair, "Light scattering by spherical particles", Journal of the Optical Society of America **37**, 475–480 (1947).

[19] R. Graaff, J. Aarnoudse, J. R. Zijp, P. Sloot, F. De Mul, J. Greve, and M. Koelink, "Reduced light-scattering properties for mixtures of spherical particles: a simple approximation derived from Mie calculations", Applied Optics **31**, 1370–1376 (1992).

[20] D. Tzarouchis and A. Sihvola, "Light scattering by a dielectric sphere: perspectives on the Mie resonances", Applied Sciences **8**, 184 (2018).

[21] W. Mundy, J. Roux, and A. Smith, "Mie scattering by spheres in an absorbing medium", Journal of the Optical Society of America **64**, 1593–1597 (1974).

[22] C. Sorensen and D. Fischbach, "Patterns in Mie scattering", Optics Communications **173**, 145–153 (2000).

[23] T. Wriedt, "Mie theory: a review", The Mie Theory, 53–71 (2012).

[24] R. Drake and J. Gordon, "Mie scattering", American Journal of Physics **53**, 955–962 (1985).

[25] Y.-L. Geng, X.-B. Wu, L.-W. Li, and B.-R. Guan, "Mie scattering by a uniaxial anisotropic sphere", Physical Review E **70**, 056609 (2004).

[26] Y. Pavlyukh and W. Hübner, "Nonlinear Mie scattering from spherical particles", Physical Review B **70**, 245434 (2004).

[27] R. Hightower and C. Richardson, "Resonant Mie scattering from a layered sphere", Applied Optics **27**, 4850–4855 (1988).

[28] D. Kunz, A. Thurn, and W. Burchard, "Dynamic light scattering from spherical particles", Colloid and Polymer Science **261**, 635–644 (1983).

[29] A. V. Kildishev, A. Boltasseva, and V. M. Shalaev, "Planar photonics with metasurfaces", Science **339**, 1232009 (2013).

[30] T. J. Garner, A. Lakhtakia, J. K. Breakall, and C. F. Bohren, "Lorentz invariance of absorption and extinction cross sections of a uniformly moving object", Physical Review A **96**, 053839 (2017).

[31] T. J. Garner, A. Lakhtakia, J. K. Breakall, and C. F. Bohren, "Time-domain electromagnetic scattering by a sphere in uniform translational motion", Journal of the Optical Society of America A **34**, 270–279 (2017).

[32] T. J. Garner, A. Lakhtakia, J. K. Breakall, and C. F. Bohren, "Scattering characteristics of relativistically moving concentrically layered spheres", Physics Letters A **382**, 362–366 (2018).

[33] C. C. Handapangoda, M. Premaratne, and P. N. Pathirana, "Plane wave scattering by a spherical dielectric particle in motion: a relativistic extension of the mie theory", Progress In Electromagnetics Research **112**, 349–379 (2011).

[34] B. Zerulla, M. Krstić, D. Beutel, C. Holzer, C. Wöll, C. Rockstuhl, and I. Fernandez-Corbaton, "A multi-scale approach for modeling the optical response of molecular materials inside cavities", Advanced Materials **34**, 2200350 (2022).

[35] B. Zerulla, R. Venkitakrishnan, D. Beutel, M. Krstić, C. Holzer, C. Rockstuhl, and I. Fernandez-Corbaton, "A T-matrix based approach to homogenize artificial materials", Advanced Optical Materials **11**, 2201564 (2023).

[36] B. Zerulla, D. Beutel, C. Holzer, I. Fernandez-Corbaton, C. Rockstuhl, and M. Krstić, "A multi-scale approach to simulate the nonlinear optical response of molecular nanomaterials", Advanced Materials **36**, 2311405 (2024).

[37] B. Zerulla, C. Li, D. Beutel, S. Oßwald, C. Holzer, J. Bürck, S. Bräse, C. Wöll, I. Fernandez-Corbaton, L. Heinke, C. Rockstuhl, and M. Krstić, "Exploring functional photonic devices made from a chiral metal-organic framework material by a multi-scale computational method", Advanced Functional Materials **34**, 2301093 (2024).

[38] B. Zerulla, M. Krstić, S. Chen, Z. Yu, D. Beutel, C. Holzer, M. Nyman, A. Nefedov, Y. Wang, T. G. Mayerhöfer, C. Wöll, and C. Rockstuhl, "Polarization-dependent effects in vibrational absorption spectra of 2D finite-size adsorbate islands on dielectric substrates", Physical Chemistry Chemical Physics **26**, 13683–13693 (2024).

[39] P. Garg, A. G. Lamprianidis, D. Beutel, T. Karamanos, B. Verfürth, and C. Rockstuhl, "Modeling four-dimensional metamaterials: a T-matrix approach to describe time-varying metasurfaces", Optics Express **30**, 45832–45847 (2022).

[40] A. G. Lamprianidis, C. Rockstuhl, and I. Fernandez-Corbaton, "Transcending the rayleigh hypothesis with multipolar sources distributed across the topological skeleton of a scatterer", Journal of Quantitative Spectroscopy and Radiative Transfer **296**, 108455 (2023).

[41] X. Wang, P. Garg, M. Mirmoosa, A. Lamprianidis, C. Rockstuhl, and V. Asadchy, "Expanding momentum bandgaps in photonic time crystals through resonances", Nature Photonics, 1–7 (2024).

[42] H.-T. Chen, A. J. Taylor, and N. Yu, "A review of metasurfaces: physics and applications", Reports on Progress in Physics **79**, 076401 (2016).

[43] S. M. Choudhury, D. Wang, K. Chaudhuri, C. DeVault, A. V. Kildishev, A. Boltasseva, and V. M. Shalaev, "Material platforms for optical metasurfaces", Nanophotonics **7**, 959–987 (2018).

[44] K. Koshelev, S. Lepeshov, M. Liu, A. Bogdanov, and Y. Kivshar, "Asymmetric metasurfaces with high-q resonances governed by bound states in the continuum", Physical review letters **121**, 193903 (2018).

[45] P. Daukantas, "Breakthrough Starshot", Optics and Photonics News **28**, 26–33 (2017).

[46] K. L. Parkin, "The Breakthrough Starshot system model", Acta Astronautica **152**, 370–384 (2018).

[47] https://breakthroughinitiatives.org/initiative/3, (Accessed 08.12.2024).

[48] R. V. Petrescu, R. Aversa, A. Apicella, S. Kozaitis, T. Abu-Lebdeh, and F. I. Petrescu, "NASA started a propeller set on board Voyager 1 after 37 years of break", American Journal of Engineering and Applied Sciences **11**, 66–77 (2018).

[49] M. Beech, "A journey through time and space: Alpha Centauri", Astronomy & Geophysics **53**, 6–10 (2012).

[50] J. Brewer, M. F. Campbell, P. Kumar, S. Kulkarni, D. Jariwala, I. Bargatin, and A. P. Raman, "Multiscale photonic emissivity engineering for relativistic lightsail thermal regulation", Nano Letters **22**, 594–601 (2022).

[51] W. Jin, W. Li, C. Khandekar, M. Orenstein, and S. Fan, "Laser cooling assisted thermal management of lightsails", ACS Photonics **9**, 3384–3390 (2022).

[52] G. R. Holdman, G. R. Jaffe, D. Feng, M. S. Jang, M. A. Kats, and V. W. Brar, "Thermal runaway of silicon-based laser sails", Advanced Optical Materials **10**, 2102835 (2022).

[53] M. Rafat, H. R. Dullin, B. T. Kuhlmey, A. Tuniz, H. Luo, D. Roy, S. Skinner, T. J. Alexander, M. S. Wheatland, and C. M. de Sterke, "Self-stabilization of light sails by damped internal degrees of freedom", Physical Review Applied **17**, 024016 (2022).

[54] D.-C. Savu and A. J. Higgins, "Structural stability of a lightsail for laser-driven interstellar flight", Acta Astronautica **201**, 376–393 (2022).

[55] N. Gieseler, A. Rahimzadegan, and C. Rockstuhl, "Self-stabilizing curved metasurfaces as a sail for light-propelled spacecrafts", Optics Express **29**, 21562–21575 (2021).

[56] Z. Manchester and A. Loeb, "Stability of a light sail riding on a laser beam", The Astrophysical Journal Letters **837**, L20 (2017).

[57] T. Fend, G. Jorgensen, and H. Küster, "Applicability of highly reflective aluminium coil for solar concentrators", Solar Energy **68**, 361–370 (2000).

[58] H. Bennett, M. Silver, and E. Ashley, "Infrared reflectance of aluminum evaporated in ultra-high vacuum", JOSA **53**, 1089–1095 (1963).

[59] Y. Jiang, H. Liu, J. Bai, Z. Li, X. Yang, D. Chen, J. He, L. Wang, and D. Liu, "Infrared optical properties of sio2 films on silicon substrate under different temperatures", Optical Engineering **61**, 031204–031204 (2022).

[60] H. A. Atwater, A. R. Davoyan, O. Ilic, D. Jariwala, M. C. Sherrott, C. M. Went, W. S. Whitney, and J. Wong, "Materials challenges for the Starshot lightsail", Nature Materials **17**, 861–867 (2018).

[61] M. M. Salary and H. Mosallaei, "Photonic metasurfaces as relativistic light sails for Doppler-broadened stable beam-riding and radiative cooling", Laser & Photonics Reviews **14**, 1900311 (2020).

[62] G. Santi, G. Favaro, A. J. Corso, P. Lubin, M. Bazzan, R. Ragazzoni, D. Garoli, and M. G. Pelizzo, "Multilayers for directed energy accelerated lightsails", Communications Materials **3**, 16 (2022).

[63] W. Jin, W. Li, M. Orenstein, and S. Fan, "Inverse design of lightweight broadband reflector for relativistic lightsail propulsion", ACS Photonics **7**, 2350–2355 (2020).

[64] J. Chang, W. Ji, X. Yao, A. J. van Run, and S. Gröblacher, "Broadband, high-reflectivity dielectric mirrors at wafer scale: combining photonic crystal and metasurface architectures for advanced lightsails", Nano Letters **24**, 6689–6695 (2024).

[65] A. Convertino, A. Valentini, T. Ligonzo, and R. Cingolani, "Organic–inorganic dielectric multilayer systems as high reflectivity distributed Bragg reflectors", Applied Physics Letters **71**, 732–734 (1997).

[66] J. Dai, W. Gao, B. Liu, X. Cao, T. Tao, Z. Xie, H. Zhao, D. Chen, H. Ping, and R. Zhang, "Design and fabrication of UV band-pass filters based on SiO2/Si3N4 dielectric distributed Bragg reflectors", Applied Surface Science **364**, 886–891 (2016).

[67] M. F. Schubert, J.-Q. Xi, J. K. Kim, and E. F. Schubert, "Distributed Bragg reflector consisting of high-and low-refractive-index thin film layers made of the same material", Applied Physics Letters **90** (2007).

[68] H. Kim, M. Kaya, and S. Hajimirza, "Broadband solar distributed Bragg reflector design using numerical optimization", Solar Energy **221**, 384–392 (2021).

[69] E. Palo and K. S. Daskalakis, "Prospects in broadening the application of planar solution-based distributed Bragg reflectors", Advanced Materials Interfaces **10**, 2202206 (2023).

[70] C. Zhang, R. ElAfandy, and J. Han, "Distributed Bragg reflectors for gan-based vertical-cavity surface-emitting lasers", Applied Sciences **9**, 1593 (2019).

[71] B. A. McGuire, P. B. Carroll, R. A. Loomis, I. A. Finneran, P. R. Jewell, A. J. Remijan, and G. A. Blake, "Discovery of the interstellar chiral molecule propylene oxide (CH3CHCH2O)", Science **352**, 1449–1452 (2016).

[72] S. Pizzarello and C. T. Yarnes, "Chiral molecules in space and their possible passage to planetary bodies recorded by meteorites", Earth and Planetary Science Letters **496**, 198–205 (2018).

[73] J. E. Hein and D. G. Blackmond, "On the origin of single chirality of amino acids and sugars in biogenesis", Accounts of Chemical Research **45**, 2045–2054 (2012).

[74] A. J. Wagner, D. Y. Zubarev, A. Aspuru-Guzik, and D. G. Blackmond, "Chiral sugars drive enantioenrichment in prebiotic amino acid synthesis", ACS Central Science **3**, 322–328 (2017).

[75] D. Winogradoff, P.-Y. Li, H. Joshi, L. Quednau, C. Maffeo, and A. Aksimentiev, "Chiral systems made from DNA", Advanced Science **8**, 2003113 (2021).

[76] M. H. Jamróz, J. E. Rode, S. Ostrowski, P. F. Lipiński, and J. C. Dobrowolski, "Chirality measures of α-amino acids", Journal of Chemical Information and Modeling **52**, 1462–1479 (2012).

[77] Y.-P. Xue, C.-H. Cao, and Y.-G. Zheng, "Enzymatic asymmetric synthesis of chiral amino acids", Chemical Society Reviews **47**, 1516–1561 (2018).

[78] H. Brückner, D. Becker, and M. Lüpke, "Chirality of amino acids of microorganisms used in food biotechnology", Chirality **5**, 385–392 (1993).

[79] J. Qin, S. Jiang, Z. Wang, X. Cheng, B. Li, Y. Shi, D. P. Tsai, A. Q. Liu, W. Huang, and W. Zhu, "Metasurface micro/nano-optical sensors: principles and applications", ACS nano **16**, 11598–11618 (2022).

[80] Y. Wu, H. W. Huang, and G. A. Olah, "Method of oriented circular dichroism", Biophysical Journal **57**, 797–806 (1990).

[81] N. Berova, K. Nakanishi, and R. W. Woody, "Circular dichroism: principles and applications", John Wiley & Sons (2000).

[82] S. R. Martin and M. J. Schilstra, "Circular dichroism and its application to the study of biomolecules", Methods in Cell Biology **84**, 263–293 (2008).

[83] E. Nabedryk, P. Biaudet, S. Darr, C. J. Arntzen, and J. Breton, "Conformation and orientation of chlorophyll-proteins in Photosystem I by circular dichroism and polarized infrared spectroscopies", Biochimica et Biophysica Acta (BBA)-Bioenergetics **767**, 640–647 (1984).

[84] B. Ranjbar and P. Gill, "Circular dichroism techniques: biomolecular and nanostructural analyses-a review", Chemical Biology & Drug Design **74**, 101–120 (2009).

[85] V. Yannopapas, "Circular dichroism in planar nonchiral plasmonic metamaterials", Optics Letters **34**, 632–634 (2009).

[86] E. A. Gurvitz and A. S. Shalin, "2017 days on diffraction (dd)", IEEE, 159–166 (2017).

[87] Y. Yang, M. Kim, J. Mun, and J. Rho, "Ultra-sharp circular dichroism induced by twisted layered c4 oligomers", Advanced Theory and Simulations **3**, 1900229 (2020).

[88] R. W. Woody, "Circular dichroism", Methods in Enzymology **246**, 34–71 (1995).

[89] W. C. Johnson Jr, "Protein secondary structure and circular dichroism: a practical guide", Proteins: Structure, Function, and Bioinformatics **7**, 205–214 (1990).

[90] M. Vorlíčková, I. Kejnovská, K. Bednářová, D. Renčiuk, and J. Kypr, "Circular dichroism spectroscopy of dna: from duplexes to quadruplexes", Chirality **24**, 691–698 (2012).

[91] R. del Villar-Guerra, J. O. Trent, and J. B. Chaires, "G-quadruplex secondary structure obtained from circular dichroism spectroscopy", Angewandte Chemie **130**, 7289–7293 (2018).

[92] D. Beutel, I. Fernandez-Corbaton, and C. Rockstuhl, "Treams – a T-matrix-based scattering code for nanophotonics", Computer Physics Communications **297**, 109076 (2024).

[93] H. Barhom, A. A. Machnev, R. E. Noskov, A. Goncharenko, E. A. Gurvitz, A. S. Timin, V. A. Shkoldin, S. V. Koniakhin, O. Y. Koval, M. V. Zyuzin, A. S. Shalin, I. I. Shishkin, and P. Ginzburg, "Biological Kerker effect boosts light collection efficiency in plants", Nano Letters **19**, 7062–7071 (2019).

[94] J. D. Jackson, "Classical electrodynamics", John Wiley & Sons (2021).

[95] D. J. Griffiths, "Introduction to electrodynamics", Cambridge University Press (1999).

[96] H. Feshbach and P. M. Morse, "Methods of theoretical physics", McGraw-Hill (1953).

[97] A. Lakhtakia, "Beltrami fields in chiral media", World Scientific **2** (1994).

[98] A. Enciso and D. Peralta-Salas, "Beltrami fields with a nonconstant proportionality factor are rare", Archive for Rational Mechanics and Analysis **220**, 243–260 (2016).

[99] I. Fernandez-Corbaton, D. Beutel, C. Rockstuhl, A. Pausch, and W. Klopper, "Computation of electromagnetic properties of molecular ensembles", ChemPhysChem **21**, 878–887 (2020).

[100] C. F. Bohren and D. R. Huffman, "Absorption and scattering of light by small particles", John Wiley & Sons (2008).

[101] A. Rahimzadegan, C. Rockstuhl, and I. Fernandez-Corbaton, "Core-shell particles as building blocks for systems with high duality symmetry", Physical Review Applied **9**, 054051 (2018).

[102] D. Beutel, A. Groner, C. Rockstuhl, and I. Fernandez-Corbaton, "Efficient simulation of bi-periodic, layered structures based on the T-matrix method", Journal of the Optical Society of America B **38**, 1782–1791 (2021).

[103] N. Stefanou, V. Yannopapas, and A. Modinos, "Heterostructures of photonic crystals: frequency bands and transmission coefficients", Computer Physics Communications **113**, 49–77 (1998).

[104] A. Rodger and B. Nordén, "Circular dichroism and linear dichroism", Oxford University Press, USA **1** (1997).

[105] C. Bustamante, I. Tinoco Jr, and M. F. Maestre, "Circular differential scattering can be an important part of the circular dichroism of macromolecules.", Proceedings of the National Academy of Sciences **80**, 3568–3572 (1983).

[106] E. H. Strickland and S. Beychok, "Aromatic contributions to circular dichroism spectra of protein", CRC Critical Reviews in Biochemistry **2**, 113–175 (1974).

[107] B. A. Bondesen and M. D. Schuh, "Circular dichroism of globular proteins", Journal of Chemical Education **78**, 1244 (2001).

[108] N. J. Greenfield, "Using circular dichroism spectra to estimate protein secondary structure", Nature Protocols **1**, 2876–2890 (2006).

[109] TURBOMOLE GmbH, "TURBOMOLE V7.8 a development of University of Karlsruhe and Forschungszentrum Karlsruhe GmbH, 1989-2007, `https://www.turbomole.org`", (2023).

[110] M. Fruhnert, I. Fernandez-Corbaton, V. Yannopapas, and C. Rockstuhl, "Computing the T-matrix of a scattering object with multiple plane wave illuminations", Beilstein Journal of Nanotechnology **8**, 614–626 (2017).

[111] A. Einstein, "Zur Elektrodynamik bewegter Körper", Annalen der Physik **17**, 891–921 (1905).

[112] K. S. Thorne, C. W. Misner, and J. A. Wheeler, "Gravitation", Freeman San Francisco (2000).

[113] I. Fernandez-Corbaton, "Helicity and duality symmetry in light matter interactions: theory and applications", in Frontiers in Optics 2015 (Optica Publishing Group, 2015), LM1H.2.

[114] I. Fernandez-Corbaton, "Total helicity of electromagnetic fields and matter", Physical Review B **103**, 054406 (2021).

[115] D. Poljak and M. Cvetkovic, "Human interaction with electromagnetic fields: computational models in dosimetry", Academic Press (2019).

[116] R. Alaee, R. Filter, D. Lehr, F. Lederer, and C. Rockstuhl, "A generalized Kerker condition for highly directive nanoantennas", Optics Letters **40**, 2645–2648 (2015).

[117] L. Novotny and B. Hecht, "Principles of nano-optics", Cambridge University Press (2012).

[118] M. C. Teich and B. Saleh, "Fundamentals of photonics", Wiley New Jersey **2** (2007).

[119] M. Vavilin and I. Fernandez-Corbaton, "The polychromatic T-matrix", Journal of Quantitative Spectroscopy and Radiative Transfer **314**, 108853 (2024).

[120] A. G. Lamprianidis and A. E. Miroshnichenko, "Excitation of nonradiating magnetic anapole states with azimuthally polarized vector beams", Beilstein Journal of Nanotechnology **9**, 1478–1490 (2018).

[121] I. Fernandez-Corbaton, M. Fruhnert, and C. Rockstuhl, "Dual and chiral objects for optical activity in general scattering directions", ACS Photonics **2**, 376–384 (2015).

[122] A. Rahimzadegan, R. Alaee, C. Rockstuhl, and R. W. Boyd, "Minimalist Mie coefficient model", Optics Express **28**, 16511–16525 (2020).

[123] M. Born and E. Wolf, "Principles of optics: electromagnetic theory of propagation, interference and diffraction of light", Elsevier (2013).

[124] I. Dunning, J. Huchette, and M. Lubin, "JuMP: a modeling language for mathematical optimization", SIAM Review **59**, 295–320 (2017).

[125] N. Rajalakshmi and S. Srivarshini, "Fuel effective photonic propulsion", in IOP conference series: Materials Science and Engineering, Vol. 234, 1 (IOP Publishing, 2017), p. 012005.

[126] W. M. Haynes, "Crc handbook of chemistry and physics", CRC Press (2014).

[127] C. Schinke, P. Christian Peest, J. Schmidt, R. Brendel, K. Bothe, M. R. Vogt, I. Kröger, S. Winter, A. Schirmacher, S. Lim, H. T. Nguyen, and D. MacDonald, "Uncertainty analysis for the coefficient of band-to-band absorption of crystalline silicon", AIP Advances **5** (2015).

[128] L. V. Rodríguez-de Marcos, J. I. Larruquert, J. A. Méndez, and J. A. Aznárez, "Self-consistent optical constants of SiO2 and Ta2O5 films", Optical Materials Express **6**, 3622–3637 (2016).

[129] K. M. McPeak, S. V. Jayanti, S. J. Kress, S. Meyer, S. Iotti, A. Rossinelli, and D. J. Norris, "Plasmonic films can easily be better: rules and recipes", ACS Photonics **2**, 326–333 (2015).

[130] A. B. Evlyukhin, M. Matiushechkina, V. A. Zenin, M. Heurs, and B. N. Chichkov, "Lightweight metasurface mirror of silicon nanospheres", Optical Materials Express **10**, 2706–2716 (2020).

[131] O. Ilic, C. M. Went, and H. A. Atwater, "Nanophotonic heterostructures for efficient propulsion and radiative cooling of relativistic light sails", Nano Letters **18**, 5583–5589 (2018).

[132] C. R. McInnes, "Solar sailing: technology, dynamics and mission applications", Springer Science & Business Media (2004).

[133] A. Macchi, S. Veghini, and F. Pegoraro, ""light sail" acceleration reexamined", Physical Review letters **103**, 085003 (2009).

[134] Z. A. Kudyshev, A. V. Kildishev, V. M. Shalaev, and A. Boltasseva, "Optimizing startshot lightsail design: a generative network-based approach", ACS Photonics **9**, 190–196 (2021).

[135] A. Rahimzadegan, T. D. Karamanos, R. Alaee, A. G. Lamprianidis, D. Beutel, R. W. Boyd, and C. Rockstuhl, "A comprehensive multipolar theory for periodic metasurfaces", Advanced Optical Materials **10**, 2102059 (2022).

[136] M. R. Lien, D. Meng, Z. Liu, M. A. Sakib, Y. Tang, W. Wu, and M. L. Povinelli, "Experimental characterization of a silicon nitride photonic crystal light sail", Optical Materials Express **12**, 3032–3042 (2022).

[137] V. Valković and J. Obhođaš, "Origins of chiral life in interstellar molecular clouds", The Astronomical Journal **163**, 270 (2022).

[138] G. Marloie, M. Lattelais, F. Pauzat, J. Pilmé, and Y. Ellinger, "Looking for homochirality in the inter-stellar medium", Interdisciplinary Sciences: Computational Life Sciences **2**, 48–56 (2010).

[139] I. Myrgorodska, C. Meinert, Z. Martins, L. Le Sergeant d'Hendecourt, and U. J. Meierhenrich, "Molecular chirality in meteorites and interstellar ices, and the chirality experiment on board the esa cometary rosetta mission", Angewandte Chemie International Edition **54**, 1402–1412 (2015).

[140] A. C. Evans, C. Meinert, C. Giri, F. Goesmann, and U. J. Meierhenrich, "Chirality, photochemistry and the detection of amino acids in interstellar ice analogues and comets", Chemical Society Reviews **41**, 5447–5458 (2012).

[141] C. Giri, F. Goesmann, C. Meinert, A. C. Evans, and U. J. Meierhenrich, "Synthesis and chirality of amino acids under interstellar conditions", Biochirality: Origins, Evolution and Molecular Recognition, 41–82 (2013).

[142] C. D. Stevenson and J. P. Davis, "Magnetars and magnetic separation of chiral radicals in interstellar space: homochirality", The Journal of Physical Chemistry A **123**, 9587–9593 (2019).

[143] C. Meinert, P. De Marcellus, L. Le Sergeant d□Hendecourt, L. Nahon, N. C. Jones, S. V. Hoffmann, J. H. Bredehöft, and U. J. Meierhenrich, "Photochirogenesis: photochemical models on the absolute asymmetric formation of amino acids in interstellar space", Physics of Life Reviews **8**, 307–330 (2011).

[144] S. Thripati, R. Gautam, and R. O. Ramabhadran, "Possible role of metal-ions in the chemistry of prochirality and the origin of chirality in the interstellar medium", ACS Earth and Space Chemistry **7**, 77–91 (2023).

[145] A. D. Garcia, C. Meinert, H. Sugahara, N. C. Jones, S. V. Hoffmann, and U. J. Meierhenrich, "The astrophysical formation of asymmetric molecules and the emergence of a chiral bias", Life **9**, 29 (2019).

[146] A. Bergantini, M. J. Abplanalp, P. Pokhilko, A. I. Krylov, C. N. Shingledecker, E. Herbst, and R. I. Kaiser, "A combined experimental and theoretical study on the formation of interstellar propylene oxide (ch3chch2o)—a chiral molecule", The Astrophysical Journal **860**, 108 (2018).

[147] A. Semechko, "Https://uk.mathworks.com/matlabcentral/fileexchange/37004-suite-of-functions-to-perform-uniform-sampling-of-a-sphere", (2024).

[148] W.-K. Tung, "Group theory in physics", World Scientific **1** (1985).

[149] M. Vavilin, J. D. Mazo-Vásquez, and I. Fernandez-Corbaton, "Computing the interaction of light pulses with objects moving at relativistic speeds", arXiv preprint arXiv:2404.05117 (2024).

[150] E. Popova, M. Efendiev, and I. Gabitov, "On the stability of a space vehicle riding on an intense laser beam", Mathematical Methods in the Applied Sciences **40**, 1346–1354 (2017).

[151] A. Shirin, E. Schamiloglu, C. Sultan, Y. Yang, J. Benford, and R. Fierro, "Modeling and stability of a laser beam-driven sail", in 2021 American Control Conference (ACC) (IEEE, 2021), pp. 4269–4275.